Charles University in Prague

Faculty of Mathematics and Physics

DOCTORAL THESIS

Nina Benešová

Thermal Convection in Terrestrial Planetary Mantles

Department of Geophysics

Supervisor of the doctoral thesis: Doc. RNDr. Hana Čížková PhD.
Study programme: Physics
Specialization: Geophysics

Prague 2015

First of all, I would like to thank Hana Čížková, the supervisor of the thesis, for her leadership and endless patience. I would like to thank my consultant Ondřej Čadek, for his guidance especially in the beginning of this work. Further, I would like to thank Nicola Tosi, Arie van den Berg and Marie Běhounková for providing their results for benchmarks, Michal Kuráž for providing additional computational capacities and to all members of the Department of Geophysics for creating friendly atmosphere. Last but not least, I am very grateful to my family, especially my parents, who supported me through my seemingly never ending studies, Michal and Mirka for proofreading this thesis, and Vojta for supporting me anytime, anywhere.

This research has been supported by the Grant Agency of Charles University grant No. GAUK 2333/2007, by the research project MSM0021620860 of the Czech Ministry of Education, Youth and Sports, and by grant SVV-2010-261308.

I declare that I carried out this doctoral thesis independently, and only with the cited sources, literature and other professional sources.

I understand that my work relates to the rights and obligations under the Act No. 121/2000 Coll., the Copyright Act, as amended, in particular the fact that the Charles University in Prague has the right to conclude a license agreement on the use of this work as a school work pursuant to Section 60 paragraph 1 of the Copyright Act.

In Prague .... Nina Benešová

Název práce: Termální konvekce v pláštích terestrických těles

Autor: Nina Benešová

Katedra: Katedra geofyziky

Vedoucí disertační práce: Doc. RNDr. Hana Čížková, PhD., Katedra geofyziky

Abstrakt: V této práci prezentujeme výsledky numerických modelů termálního vývoje Země a terestrických planet. Zaměřili jsme se zejména na dva problémy: I) studium vnitřní struktury Venuše a Merkuru s využitím měřených dat — geoidu a povrchové topografie, a II) vliv post-perovskitu na chladnutí Země. V části I jsme provedli simulace tečení v plášti Venuše v modelech s různým reologickým popisem. Modelová spektra geoidu a topografie jsme porovnali se spektry měřených dat. Nejlepší shodu s daty dostáváme pro model s radiálním profilem viskozity charakterizovaným 200 km silnou litosférou, bez astenosféry a s nárustem viskozity ve spodním plášti. Naopak, žádný z našich modelů Merkuru nevystihoval pozorovaná data. To naznačuje, že geoid a topografie na Merukuru mají jiný než dynamický původ. V části II jsme se zabývali otázkou, jak přítomnost nízkoviskozního post-perovskitu ovlivní konvekci a chladnutí Země. Ukázali jsme, že přítomnost post-perovskitu výrazně zvýší efektivitu chladnutí jádra. Oproti tomu zahrnutí hloubkově závislých materiálových parametrů (teplotní roztažnost a vodivost) chladnutí zpomaluje.

Klíčová slova: numerické simulace, plášťová konvekce, termální vývoj, geoid a topografie, post-perovskit

Title: Thermal Convection in Terrestrial Planetary Mantles

Author: Nina Benešová

Department: Department of Geophysics

Supervisor: Doc. RNDr. Hana Čížková, PhD., Department of Geophysics

Abstract: In this thesis, we present results of a numerical modelling study focused on the thermal evolution of the Earth and terrestrial planets. We focus particularly on two problems: I) constraining the internal structure of Venus and Mercury using their geoid and surface topography data and II) evaluating the effects of a rheologically distinct post-perovskite on the secular cooling of the Earth. In part I, we performed simulations in a broad group of models of the Venusian mantle, characterised by different rheological descriptions, and we compared spectra of their geoid and their surface topography with the observed quantities. Our analysis suggested that the geoid and the surface topography of Venus are consistent with a radially symmetric viscosity model with a strong 200 km thick lithosphere, without an asthenosphere and with a gradual viscosity increase in the underlying mantle. In the case of Mercury, none of our models was able to predict observed data, thus suggesting other than a dynamic origin of observed geoid and topography. In part II, we investigated style of Earth's mantle convection and its long-term evolution in the models that take into account a weak post-perovskite. We conclude that the presence of the weak post-perovskite enhances the core cooling. This effect is comparable in magnitude to the effect of a depth-dependent material parameters that, on the other hand, tends to delay the secular cooling.

Keywords: numerical simulations, mantle convection, thermal evolution, geoid and topography, post-perovskite

Contents

Introduction

The terrestrial bodies have a similar composition and structure as our Earth. They are assumed to have formed through the same processes of accretion and differentiation. They have a solid surface, they are composed mainly of silicate rocks and metals and they have the same structure of a metallic (mostly iron) core inside a silicate mantle. Those bodies can be planets (including exoplanets) or smaller bodies like satellites of the planets (e.g. the Moon). In the Solar System, there are four terrestrial planets: Mercury, Venus, Earth and Mars.

Although those terrestrial planets are similar in some basic characteristics, they differ in many ways. Among other things, Earth is the only planet where the surface plate motion is currently observed. It has been widely accepted that the primary mechanism that can explain its internal dynamics is mantle convection as, on the geological time scale, the mantle material flows as a viscous fluid. The energy driving the convection originates from primordial heat and from a decay of radioactive elements. This energy is manifested on the surface by the plate tectonics. Other planets do not reveal their internal dynamics in such a way and we have only indirect information about their internal processes (like remains of a volcanic activity on their surface). Therefore, it is difficult to determine whether these planets experience thermal convection at present. It is assumed that these planets must transfer heat from the core to the surface in a similar fashion as the Earth, and that they experienced mantle convection at least in the past, although its regime might have been different.

Various approaches can be used for constraining the structure and the internal dynamics of the Earth and other planets. An inversion of the seismic data (travel times, waveforms, free-oscillations) provides rather detailed information about the structure of the Earth interior. However, it provides only a snapshot of the present state, moreover, it is not available for other planets.

That is why numerical simulations of mantle convection are traditionally used to investigate thermal evolution and dynamical processes in the mantle. Character of the convection is determined by the parameters of the mantle material (viscosity, thermal expansivity, thermal diffusivity, etc.). With increasing pressure and temperature, the material undergoes mineralogical changes and its properties can change considerably. The deformation of mantle rocks under the conditions of the Earth's deep interior can be studied by laboratory experiments and ab initio calculations. Both approaches give crucial constraints on mantle material properties. However, they have large uncertainties and give only a range of possible values. Mantle convection models can be then used to put additional constraints on those parameters. We can use numerical models to explore the parameter space by running multiple calculations with varying input parameters. Then we can compare the output with the observed quantities (e.g. heat flow, character of thermal anomalies, gravity, topography, etc.) and thus we can identify the admissible models satisfying the observations.

High demands on computational capacities is a restraining factor in using numerical models. Since the field of computer technology is developing rapidly it becomes more and more feasible to perform calculations in a realistic 3D spherical geometry. Nevertheless, it is still computationally challenging to carry out the simulations with realistic material characteristics and complex mantle processes. This explains the common use of simplifying geometries like cylindrical, spherical axisymmetric or Cartesian. Within the scope of this work, a convection code was developed, which allows to carry out the calculations both in axisymmetric spherical shell and in fully 3D spherical geometry with some additional simplifying assumptions to reduce the computational costs. The code was applied to problems related to Venus, Mercury and Earth mantle evolution.

From all the terrestrial planets, Venus most closely resembles the Earth and it is sometimes called Earth's sister planet. It has similar size, mass, surface composition and distance to the Sun. On the other hand, it is markedly different in other aspects. It has a dense atmosphere consisting mainly of carbon dioxide that through the greenhouse effect makes Venus the hottest planet in the Solar System (~ 735 K at the surface). This thick atmosphere also prevented any visual observations of Venus' surface until the development of radar observations. The surface is shaped by a volcanic activity and no evidences for the plate tectonics were found. In the absence of global tectonics, Venus is often assumed to have a stiff lithosphere that reduces the heat loss from the interior, causing the interior to be relatively hot. This concept could be consistent with the fact that Venus lacks internal magnetic field and it may imply that Venus' heat budget and convective regime are markedly different than the Earth's ones.

Of the Solar System planets, Mercury is the smallest and the closest to the Sun. It is probably the least understood one of the inner planets. Its proximity to the Sun makes it difficult target for both ground-based observations and spacecraft missions. Our knowledge of the planet is based mainly on the measurements made by two spacecraft. Mariner 10 in 1970s provided first close-up images of its surface which revealed its old heavily cratered surface. Recently, our knowledge about the planet was dramatically improved by measurements of MESSENGER mission. Among others, it provided images of the surface in much higher resolution, it was equipped with magnetometer that confirmed the existence of internal magnetic field and its spectrometers provided an estimate of the surface element abundances. Important piece of knowledge is the fact that Mercury has a relatively large core and a thin mantle (in comparison with the other terrestrial planets). This implies that its formation or its evolution may be significantly different from the other planets. Important question arises, whether a viable mantle convection can still occur in such a thin mantle (400 km at maximum).

In the lack of seismic data, an important source of information about internal structure of a planet is its gravity and its topography. The gravitational field of a planet can be constructed through an analysis of the tracking data of an orbiter. The surface topography can be measured from the orbit using a radar altimeter. That data is available for both Venus and Mercury, although their limited resolution and accuracy should be kept in mind. In the case of Venus, gravity and topography data are available with a relatively high resolution based mainly on Pioneer Venus (late 1970s) and Magellan (1990s) measurements. In recent years, these data have been already analysed to reveal some information about the Venusian mantle structure mostly in the terms of steady-state models. Here, we perform a broad parametric study: we vary the viscosity model and the characteristic density distribution (as controlled by Rayleigh number) and we perform time-dependent calculations of thermal convection. Then, we analyse the spectra of the geoid and the topography generated by these models and we compare them to the observed quantities with the aim to constrain the mantle viscosity stratification. In the case of Mercury, MESSENGER measurements of gravity and topography are very recent and only few analyses were published so far. We focus here on the main question whether the data is consistent with mantle convection still operating in Mercurian mantle and whether the dynamic support is a possible mechanism that may explain topographic and geoid data.

The last question addressed in this thesis concerns the long-term evolution/ cooling of the Earth mantle. After its formation, ~ 4.5 Ga ago, the Earth was much hotter then nowadays. Since then, it is losing heat primarily by the process of mantle convection. Although the radioactive decay acts as a contrary process (it heats the planet), in total, Earth losses heat and thus cools in time. This process of secular cooling is generally very complex and it depends on the initial state of the Earth on the onset of mantle convection and on the Earth material parameters. The question of Earth cooling has already been addressed in numerous studies and effects of various mantle parameters were investigated. A decade ago a new high-pressure phase of perovskite (post-perovskite) was discovered in the lowermost mantle. It was suggested it has different properties than perovskite (e.g. lower viscosity). Such a distinct layer just above the core-mantle boundary (in mantle convection thermal boundary layer) should exert a significant influence on the cooling process. We study this effect in mantle convection models in combination with the effects of other material parameters.

The structure of the thesis is as follows. Chapter 1 gives an overview of the mathematical description of mantle convection, solution methods and benchmark tests. The results are then divided into two parts. Part I (Chapters 2 and 3) deals with Venus and Mercury and it uses their gravity and topography to constrain their structure and dynamics. Part II (Chapters 4 and 5) focuses on the effects of post-perovskite on the long-term evolution of the Earth and on the possible constraints on its spatial distribution. Appendix introduces the formalism of spherical harmonic functions employed to solve the problem.

1. Theory and Method

1.1 Formulation of the problem

Thermal convection in the mantle is described by the set of equations based on general laws of conservation. Various simplifying approximations and assumptions are usually applied when solving the equations. The extended Boussinesq approximation is used here, which is widely used when simulating mantle convection (e.g. Ita and King, 1994; Matyska and Yuen, 2007; King et al., 2010).

The basic equations in the extended Boussinesq approximation are as follows:

$$\begin{aligned} \nabla \cdot \boldsymbol{v} &= 0, && (1.1) \\ \nabla \cdot \tau &= -\Delta\varrho\, \boldsymbol{g}, && (1.2) \\ \varrho_0 c_p \frac{\partial T}{\partial t} &= \nabla \cdot (k \nabla T) - \varrho_0 c_p \boldsymbol{v} \cdot \nabla T - \varrho_0 v_r \alpha T g + \sigma : \nabla \boldsymbol{v} + H + L_t. && (1.3) \end{aligned}$$

Eq. (1.1) is the equation of continuity under the assumption that the material is incompressible. Eq. (1.2) is the momentum equation assuming the infinite Prandtl number (neglecting inertial forces) and omitting the self-gravitation. Right-hand side (RHS) of this equation is a source term—buoyancy force caused by density heterogeneities. Finally, (1.3) is the energy equation. Terms on the RHS of the energy equation represent heat conduction, heat advection, adiabatic cooling or heating, viscous dissipation, radioactive heat sources and latent heat associated with phase transitions, respectively. The law of angular momentum conservation further yields that stress tensor τ is a symmetric tensor. For a summary of used symbols see Table 1.1.

Further, we need to specify the rheological description of the material in terms of constitutive equation:

$$\tau = -pI + \sigma. \tag{1.4}$$

Under the assumption of Newtonian fluid, the deviatoric part σ of the stress tensor is considered in the form:

$$\sigma = \eta\big(\nabla \boldsymbol{v} + (\nabla \boldsymbol{v})^T\big). \tag{1.5}$$

Here viscosity η can generally be a function of radius (pressure), temperature and mineral phase parametrised by phase function Γ_k (see eq. (1.12) below)—$\eta = \eta(r, T, \Gamma_k)$. Detailed description of viscosity as a function of p, T and Γ_k differ for various applications and will be further specified in subsequent chapters. We assume linearised equation of state with density anomalies depending linearly on temperature variations through thermal expansivity. Equation of state also includes density changes due to phase transitions:

$$\Delta\varrho = -\varrho_0\alpha(T - T_{ref}) + \sum_k \Delta\varrho_k\Gamma_k. \tag{1.6}$$

Reference density ϱ_0, gravity acceleration g and specific heat c_p are assumed constant. Expansivity α and thermal conductivity k may generally depend on radius.

1.1.1 Boundary and initial conditions

The set of equations (1.1)-(1.6) has to be supplemented by the boundary conditions. The equations are solved on the domain restricted by two spherical surfaces, the planet's surface and the core-mantle boundary (CMB). On both boundaries impermeable free-slip conditions are prescribed—zero radial velocity:

$$\boldsymbol{v} \cdot \boldsymbol{e}_r = 0 \tag{1.7}$$

and zero tangential stress:

$$\tau \cdot \boldsymbol{e}_r - ((\tau \cdot \boldsymbol{e}_r) \cdot \boldsymbol{e}_r)\boldsymbol{e}_r = 0. \tag{1.8}$$

Further, we prescribe temperatures on both boundaries. Temperatures T_{top} at the surface and T_{cmb} at the core-mantle boundary are constant along the boundary, but T_{cmb} may vary with time in some applications.

The initial condition differs for various problems and will be specified for each model separately.

1.1.2 Phase transitions

The effect of major mantle phase transitions in convection codes is usually included either by using effective thermal expansivity (Christensen and Yuen, 1985) or by using phase function Γ_k (van Hunen, 2001). We use both approaches in this thesis. In 3D models we apply effective thermal expansivity, while in 2D models, where we need phase dependent rheology, we use phase function approach.

Table 1.1: Used symbols

$\boldsymbol{v}$	velocity
$\boldsymbol{r}$	position vector
r	radius
z	depth
v_r	radial component of velocity
τ	stress tensor
σ	deviatoric part of the stress tensor
$\boldsymbol{g}$	vector of the gravity acceleration
g	gravity acceleration
t	time
c_p	specific heat at constant pressure
T	temperature
k	thermal conductivity
κ	thermal diffusivity ($\kappa = k/\varrho_0 c_p$), κ_0 denotes reference value
α	coefficient of thermal expansivity, α_0 denotes reference value
H	volume heat sources
L_t	latent heat due to phase changes
p	dynamic pressure
I	identity tensor
η	dynamic viscosity, η_0 denotes reference value
ϱ	density
ϱ_0	reference density at reference temperature T_{ref}
$\Delta\varrho$	density anomalies
Γ_k	phase function of the k-th phase transition
$\Delta\varrho_k$	density change due to the k-th phase transition
d_{ph}^k	transition width of the k-th phase transition
γ_k	Clapeyron slope for k-th phase transition
z_0^k	reference transition depth at a reference temperature T_0^k
z_{ph}^k	depth of the k-th phase transition
$\Delta\eta_k$	viscosity jump due to the k-th phase transition
$\boldsymbol{e}_r$	unit radial vector
T_{top}	temperature at the surface (r_{top})
T_{cmb}	temperature at the core-mantle boundary (r_{cmb})
d	thickness of the mantle
Ra	Rayleigh number
Ra_q	Rayleigh number for heat sources
Ra_k	phase Rayleigh number
Nu	Nusselt number
Di	dissipation number

1.1.2.1 Phase function approach (2D models)

Phase transitions are parametrised by harmonic phase functions. Phase function of k-th transition is assumed in following form:

$$\Gamma_k = \frac{1}{2}\left[1 + \sin\left(\pi \frac{z - z_{ph}^k(T)}{d_{ph}^k}\right)\right]. \tag{1.9}$$

Function Γ_k ranging between 0 and 1 indicates what portion of material underwent the transition. In eq. (1.9) d_{ph}^k sets width of the transition and the temperature dependence of transition depth z_{ph}^k is described by:

$$z_{ph}^k(T) = z_0^k + \frac{1}{\varrho_0 g}\gamma_k(T - T_0^k), \tag{1.10}$$

where z_0^k is the reference depth of the transition at the reference temperature T_0^k and γ_k is the Clapeyron slope of the transition. The buoyancy effect of the phase change is included in RHS of eq. (1.2) according to eq. (1.6). The latent heat L_t associated with phase changes (RHS of eq. (1.3)) due to all phase changes is as follows (van Hunen, 2001):

$$L_t = \sum_k \frac{\gamma_k \Delta\varrho_k T}{\varrho_0}\frac{\mathrm{D}\Gamma_k}{\mathrm{D}t}. \tag{1.11}$$

In some models we also assume phase dependent viscosity:

$$\eta(r, T, \Gamma_k) = (1 - \Gamma_k)\eta(r, T) + \Delta\eta_k \Gamma_k \eta(r, T), \tag{1.12}$$

where $\Delta\eta_k$ is the viscosity jump due to k-th phase transition.

1.1.2.2 Effective thermal expansivity approach (3D models)

Both buoyancy and latent heat effects of phase transition can alternatively be introduced by assuming effective thermal expansivity α' (Christensen and Yuen, 1985; Matyska and Yuen, 2007). We parametrise the transition by Gaussian function and effective thermal expansivity then yields:

$$\alpha' = \alpha + \frac{\Delta\rho_k \gamma_k}{\rho_0^2 g d_{ph}^k \sqrt{\pi}} \exp\left(-\frac{(z - z_0^k)^2}{(d_{ph}^k)^2}\right). \tag{1.13}$$

Compared to the above mentioned approach using phase function Γ_k, here phase transition occurs at a constant depth z_0^k.

1.1.3 Dimensionless formulation

Governing equations (1.1)-(1.3) can be simplified by introducing new dimensionless variables (denoted by primes):

$$\boldsymbol{r} = d\boldsymbol{r'}, \quad t = \frac{d^2}{\kappa_0}t', \quad \boldsymbol{v} = \frac{\kappa_0}{d}\boldsymbol{v}', \quad p = \frac{\eta_0\kappa_0}{d^2}p', \quad T = T_{top} + (T_{cmb} - T_{top})T'. \tag{1.14}$$

Here κ_0 and η_0 are reference values of thermal diffusivity and viscosity. Basic equations (1.1)-(1.2) together with the rheology equation (1.5) of state (1.6) then yield:

$$\nabla' \cdot \boldsymbol{v}' = 0, \tag{1.15}$$

$$\nabla' p' + \nabla' \cdot \frac{\eta}{\eta_0}\big(\nabla'\boldsymbol{v}' + (\nabla'\boldsymbol{v}')^T\big) = \Big(\frac{\alpha}{\alpha_0}Ra(T' - T'_{ref}) - \sum_k Ra_k\Gamma_k\Big)\frac{\boldsymbol{g}}{g} \tag{1.16}$$

and energy equation yields:

$$\frac{\partial T'}{\partial t'} = \nabla \cdot (k\nabla' T') - \boldsymbol{v}' \cdot \nabla T' - Di\frac{\alpha}{\alpha_0}\Big(T' + \frac{T_{top}}{T_{cmb} - T_{top}}\Big)v'_r + \tag{1.17}$$

$$+ \frac{Di}{Ra}\frac{\eta}{\eta_0}\big(\nabla'\boldsymbol{v}' + (\nabla'\boldsymbol{v}')^T\big) : \nabla'\boldsymbol{v}' + \frac{Ra_q}{Ra} + \tag{1.18}$$

$$+ \sum_k \frac{Ra_k}{Ra}Di\Big(T' + \frac{T_{top}}{T_{cmb} - T_{top}}\Big)\gamma_k\frac{\mathrm{D}\Gamma'_k}{\mathrm{D}t'}, \tag{1.19}$$

where Ra, Di, Ra_q and Ra_k are dimensionless numbers.

The presence and the vigour of convection is controlled by Rayleigh number

$$Ra = \frac{\varrho_0\alpha_0 g(T_{cmb} - T_{top})d^3}{\kappa_0\eta_0}. \tag{1.20}$$

When Ra is below the critical value for the fluid, temperature perturbations are damped and convection does not begin. When Ra exceeds the critical value, the convection is generated by temperature variations. The higher the Rayleigh number is, the more vigorous is the convective flow. In the models with non-constant material parameters, the style and the vigour of flow also reflects spatial variability of parameters and it is necessary to define what reference values of these parameters are to be used in the definition of Rayleigh number. In cases where viscosity, thermal diffusivity and expansivity are depth-dependent, surface values are often used for the Rayleigh number definition. This choice could, however, be misleading especially in case of viscosity, as surface values of viscosity can differ by orders of magnitude from the rest of the mantle. Therefore, we use the volume-averaged viscosity for Ra evaluation, unless stated otherwise.

Adiabatic and viscous heating scale with the dissipation number Di. It is defined as follows:

$$Di = \frac{\alpha_0 g d}{c_p}. \tag{1.21}$$

Internal heat sources are characterised by Rayleigh number for heat sources Ra_q:

$$Ra_q = \frac{\varrho_0 \alpha_0 g H d^5}{\kappa_0 \eta_0 k_0}, \tag{1.22}$$

and Ra_k is the phase Rayleigh number and is defined as follows:

$$Ra_k = \frac{\Delta\varrho_k g d^3}{\kappa_0 \eta_0}. \tag{1.23}$$

The time variability of convective mixing may be characterised by Nusselt number Nu. The Nusselt number represents ratio of the heat flux from the convective solution to purely conductive heat flux solution at the surface (Nu_{top}) or CMB (Nu_{cmb}). Here we use Nu scaled by $\frac{r_{top}}{r_{cmb}}$ ratio:

$$Nu_{top} = \frac{d}{T_{cmb} - T_{top}} \frac{r_{top}}{r_{cmb}} \left.\frac{\partial T}{\partial r}\right|_{r=r_{top}}, \qquad Nu_{cmb} = \frac{d}{T_{cmb} - T_{top}} \frac{r_{cmb}}{r_{top}} \left.\frac{\partial T}{\partial r}\right|_{r=r_{cmb}} \tag{1.24}$$

It reflects the time behaviour of the solution. For an Earth-like convection system with $Ra \sim 10^7$–10^8, the statistically steady-state solution is obtained, characterised by oscillating Nu with time independent mean.

1.2 Strategy of solution

The problem introduced above was solved in spherical geometry. We solved the problem both in 2D axisymmetric and fully 3D geometry. In case of 3D geometry, additional simplifying assumptions were applied, thus the strategy of the solution slightly differs between 2D and 3D cases. First let us discuss common features and then the differences will be discussed in subsequent paragraphs.

Solution of the convection problem starts from the initial temperature distribution $T_{ini}(r, \vartheta, \varphi)$. Density variations $\Delta\varrho_{ini}(r, \vartheta, \varphi)$ corresponding to this initial distribution are calculated using eq. (1.6). Then Stokes' problem (eqs. (1.1), (1.2), (1.4) and (1.5)) with boundary conditions (1.7) and (1.8) is solved. Obtained velocity and stress are then used to evaluate RHS terms of eq. (1.3) and the temperature distribution in the next time step is computed. This procedure is then repeated for this new temperature distribution.

Our solution method is based on spectral decomposition in angular coordinates and finite differences in radial direction (Čížková and Čadek, 1997). All laterally dependent quantities are approximated by finite series of spherical harmonic functions (see Appendix A). By substituting the expansions (A.1a)–(A.1c) into governing equations a set of ordinary differential equations is obtained. The expansions are in principle infinite series, therefore we need to truncate the expansions at some degree (cut-off degree j_{max}) to obtain finite number of equations and unknowns. This cut-off degree determines the resolution in lateral direction. The typical value of j_{max} in this work is 250, which gives lateral resolution of about 80 km at the surface of the Earth. In radial direction the domain is divided into n layers and radial derivatives are evaluated using second-order finite difference method (Fornberg, 1988). Typical number of layers is 100, which gives radial resolution of 30 km.

1.2.0.1 Solution of Stokes' problem

After applying the formalism of spherical harmonic functions, the equations for Stokes' problem take the form of ordinary differential equations (A.16)–(A.23) which becomes a set of algebraic equations after approximating radial derivatives by finite differences (Zhang and Christensen, 1993). This can be written in the matrix form as

$$\boldsymbol{A}\boldsymbol{x} = \boldsymbol{b}, \tag{1.25}$$

where $\boldsymbol{x}$ is a vector of unknowns (harmonic coefficients of stress (τ_{jm}^{j0}, τ_{jm}^{j-2}, τ_{jm}^{j}, τ_{jm}^{j+2}) and velocity (v_{jm}^{j-1}, v_{jm}^{j+1})) and $\boldsymbol{b}$ contains source term—coefficients of buoyancy. If viscosity in eqs. (A.19)–(A.21) varies only with the radius, the equations are linear, they are split according to degree j and order m, and matrix $\boldsymbol{A}$ is a band matrix, formed by square submatrices for each degree. Consequently, the problem can be solved for each submatrix separately, using efficient algorithms for solving the band matrices. Solution of the problem in this case is both time and memory efficient.

For general (laterally dependent) viscosity, the couplings between viscosity and strain-rate tensor arise, matrix $\boldsymbol{A}$ is not split according to degree and order. Although it is sparse, it is not band and the problem must be solved for all degrees together.

1.2.0.2 Thermal equation and time step

To integrate the thermal equation (1.3), Runge-Kutta scheme of second order is applied. The criterion for optimising time step Δt is Courant–Friedrichs–Lewy condition that ensures, that the distance travelled by material within one time-step does not exceed the grid spacing. For advection motion, the time step (Δt_{adv}) restriction is given by

$$\Delta t_{adv} \leq \left(\frac{\Delta r}{v_r^{max}} \right), \tag{1.26}$$

where v_r^{max} is the maximum radial velocity, and Δr is the corresponding discretisation step. The conduction time step Δt_{cond} is:

$$\Delta t_{cond} \leq \left(\frac{\Delta r_{min}}{2\kappa} \right), \tag{1.27}$$

where Δr_{min} is the minimum discretisation step. The time step is then chosen as the minimum of the advection and the conduction ones:

$$\Delta t = C \min\bigl(\Delta t_{adv}, \Delta t_{cond}\bigr). \tag{1.28}$$

Coefficient C varies in the range (0,0.5] and adjusts the time step with respect to the temperature changes in i-th time step, to ensure that those changes are as follows:

$$0.005 < \frac{\max(|T_{i+1} - T_i|)}{\max(T_i)} < 0.02, \tag{1.29}$$

where T_i and T_{i+1} are temperature distributions in two successive time steps.

1.2.0.3 Evaluation of non-linear terms

The most time-consuming part of the computations is the evaluation of the non-linear terms—$\boldsymbol{v} \cdot \nabla T$, $v_r T$, $\sigma : \nabla \boldsymbol{v}$, $\eta \nabla \boldsymbol{v}$ and $T\, \boldsymbol{v} \cdot \nabla \Gamma$. To evaluate the gradient and the divergence of variables, the analytical formulas (A.7)–(A.9) can be used. On the other hand, evaluating products of scalar, vector, and tensor harmonic functions using analytical formulas (A.11)–(A.15) is computationally demanding. It turns out that it is much faster to evaluate those products on the grid (Martinec, 1989). This process consists of three steps: (1) evaluation of scalar, vector or tensor fields in a latitude-longitude grid , (2) enumeration of the product at each grid point, (3) harmonic analysis to compute the harmonic coefficients of the resulting product. The principle of this process is described in Martinec (1989). All formulas needed to perform steps (1)-(3) are stated in Appendix.

1.2.1 2D solution

Let us begin with the description of the 2D solution of the problem. If only spherical harmonic coefficients of order 0 ($m = 0$, in eqs. (A.1a)–(A.1c)) are considered, the solution is axisymmetric (depends only on r and ϑ). This greatly reduces the number of unknown harmonic coefficients and time costs of the calculation. This spherical axisymmetric case is referenced as 2D in this work.

1.2.1.1 Solution of Stokes' problem

As mentioned above, in the case of radially-dependent viscosity ($\eta = \eta(r)$) the matrix $\boldsymbol{A}$ in eq. (1.25) is a band matrix, formed by submatrices for each degree and order and thus the system can be efficiently solved for each degree and order separately. On the other hand, in the case of general laterally-dependent viscosity ($\eta = \eta(r, \vartheta, \varphi)$), this separation is not possible and the whole system has to be solved together. The number of equations depends on the required resolution. For typical values of $j_{max} = 250$ and $n = 100$, the number of equations is $j_{max}[6(n+1)+2] \approx 10^5$, thus the direct inversion of matrix $\boldsymbol{A}$ can be difficult. Therefore, we use the iterative approach, described in Klika (1995). We apply Jacobi iterative method combined with successive overrelaxation. The idea is to formally transform the problem to a problem with radial viscosity. We decompose the viscosity into spherically symmetric part $\eta_0(r)$ and residue $\eta_R(r, \vartheta, \varphi)$ (spatial viscosity deviation from the mean radial profile), thus $\eta(r, \vartheta, \varphi) = \eta_0(r) + \eta_R(r, \vartheta, \varphi)$. In the matrix formalism we decompose the matrix $\boldsymbol{A}$ into "band-diagonal" component $\boldsymbol{D}$, and residue $\boldsymbol{R}$:

$$(\boldsymbol{D} + \boldsymbol{R})\boldsymbol{x} = \boldsymbol{b}. \tag{1.30}$$

The residue is then shifted to the right-hand side:

$$\boldsymbol{D}\boldsymbol{x} = \boldsymbol{b} - \boldsymbol{R}\boldsymbol{x}. \tag{1.31}$$

On the left-hand side (LHS) we now have the band matrix $\boldsymbol{D}$. All couplings arising from residual term $\eta_R(r, \vartheta, \varphi)$ are shifted to the RHS and iterative method is used. The iterative scheme holds:

$$\boldsymbol{D}\boldsymbol{x}^{i+1} = \boldsymbol{b} - \boldsymbol{R}\boldsymbol{x}^{i}, \tag{1.32}$$

where $i = 0, 1, 2, \ldots$ is the number of iterative step.

Finally, we need to specify the first iterative value $\boldsymbol{x}^0$ which is usually set to 0. The iterative loop continues until the normalised difference between the two successive steps $\boldsymbol{x}^{i+1}$ and $\boldsymbol{x}^i$ is less than a predefined precision Δ:

$$\frac{\|\boldsymbol{x}^{i+1}-\boldsymbol{x}^i\|_{L_2}}{\|\boldsymbol{x}^{i+1}\|_{L_2}} < \Delta, \tag{1.33}$$

Here we can take the advantage of the fact that we solve the system (1.32) repeatedly in each time step. At the beginning of the calculation ($t = 0$), we take $\boldsymbol{x}^0_{t=0} \equiv 0$ but as a starting value for subsequent time steps ($\boldsymbol{x}^0_{t>0}$), the solution vector from the previous time step is taken, which markedly speeds up the convergence. Here Δ is the relative difference between viscosities in last two time steps. This convergence criterion should thus reflect the differences between the solutions of the thermal equation in successive time steps.

The successive overrelaxation method is extrapolation of Jacobi method where we take weighted average between the previous iterate $\bar{\boldsymbol{x}}^{i+1}$ and the computed iterate $\boldsymbol{x}^i$ as a solution vector for next iterative step (Young, 1950):

$$\boldsymbol{x}^{i+1} = \omega\bar{\boldsymbol{x}}^{i+1} + (1-\omega)\boldsymbol{x}^i, \tag{1.34}$$

where ω is the relaxation factor. The choice of $\omega > 1$ speeds up the convergence of slow-converging process while $\omega < 1$ helps establish convergence for diverging process. Here, parameter $\omega \leq 1$ was chosen by trial-and-error for each model calculation to optimize convergence.

1.2.2 3D solution

1.2.2.1 Solution of Stokes' problem

While in the 2D case the number of unknown harmonic coefficients for stress and velocity was $\sim 10^5$, in 3D we have a full set of harmonic coefficients for degree $j = 0, 1, \ldots j_{max}$ and order $m = 0, 1, \cdots j$. For $j_{max} = 250$ and $n = 100$ the number of unknowns is $[6(n+1)+2](j_{max}+2)(j_{max}+1)/2 \approx 2 \cdot 10^7$. To assure the time feasibility of the calculations, only the case with radially stratified viscosity is considered in 3D.

If viscosity is depth-dependent and thus no couplings have to be evaluated, problem is linear and we can apply the formalism of Green's (response) functions. System (1.25) is solved repeatedly, in each time step. Matrix $\boldsymbol{A}$ does not change (as viscosity does not depend on temperature) and response functions can only be evaluated once—at the beginning. Thus, using Green's functions formalism considerably speeds up calculations.

1.2.2.2 Thermal equation

Two simplifications were made in thermal equation, which in 3D is considered in the following form:

$$\varrho_0 c_p \frac{\partial T}{\partial t} = k\nabla^2 T - \varrho_0 c_p \boldsymbol{v} \cdot \nabla T - \varrho_0 v_r \alpha T g + H. \tag{1.35}$$

Thermal conductivity k is assumed a constant now, which simplifies the first term on the right hand side. Further simplification is achieved by omitting viscous dissipation. Dissipation term $\sigma : \nabla \boldsymbol{v}$ is the most time-consuming term in the thermal equation to evaluate. We therefore drop this term to suppress computational costs. We however do consider adiabatic heating (3rd term of RHS of (1.35)). Adiabatic and viscous heating terms should in principle either both be considered (extended Boussinesq approximation) or both omitted (classical Boussinesq approximation). Dropping viscous heating term while keeping adiabatic heating term is not consistent and violates energy conservation. However, it is useful to have adiabatic heating term included (Čížková and Matyska, 2004)—it allows for the development of realistic depth temperature gradient, and inclusion of latent heat associated with phase transitions through effective thermal expansivity (1.13).

1.3 Benchmarks

Several benchmarks were performed to verify the numerical implementation of the method. Two sets of benchmarks are presented here. First set (denoted Benchmarks 1) tests the 3D solution. Benchmarks 1a and 1b reproduce the published results of other convection codes under classical Boussinesq approximation. Benchmark 1c tests implementation of adiabatic heating against convection code Antigona (Běhounková et al., 2010). Second set of benchmarks (denoted Benchmarks 2) tests the 2D solution. In 2D case, viscosity can generally be both radially and laterally dependent. In benchmarks 2 we thus test the solution of Stokes problem with laterally dependent viscosity. Our code is benchmarked against the spectral finite element code of Tosi (2007).

1.3.1 Benchmark 1

1.3.1.1 Benchmark 1a

If we take model case with small but supercritical Ra, the thermal convection in a spherical shell has two stable solutions found by perturbation analysis (Busse, 1975; Busse and Riahi, 1982). Those two stable modes have tetrahedral (dominant spherical harmonic degree $j = 3$ and order $m = 2$), and cubic (dominant harmonic degree $j = 4$ and orders $m = 0, 4$) symmetries. These cases are commonly used as standard benchmark test and the results are published in several studies. To obtain these solutions, we performed simulations of isoviscous convection in a spherical shell under Boussinesq approximation with a constant boundary temperature, and impermeable free-slip boundary conditions with inner to outer radius ratio ($r_{i/o}$) equal to 0.55. To obtain two different solutions, we applied two different initial conditions (Yoshida and Kageyama, 2004). As an initial temperature field, the conductive profile is taken, and a perturbation is added: $T(r,\theta,\varphi) = T_{cond}(r) + T_{pert}(r,\theta,\varphi)$, where $\nabla^2 T_{cond} = 0$. The perturbation term for the tetrahedral symmetry is:

$$T_{pert}(r,\theta,\varphi) = 0.1(T_{cmb} - T_{top}) \sin \frac{\pi(r - r_{cmb})}{d} Y_{32}(\theta,\varphi), \tag{1.36}$$

and for the cubic symmetry is:

$$T_{pert}(r,\theta,\varphi) = 0.1(T_{cmb} - T_{top}) \sin \frac{\pi(r - r_{cmb})}{d} \left[Y_{40}(\theta,\varphi) + \frac{5}{7} Y_{44}(\theta,\varphi) \right], \tag{1.37}$$

where Y_{jm} are spherical harmonic functions (see Appendix A). These tests were performed for Ra in the range from 2000 to 14000. In higher Ra runs, the temperature solution of the corresponding lower Ra run was used as the initial condition.

We benchmarked our results against results of seven different codes: Bercovici et al. (1989), referenced here as Be89, where equations are solved with the spectral method; Zhong et al. (2000, 2008) using finite element code CitcomS, referenced as Zh00 and Zh08; Richards et al. (2001) (referenced Ri01) who employed finite element code TERRA; Yoshida and Kageyama (2004) published benchmark of their finite difference code (ref. YK04), Choblet et al. (2007) used finite volume code ŒDIPUS, referenced as Ch07, Běhounková et al. (2010) uses code named Antigona which contains convection part from ŒDIPUS but uses different advection scheme (super-bee slope limiter), referenced as Be10 and hybrid spectral code Wr10 (Wright et al., 2010). Our code is referenced here

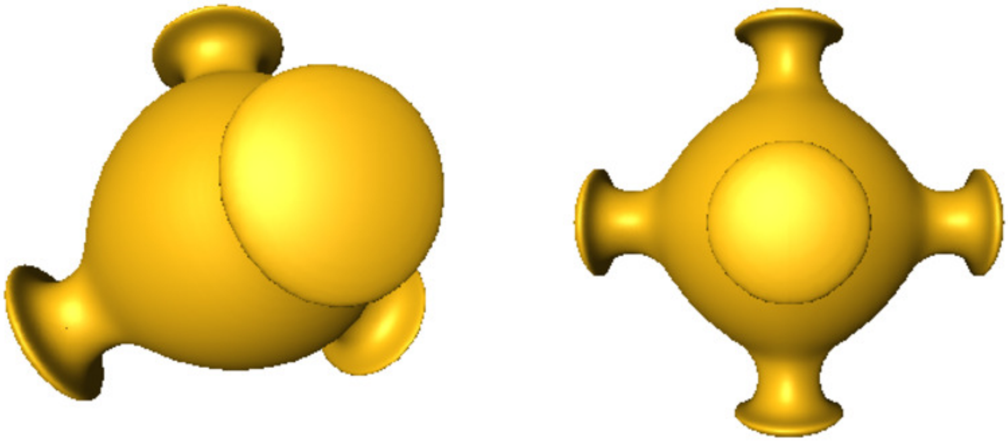

Figure 1.1: Isosurface of temperature 1800 K for tetrahedral and cubic symmetry cases, $Ra = 7000$.

as Be14. Three quantities were compared between benchmark models: surface and bottom Nusselt numbers (1.24) and dimensionless root mean square velocity $v_{rms} = \frac{d}{\kappa}\sqrt{\int_V \boldsymbol{v}\cdot\boldsymbol{v}\,\mathrm{d}V}$ (V being the volume of the mantle).

Temperature isosurfaces of the solutions for both symmetries with Rayleigh number 7000 are shown in Fig. 1.1. Results for all models considered are summarised in Tables 1.2 and 1.3. To show the deviation from the benchmark models, we use the relative error with respect to our model Be14. It can be concluded that errors are within the range of a few per cent at maximum, not more than the comparison models differ among each other.

1.3.1.2 Benchmark 1b

Comparing Nusselt numbers and root mean square velocity is a common way to benchmark convection codes. Although it only compares the mean statistical values, it is an easy way to compare codes that use different methods on entirely different grids. Here we want to go a bit further and compare our code against another spectral code in more detail. Bercovici et al. (1991) present values of harmonic coefficients of temperature variance for both cubic and tetrahedral cases and different Rayleigh numbers. Temperature variance is defined as

$$\langle T^2\rangle_{jm} = \int_{r_{cmb}}^{r_{top}} T_{jm}T^*_{jm}r^2\mathrm{d}r, \tag{1.38}$$

where * denotes complex conjugation. This value is normalised by the dominant value for each symmetry. For the tetrahedral pattern, the dominant mode is $\langle T^2\rangle_{32}$, while for the cubic symmetry it is mode $\langle T^2\rangle_{40}$. Results of our code

Table 1.2: Benchmark 1a results, tetrahedral symmetry. Numbers in parentheses give relative differences between published benchmark models and our model denoted with respect as Be14:

$Ra = 2000$, $r_{i/o} = 0.55$

Ref.	Nu_{top}	Nu_{cmb}	v_{rms}
Be89	2.2507 (2.0%)	2.2532 (2.1%)	-
Zh00	2.218 (0.5%)	2.201 (0.2%)	-
YK04	2.2025 (0.2%)	-	12.1246 (4.0%)
Be10	2.2109 (0.2%)	2.2149 (0.4%)	12.65 (0.2%)
Be14	2.2067	2.2061	12.6176

$Ra = 7000$, $r_{i/o} = 0.55$

Ref.	Nu_{top}	Nu_{cmb}	v_{rms}
Be89	3.4657 (1.3%)	3.5293 (0.7%)	-
Zh08	3.5126 (0.4%)	3.4919 (0.3%)	32.66 (0.0%)
Ri01	3.4160 (2.8%)	-	-
YK04	3.4430 (1.9%)	-	32.0481 (1.9%)
Ch07	3.4814 (0.8%)	3.4717 (0.9%)	32.743 (0.3%)
Wr10	3.4962 (0.4%)	3.4962 (0.2%)	32.6424 (0.0%)
Be10	3.4889 (0.6%)	3.4953 (0.2%)	32.52 (0.4%)
Be14	3.5101	3.5040	32.6472

$Ra = 14000$, $r_{i/o} = 0.55$

Ref.	Nu_{top}	Nu_{cmb}	v_{rms}
Ri01	4.2250 (2.0%)	-	-
YK04	4.2395 (1.7%)	-	50.0048 (1.0%)
Be10	4.2818 (0.7%)	4.2856 (0.2%)	50.13 (0.7%)
Be14	4.3108	4.2962	50.4992

Table 1.3: Benchmark 1a results, cubic symmetry. Same as Table 1.2

$Ra = 3500$, $r_{i/o} = 0.55$

Ref.	Nu_{top}	Nu_{cmb}	v_{rms}
Be89	2.7954 (2.2%)	2.7568 (3.5%)	-
YK04	2.8830 (0.9%)	-	18.4801 (2.9%)
Ch07	2.8640 (0.3%)	2.8948 (1.4%)	19.546 (2.7%)
Be10	2.8254 (1.1%)	2.8237 (1.0%)	18.86 (0.8%)
Be14	2.8561	2.8529	19.0140

$Ra = 7000$, $r_{i/o} = 0.55$

Ref.	Nu_{top}	Nu_{cmb}	v_{rms}
YK04	3.5554 (1.9%)	-	30.5197 (1.9%)
Zh08	3.6254 (0.0%)	3.6016 (0.5%)	31.09 (0.0%)
Wr10	3.6096 (0.4%)	3.6096 (0.2%)	31.0820 (0.0%)
Be10	3.5854 (1.1%)	3.5739 (1.2%)	30.73 (1.2%)
Be14	3.6239	3.6184	31.0854

$Ra = 14000$, $r_{i/o} = 0.55$

Ref.	Nu_{top}	Nu_{cmb}	v_{rms}
YK04	4.4231 (1.7%)	-	48.1082 (0.9%)
Be10	4.4236 (1.6%)	4.4198 (1.4%)	47.85 (1.5%)
Be14	4.4962	4.4820	48.5559

Table 1.4: Benchmark 1b results, tetrahedral symmetry. Normalised temperature variance coefficients $\langle T^2_{jm} \rangle$ for tetrahedral cases.

j	4	4	6	7	7	9	10	10
m	0	4	4	2	6	6	4	8
$Ra = 8000$								
Be91	12.360	8.709	2.547	2.233	1.867	4.092	1.387	1.924
Be14	12.227	8.734	2.408	2.185	1.849	4.155	1.383	1.960
$Ra = 16000$								
Be91	12.560	8.978	3.238	3.522	2.981	8.041	2.539	3.599
Be14	12.539	8.957	3.094	3.448	2.918	8.047	2.507	3.551

Table 1.5: Benchmark 1b results, cubic symmetry. Same as Table 1.4

j	6	8	8	10	10	12	12	12
m	4	0	8	4	8	0	4	12
$Ra = 7000$								
Be91	4.746	4.553	2.990	1.397	1.979	4.670	1.261	3.032
Be14	4.747	4.603	3.023	1.395	1.982	4.645	1.252	3.017
$Ra = 14000$								
Be91	5.053	6.416	4.212	3.009	4.263	10.050	2.720	6.528
Be14	5.056	6.448	4.233	3.006	4.259	10.002	2.707	6.499

compared to Bercovici et al. (1991) are shown in Tables 1.4 and 1.5. Relative errors between the two codes are up to 1% for most degrees and do not exceed 5% for ant degree. The ratio of the two largest cubic pattern modes ($\langle T^2 \rangle_{44} / \langle T^2 \rangle_{40}$) was theoretically predicted to be 5/7 (Busse, 1975), and numerically confirmed (Bercovici et al., 1989). Our results agrees with this ratio with accuracy of tenths per mille (not shown in Table 1.5).

1.3.1.3 Benchmark 1c

In previous two benchmarks, the 3D solution under classical Boussinesq approximation was verified. In the third benchmark we test the solution of thermal eq. (1.35) where adiabatic heating is included. For this purpose a simulation with $Ra = 10000$ was carried out. The inner to outer radius ratio is 0.5, dissipation number is 0.48 and the temperature ratio $T_{top}/(T_{cmb} - T_{top})$ is 0.12. Our results were compared against the results of the code Antigona (Běhounková et al., 2010)

Table 1.6: Benchmark 1c results, cubic symmetry

$Ra = 10000$, $r_{i/o} = 0.5$, $Di = 0.48$, $T_{top}/(T_{cmb} - T_{top} = 0.12)$			
Ref.	Nu_{top}	Nu_{cmb}	v_{rms}
Be10	2.342 (1.3%)	3.321 (1.2%)	29.20 (1.1%)
Be14	2.373	3.361	29.51

and are summarised in Table 1.6. Relative differences between the two codes are 1.1–1.3%.

1.3.2 Benchmark 2

1.3.2.1 Benchmark 2a

Up to now we tested models with radially symmetric viscosity, now we will focus on the 2D models with laterally variable viscosity. In this test case we compare Green's response functions of horizontal velocity divergence, dynamic topography and geoid against spectral finite element code (Tosi (2007)—it will be referred to as To07). We computed Green's functions up to degree 10. For this test, a simple viscosity distribution was chosen: $\eta_{00} = \sqrt{4\pi}, \eta_{10} = 2$, otherwise $\eta_{jm} = 0$. The thickness of the mantle was $d = 2891$ km, the inner to outer radius $r_{i/o} = 0.55$, and the gravity acceleration was 9.8 m s^{-2}. We assumed density load at degree 2 ($j_{load} = 2$). The graphs of response functions are shown in Fig. 1.2. Grey line shows response at degree 2 (note that the scale for this curve is on the right), black lines are for response at higher degrees, that are non-zero due the lateral variations of viscosity. Our results agree with To07 within the line thickness. The results at three different depths ($0.25d$, $0.5d$ and $0.75d$) for both codes are presented in Table 1.7. Values are normalised in the following way: surface/CMB topography is -1 at the surface/CMB, geoid have the maximum value -1, and horizontal flow divergence is normalised by its highest value. Relative errors are mostly under 1% and do not exceed 1.3%.

1.3.2.2 Benchmark 2b

While the previous benchmark tested the Stokes' problem solution for a very simple viscosity distribution, and simple unit density load, benchmark 2b should test the case with more complicated density and viscosity distribution. We again compare the velocity field against Tosi (2007). This benchmark was carried out for a model with cut-off degree 50, 145 layers, and temperature dependent viscosity (two orders of magnitude). Input density and viscosity distribution is in Fig. 1.3.

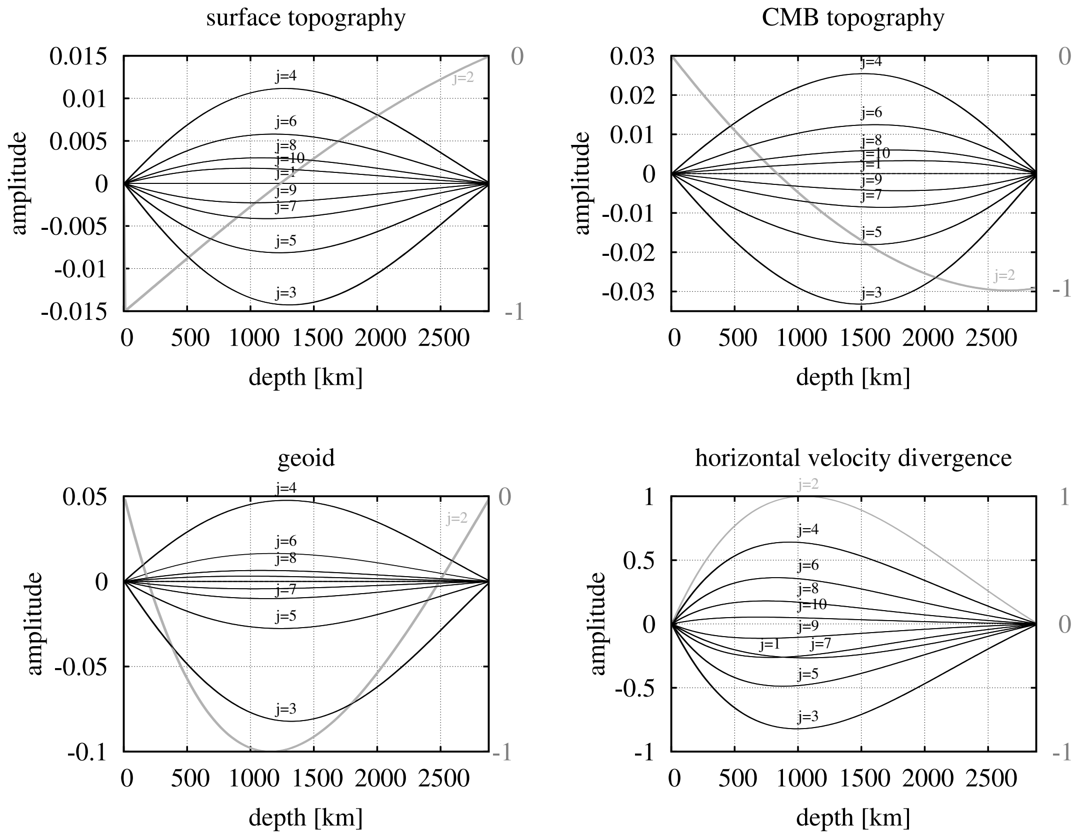

Figure 1.2: Green's functions for $j_{load} = 2$. Grey line is response at degree 2. Scale on the left is for $j > 2$, for $j = 2$ scale on the right applies.

Table 1.7: Becnhmark 2a. Comparison of Green's functions for $j_{load} = 2$ at three depths. Column e contains relative errors between the two codes.

j	surface topography			CMB topography			geoid			horizontal flow div.		
	Be14	To07	e(%)	**Be14**	To07	e(%)	**Be14**	To07	e(%)	**Be14**	To07	e(%)
depth = $0.25d$												
1	0.0000	0.0000	0.0	0.0000	0.0000	0.0	0.0000	0.0000	0.0	-0.2447	-0.2437	0.4
2	-0.7004	-0.7044	0.6	-0.4497	-0.4456	0.9	-0.8841	-0.8800	0.5	0.9261	0.9225	0.4
3	-0.0113	-0.0112	0.5	-0.0233	-0.0232	0.8	-0.0644	-0.0639	0.7	-0.7776	-0.7751	0.3
4	0.0090	0.0090	0.5	0.0175	0.0174	0.8	0.0382	0.0380	0.7	0.6191	0.6175	0.3
5	-0.0067	-0.0067	0.5	-0.0122	-0.0121	0.8	-0.0228	-0.0227	0.6	-0.4777	-0.4768	0.2
6	0.0049	0.0049	0.4	0.0081	0.0080	0.8	0.0140	0.0139	0.6	0.3590	0.3585	0.1
7	-0.0036	-0.0036	0.4	-0.0054	-0.0053	0.8	-0.0088	-0.0088	0.5	-0.2612	-0.2611	0.1
8	0.0027	0.0027	0.3	0.0036	0.0036	0.9	0.0058	0.0058	0.5	0.1804	0.1804	0.0
9	-0.0021	-0.0021	0.2	-0.0025	-0.0025	0.9	-0.0040	-0.0040	0.4	-0.1124	-0.1125	0.1
10	0.0017	0.0017	0.2	0.0018	0.0018	0.9	0.0029	0.0029	0.3	0.0534	0.0534	0.1
depth = $0.5d$												
1	0.0000	0.0000	0.0	0.0000	0.0000	0.0	0.0000	0.0000	0.0	-0.2441	-0.2449	0.3
2	-0.4203	-0.4235	0.8	-0.7771	-0.7742	0.4	-0.9568	-0.9588	0.2	0.9132	0.9161	0.3
3	-0.0141	-0.0141	0.3	-0.0332	-0.0332	0.1	-0.0814	-0.0815	0.1	-0.7278	-0.7304	0.4
4	0.0109	0.0110	0.3	0.0254	0.0254	0.1	0.0469	0.0469	0.1	0.5483	0.5506	0.4
5	-0.0079	-0.0079	0.3	-0.0180	-0.0179	0.1	-0.0269	-0.0270	0.2	-0.4001	-0.4020	0.5
6	0.0055	0.0056	0.4	0.0123	0.0123	0.2	0.0158	0.0158	0.2	0.2847	0.2862	0.5
7	-0.0039	-0.0039	0.4	-0.0084	-0.0084	0.2	-0.0095	-0.0095	0.3	-0.1966	-0.1978	0.6
8	0.0028	0.0028	0.5	0.0058	0.0058	0.2	0.0059	0.0059	0.3	0.1293	0.1301	0.6
9	-0.0020	-0.0020	0.6	-0.0041	-0.0041	0.2	-0.0038	-0.0039	0.4	-0.0769	-0.0774	0.7
10	0.0015	0.0015	0.6	0.0030	0.0030	0.3	0.0026	0.0027	0.5	0.0350	0.0352	0.7
depth = $0.75d$												
1	0.0000	0.0000	0.0	0.0000	0.0000	0.0	0.0000	0.0000	0.0	-0.1318	-0.1331	1.0
2	-0.1825	-0.1848	1.3	-0.9699	-0.9684	0.2	-0.5758	-0.5809	0.9	0.4884	0.4934	1.0
3	-0.0088	-0.0089	1.1	-0.0244	-0.0246	0.7	-0.0517	-0.0521	0.9	-0.3742	-0.3781	1.0
4	0.0066	0.0067	1.1	0.0192	0.0194	0.7	0.0289	0.0291	0.9	0.2704	0.2733	1.1
5	-0.0046	-0.0047	1.1	-0.0141	-0.0142	0.6	-0.0160	-0.0162	0.9	-0.1893	-0.1914	1.1
6	0.0031	0.0032	1.1	0.0101	0.0102	0.6	0.0090	0.0091	1.0	0.1295	0.1310	1.2
7	-0.0021	-0.0021	1.2	-0.0073	-0.0073	0.5	-0.0052	-0.0052	1.0	-0.0862	-0.0872	1.2
8	0.0014	0.0014	1.2	0.0053	0.0053	0.5	0.0031	0.0031	1.1	0.0548	0.0555	1.2
9	-0.0010	-0.0010	1.3	-0.0040	-0.0040	0.4	-0.0019	-0.0019	1.1	-0.0317	-0.0321	1.2
10	0.0007	0.0007	1.3	0.0031	0.0031	0.4	0.0012	0.0013	1.2	0.0140	0.0142	1.3

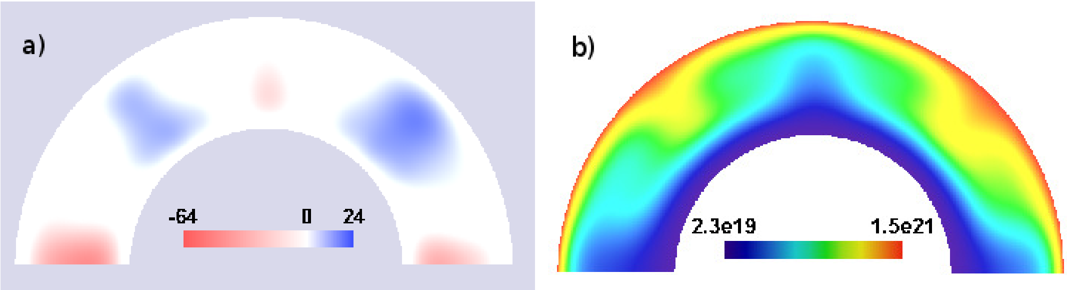

Figure 1.3: Left: input distribution of density anomalies (kg m^{-3}). Right: input distribution of viscosity (Pa s)

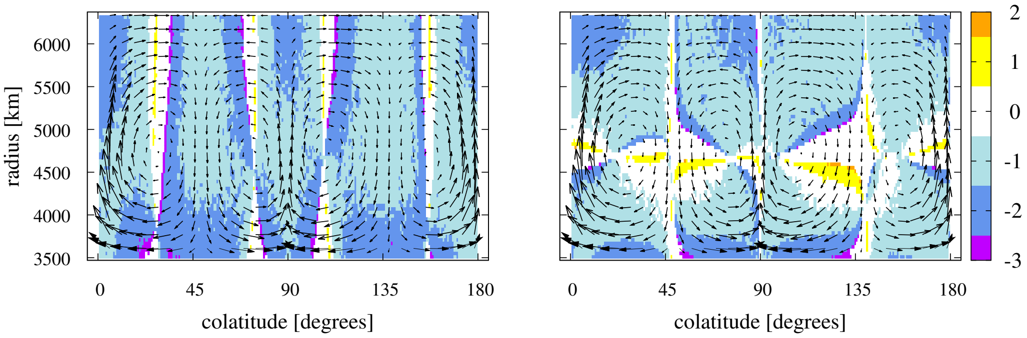

Figure 1.4: Relative differences between models Be14 and To07. Left: radial velocity v_r. Right: horizontal velocity v_ϑ. Arrows display the direction of flow.

Differences in the resulting velocity field are shown in Fig. 1.4. Our velocities differ from To07 by less then 2%.

1.3.3 Time efficiency

Finally, we will describe tests we carried out to evaluate time efficiency of the code. These tests were performed on processor Intel Core Q6600 (2.4 GHz).

1.3.3.1 3D solution

First, the influence of resolution was tested. Dependence on the number of layers (resolution in r-direction) is linear which is transparent, and does not need to be tested. Dependence on the lateral resolution (cut-off degree) was checked for $j_{max} = 16, 32, 64, 128, 256$ and 300. Cut-off degree 300 means lateral resolution 67 km at the surface of Earth. Radial resolution was 45 km (64 layers). Wall-clock time needed to evaluate one integration time-step was measured for this purpose. Ascertained dependence is power-law and time for one time-step ranges from 0.18 s for cut-off degree 16 to 487 s for $j_{max} = 300$, see Fig. 1.5, left panel.

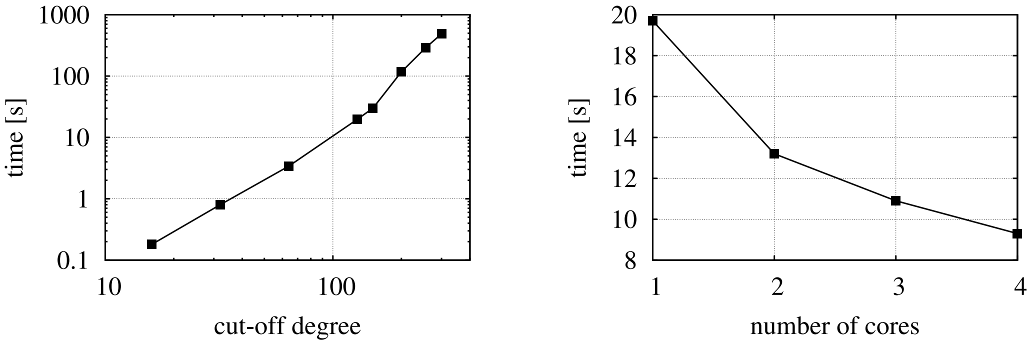

Figure 1.5: Time needed to evaluate 1 integration time step in the 3D model. Left: dependence on cut-off degree (log-log scale), serial calculation. Right: dependence on number of cores, parallel calculation.

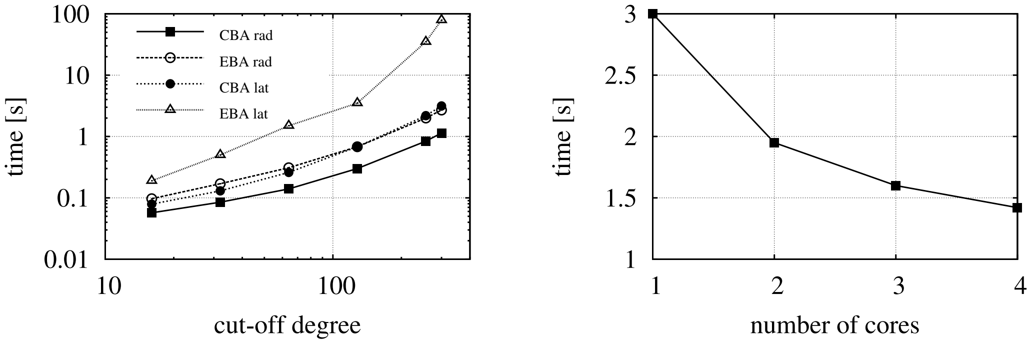

Figure 1.6: Time needed to evaluate 1 integration time step in the 2D model. Left: dependence on cut-off degree (log-log scale), serial calculation, CBA denotes run in classical Boussinesq approximation, EBA means extended Boussinesq approximation and rad/lat indicates type of viscosity dependency (purely radial or both radial and lateral). Right: dependence on number of cores, parallel calculation.

Second test of aims to show the efficiency of parallelisation. The most consuming part of the computation is the evaluation of the non-linear terms in momentum and thermal equations. As the evaluation of these terms proceeds through all layers independently, it can be easily parallelised. OpenMP library enabling parallelisation with shared memory was employed for this purpose. Here we present a test that illustrates the time reduction when the parallelisation is used. Cut-off degree for this test was chosen to be 128 and wall-clock time for one time-step was measured again. Result is demonstrated in the Fig. 1.5, right panel. If calculation on one core takes 100% of time then the same computation takes 67% of time on two cores and 47% on four cores.

1.3.3.2 2D solution

Dependence on the cut-off degree was again inspected in the range from 16 to 300 for 64 layers. Four model runs were tested: classical and extended Boussinesq approximation with either radially, or radially-laterally dependent viscosity. Lateral dependence in this test means temperature dependent viscosity varying by two orders of magnitude. Naturally, the model with the lowest time demands is the model with the radial profile of viscosity in classical Boussinesq approximation. The addition of adiabatic heating and viscous dissipation into the temperature equation requires roughly double computing time. Approximately equally demanding was a model run with temperature-dependent viscosity in classical Boussinesq approximation. The same run but in extended Boussinesq approximation is, of course, the slowest one—one time-step for $j_{max} = 256$ took 35 s. For comparison see Fig. 1.6, left panel.

As in the previous paragraph, above mentioned time efficiency graph (Fig. 1.6, left panel) shows results for calculations without parallelisation. Similarly to 3D case, parallelisation (case $j_{max} = 128$) reduces time costs to 65% on two cores and to 47% on four cores (Fig. 1.6, right panel).

Part I

Geoid, Topography and Mantle Convection in Terrestrial Planets

When we are interested in the interior structure of the Earth, crucial information can be obtained from the analysis of seismic waves propagation—seismic tomography. It is a powerful tool, which provides us with information about the shape of major discontinuities in the interior and structural anomalies that reflect convection pattern in the mantle. However, seismic tomography is only available for the Earth. Therefore, for other terrestrial bodies, here Venus and Mercury, we have to employ other methods to learn something about their internal structure and dynamics. In that respect, gravitational and topographic data provide an important source of information.

Since the gravitational field reflects the mass distribution inside the body, it can be used to study its interior structure. Mantle density anomalies contribute to the gravitational field in two ways. Static spatial distribution of density anomalies affects the gravitational field directly. At the same time, it also induces a flow that distorts the mantle boundaries associated with density contrast (either the surface, core-mantle boundary or any other internal interface). These boundary undulations (dynamic topography) cause additional mass excess or deficit that also affects the observed gravitational field. The character of the mantle flow depends on the mantle parameters where the viscosity plays the key role. If the density distribution is known we can constrain the mantle viscosity structure by solving the geodynamic inverse problem: for the known density distribution and assumed viscosity profile we calculate velocity field and surface deformation by solving Stokes' problem. Geoid generated by known internal density structure and calculated surface topography is then compared with observed data. For the Earth, the distribution of density anomalies can be inferred from seismic tomography and geodynamic inversions were performed by numerous authors to obtain estimates of mantle viscosity structure (e.g. Hager and Clayton, 1989; Ricard et al., 1989; King, 1995; Čadek and Fleitout, 2003).

In the absence of seismic data, a model of the interior density structure for Venus (Mercury) is not available. To supplement this missing information one can assume some simplified or synthetic density distributions while analysing observed gravity and topography data. E.g. Pauer et al. (2006) assumed that the mass anomaly distribution does not vary with depth. Another possible approach to obtain the density distribution is to use numerical simulations of time-dependent mantle convection (e.g. Ratcliff et al., 1995; Solomatov and Moresi, 1996; Kiefer and Kellogg, 1998). Here we use the latter approach. We will try to constrain Venusian and Mercurian viscosity structure by using time-dependent models of their mantle evolution. We will select group of viscosity models that could be applicable to given planet and for each model in this group we generate group of models. Each model is then simulated until it reaches a statistically steady-state. From these simulations we obtain density distribution and dynamic topography, and we compute the gravitational field. Next we compare them to the observed data and thus we constrain viscosity and internal dynamics of the planet.

Geoid and topography

Geoid is defined as an equipotential surface of gravity potential that coincides with mean ocean surface. In the Earth and planetary sciences, the term gravity is usually related to the attraction of a rotating planet, i.e., the gravitational potential includes the potential due to mass distribution and the centrifugal potential due to the rotation of the planet. This potential can be divided into a hydrostatic part (corresponding to the potential of a rotating spherically symmetric body in the hydrostatic equilibrium) and the non-hydrostatic part. The equipotential surface of the hydrostatic potential is called reference ellipsoid and deviations of the geoid from this reference ellipsoid are called the geoid anomaly (or geoid undulations or non-hydrostatic geoid). From now on we will use the term geoid for geoid anomaly, which is a common terminology. Although other names are sometimes used for other bodies (e.g. venoid for Venus), the term geoid will be used here for all planets.

Geoid height $N(\vartheta, \varphi)$ is given by Bruns' theorem (e.g. Heiskanen and Moritz, 1967):

$$N(\vartheta, \varphi) = \frac{V(r_{top}, \vartheta, \varphi)}{g}, \tag{I.1}$$

where V is non-hydrostatic potential evaluated at the mean surface radius and g is the gravitational acceleration which is considered constant here.

To evaluate geoid heights from formula (I.1) we need to evaluate the potential V generated by density anomalies within the body. Let us denote the density anomaly $\varrho(\boldsymbol{r'})$ as the deviation from the reference density located at $\boldsymbol{r}'$. The potential at position $\boldsymbol{r}$ can be computed using Newton's law (Wieczorek, 2007):

$$V(\boldsymbol{r}) = G \int_{V'} \frac{\varrho(\boldsymbol{r'})}{|\boldsymbol{r} - \boldsymbol{r'}|} \mathrm{d}V', \tag{I.2}$$

where the integration is carried out over the whole volume V' of the body under the consideration and G is the gravitational constant. We express density anomalies $\varrho(\boldsymbol{r'})$ as a spherical harmonic series $\varrho(\boldsymbol{r'}) = \sum_{jm} \varrho_{jm}(r') Y_{jm}(\vartheta', \varphi')$ (cf.

A.1a). Further, using addition theorem:

$$\frac{1}{|\boldsymbol{r}-\boldsymbol{r'}|} = \frac{4\pi}{r}\sum_{lk}\frac{1}{2l+1}\left(\frac{r}{r'}\right)^{j+1} Y^*_{lk}(\vartheta',\varphi')Y_{lk}(\vartheta,\varphi) \qquad \text{for } r < r', \tag{I.3}$$

$$\frac{1}{|\boldsymbol{r}-\boldsymbol{r'}|} = \frac{4\pi}{r}\sum_{lk}\frac{1}{2l+1}\left(\frac{r'}{r}\right)^{j} Y^*_{lk}(\vartheta',\varphi')Y_{lk}(\vartheta,\varphi) \qquad \text{for } r \geq r', \tag{I.4}$$

and expressing potential V as a harmonic series $V(\boldsymbol{r}) = \sum_{jm} V_{jm}(r)Y_{jm}(\vartheta,\varphi)$, the coefficients V_{jm} are:

$$V_{jm}(r) = \frac{4\pi Gr}{2j+1}\int\limits_{r'} \varrho_{jm}(r')\left(\frac{r}{r'}\right)^{j-1}\mathrm{d}r' \qquad \text{for } r < r', \tag{I.5}$$

$$V_{jm}(r) = \frac{4\pi Gr}{2j+1}\int\limits_{r'} \varrho_{jm}(r')\left(\frac{r'}{r}\right)^{j+2}\mathrm{d}r' \qquad \text{for } r \geq r'. \tag{I.6}$$

To account for the effect of undulated boundaries with (dynamic) topography $h(\vartheta,\varphi) = \sum_{jm} h_{jm}(r)Y_{jm}(\vartheta,\varphi)$ associated with density contrast $\Delta\varrho_{bnd}$ we introduce additional density anomaly:

$$\varrho^{bnd}_{jm}(r') = \delta(r'-r_{bnd})\Delta\varrho_{bnd}h^{bnd}_{jm}, \tag{I.7}$$

where r_{bnd} is the mean radius of this boundary. The potential at the surface then yields:

$$V_{jm}(r_{top}) = \frac{4\pi Gr_{top}}{2j+1}\left[\int\limits_0^{r_{top}} \varrho_{jm}(r')\left(\frac{r'}{r_{top}}\right)^{j+2}\mathrm{d}r' + \sum_{bnd=1}^{n}\Delta\varrho_{bnd}\, h^{bnd}_{jm}\left(\frac{r_{bnd}}{r_{top}}\right)^{j+2}\right]. \tag{I.8}$$

In all applications presented here we will assume only two boundaries—surface and CMB. To evaluate potential V we need to know the dynamic topographies h^{bnd} of the boundaries. Our model however does not allow for a surface deformation as we prescribe impermeable free-slip conditions on a sphere with a constant radius (eq. 1.7 and 1.8). In such models tangential component of stress is zero as well as radial component of velocity. The vertical component of stress is however not constrained, and this radial component of stress is interpreted as boundary topography. At the surface, the balance of the radial stress component τ^{top}_{rr} and the buoyancy force due to the displaced topography h^{top} (mass excess or deficit) yields:

$$h^{top}(\vartheta,\varphi)g\Delta\varrho_{top} = -(\boldsymbol{e}_r\cdot\tau(r_{top},\vartheta,\varphi)\cdot\boldsymbol{e}_r). \tag{I.9}$$

At the CMB, the effect of pressure in the Earth core must be taken into the account. The balance condition gives:

$$-\varrho_C V_C(r_{cmb}, \vartheta, \varphi) + h^{cmb}(\vartheta, \varphi) g \Delta\varrho_{cmb} = (\boldsymbol{e}_r \cdot \tau(r_{cmb}, \vartheta, \varphi) \cdot \boldsymbol{e}_r), \qquad \text{(I.10)}$$

where V_C are potential perturbations induced in the core by mantle density heterogeneities and by the deformations of all boundaries and ϱ_C is the core density. This potential can be evaluated using eq. (I.5) and (I.6). Similarly, dynamic topography can be evaluated for any boundary associated with a density contrast.

Geoid and topography from convection models

Geoid and topography generated by convection flow are calculated in postprocessing of stress and temperature fields resulting from our convection simulations. Temperature anomalies are converted into density anomalies using state eq. (1.6). Dynamic topographies are evaluated from stress field using (I.9) and (I.10). Geoid is calculated using (I.1) and (I.8) afterwards. Of course our time-dependent simulations can not produce spatial distribution of density, geoid and topography anomalies directly comparable with the observations. Successful model should rather fit the observations in terms of its characteristics—such as power spectra, average number of plumes etc.

2. Venus[1]

2.1 Introduction

Of all the terrestrial planets in the Solar system, Venus most resembles Earth. It has a similar size, density, and surface basalt composition. As a sister planet of Earth, whose dynamic processes should be controlled by the same physical processes, Venus has received a lot of attention of geoscientists as understanding Venus could help to better understand Earth. Information about this planet comes from ground-based observations and space missions either orbiting (Pioneer Venus, Magellan, Venus Express) or landing (Veneras and Vega program) probes. We also have data from flybys of Mariner, Galileo, Cassini-Huygens and MESSENGER. Magellan mission in years 1990–1994 highly improved our knowledge of the planet. Its main task was to map the surface using radar measurements and to measure the gravity field. Magellan radar succeeded in imaging 98% of the surface at resolution of 100 m.

Although there are some similarities between Earth and Venus, there are also differences between the two planets. Contrary to our planet, there is no evidence of plate tectonics on Venus. On Earth, plate tectonics is manifested by the presence of oceanic rift system and ocean trenches that are not observed on Venus (Kaula and Phillips, 1981), thus it is accepted that it is a one-plate planet at present. The absence of global tectonics is the reason why Venus is thought to be in sluggish-lid regime (lithosphere moves markedly slower than the mantle below) or stagnant-lid regime (lithosphere is stiff and immobile), although the small viscosity contrast regime cannot be rejected for certainty, and it was hypothesised that Venus may have been in a plate-tectonic regime at least in the past (O'Neill et al., 2007).

In the absence of plate tectonics the question arises how Venus looses its heat. Since pure conduction through stagnant lithosphere is too inefficient (Reese et al., 1998), it has been hypothesized that the present heat loss of the planet is not in balance with the internal heat generation. Several models of thermal evolution have been proposed based on important observation—Venus' surface has relatively few, randomly distributed, impact craters, indicating that the surface is relatively young—approximately 300–800 million years (Breuer and Moore,

---

[1] The material contained in this chapter was published in BENEŠOVÁ, N. and ČÍŽKOVÁ, H. Geoid and topography of Venus in various thermal convection models. *Stud. Geophys. Geod.* 2012, 56, 2, pp. 621–639.

2007). Possible explanations usually involve different mechanisms of catastrophic resurfacing, either through widespread magmatism (Reese et al., 2007) or episodic events of subduction (Turcotte et al., 1999).

2.1.1 Gravitational and topography data

Both geoid and surface topography satellite data is freely available at `http://pds-geosciences.wustl.edu/missions/magellan/shadr_topo_grav`. We use here geoid by Konopliv et al. (1999) obtained from Magellan Doppler radiometric tracking data together with Pioneer Venus Orbiter gravity data set that is available up to degree and order 180. The surface topography model by Rappaport et al. (1999) is based on Magellan altimetry data and is available up to degree and order 360. The geoid and the topography are displayed in Fig. 2.1 and 2.2.

The surface topography of Venus shows a broad variety of features. Some of them are generally assumed to be connected with the underlying mantle plumes. Coronae are crown shaped volcanic features of typical dimension of several hundred kilometres. They are thought to be related to shallow upwellings due to their relatively small size. Topographic rises are large areas (more than 1000 km diameter and up to 2.5 km height), with an elevated dome-shaped topography, comprising generally several shield volcanoes. Those rises are usually interpreted as the surface expression of the deep mantle plume, possibly originating at the core-mantle boundary. Besides the shape of their long-wave topography, other supporting evidence for their plume origin are large positive gravity anomalies and the connection to large volcanoes. Ten topographic rises were identified (Stofan and Smrekar, 2005). On the basis of their morphology, they can be divided into three types: rift-dominated (Atla and Beta Regiones), volcano-dominated (Bell, Dione, Imdr, Laufey and West Eistla Regiones) and corona-dominated (Themis, East Eistla and Central Eistla Regiones). The different types are hypothesised to be manifestations of variations in the lithospheric structure, or different strength or duration of the underlying plume activity.

Further, Venus Express mission (orbiting planet since 2005) provided data from VIRTIS (Visible and Infrared Thermal Imaging Spectrometer), which measures the spectral emissivity of the surface. Smrekar et al. (2010) compared the data against the topographic map, and inspected the areas off topographic rises. Of the assumed plumes, three were recorded in the VIRTIS measurements (Imdr, Themis and Dione Regiones). All of them show anomalously high emissivity values, which is interpreted as that the lava flows in the regiones being relatively recent (certainly younger than 2.5 million years, and probably younger than

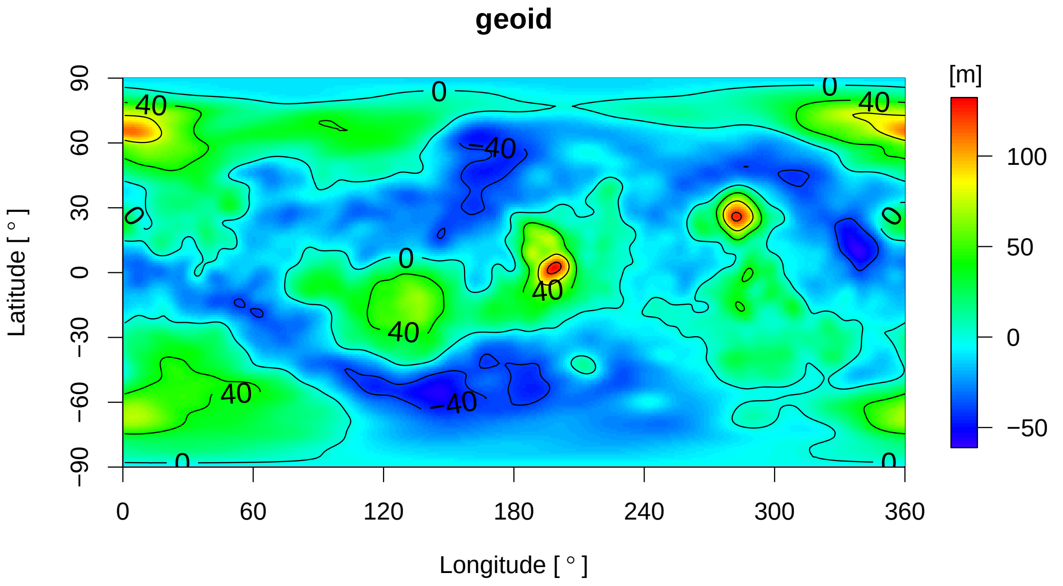

Figure 2.1: Geoid for degrees 3-40.

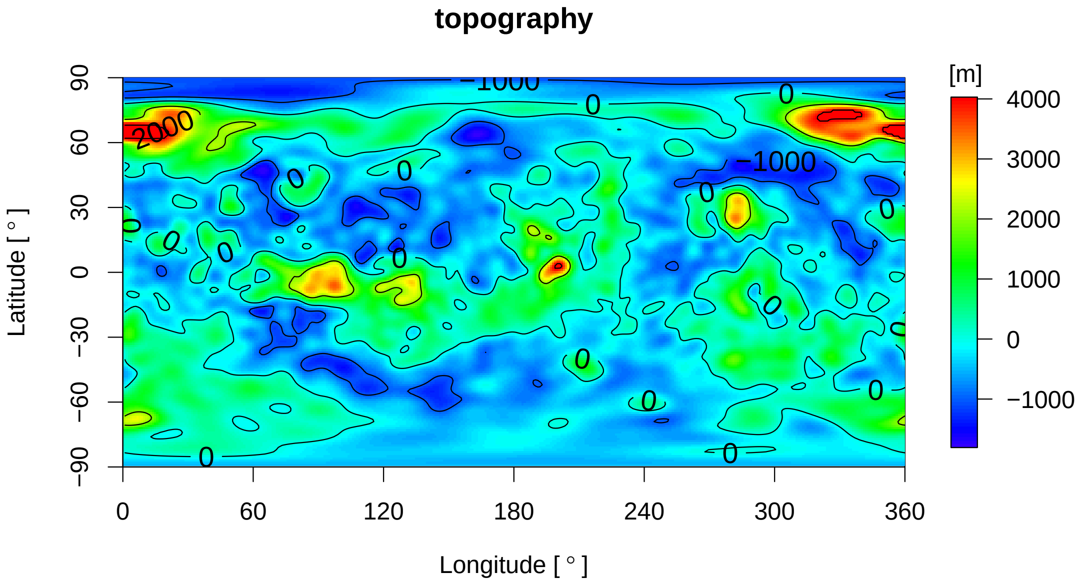

Figure 2.2: Topography for degrees 3-40.

250 000 years). This indicates that the planet is still volcanically active.

2.1.2 Mantle dynamics and structure

Numerous studies have used the gravity and topography observations to constrain the mechanisms that maintain the topographic features. The possible mechanisms include isostasy (Smrekar and Phillips, 1991), elastic flexure (Barnett et al., 2002) and mantle flow induced by density inhomogeneities (Simons et al., 1994; Pauer et al., 2006; Steinberger et al., 2010). Pauer et al. (2006) have performed the geodynamic inversion of the geoid and topography data in order to estimate the viscosity stratification of the Venus' mantle. Using a rather simplifying assumption, namely that the mass anomaly distribution does not vary with depth, they concluded, that the geoid and topography spectra between the degrees 2 and 40 can be well explained by the whole mantle flow model. One of their best fitting five-layer viscosity profiles has a relatively high-viscosity lithosphere (about 2 orders of magnitude difference with respect to the upper mantle) and shows a gradual increase of viscosity with depth by a factor of 40 in the underlying mantle.

These results are consistent with findings of Steinberger et al. (2010) who derived similar viscosity profile consistent with mineral physics. This profile has a $\sim$ 100 km-thick lithosphere, a 2.5-orders-lower viscosity upper mantle, a gradual increase of about 2 orders, and then the viscosity decrease in the lowest 500 km of the mantle by 2.5 orders of magnitude. For this profile they computed gravity and topography kernels, and then using these kernels, they computed the expected geoid-to-topography ratio (GTR). They found a good agreement with the observed ratio which indicates that long-wavelength topography is largely dynamically supported from the mantle. Further, they combined the kernels with the empirical power spectrum of density anomalies (inferred from the seismic tomography of Earth's mantle) to model the gravity power spectrum. A fit of observed and modelled gravity power spectra was good except for $2 \leq j \leq 4$, suggesting possibly much less density anomalies in this degree range than inferred from the Earth tomography.

Since the early nineties, the relationship between the topography and the geoid has been studied in the framework of the numerical models of thermal convection. The regional scale models of a single plume were used to put the first constraints on the mantle viscosity distribution on Venus. Kiefer and Hager (1991) tried to fit the geoid and topography of four selected plumes in a model with a depth-dependent viscosity, and concluded that their preferred model shows a moderate increase of viscosity in the lower mantle. Furthermore, they reported a trade-off between the viscosity increase and the Rayleigh number—the model with a lower Ra and a viscosity increase gave the same fit as the model with a higher Ra and constant viscosity beneath the lithosphere.

Smrekar and Parmentier (1996) studied the time evolution of the geoid and the GTR in a similar model but with temperature dependent viscosity. They concluded that both quantities change with time, and they used the GTR to estimate the evolutionary stage of several plumes on Venus—Beta, Atla, Western Eistla, and Imdr Regiones were estimated to overlie active or recently active plume, while Bell, Dione, and Themis Regiones seem to overlie a very late (or extinct) stage of plume. The effect of temperature dependent viscosity on the plume evolution and the predicted GTR were also studied by Solomatov and Moresi (1996) in a Cartesian model. They needed a rather thick lithosphere (200–400 km) to predict an average observed GTR and, for some plume regions, their stagnant lid was as thick as 500 km. Their preferred model was characterised by the Ra of $3 \cdot 10^7$. A relatively thick highly viscous lithosphere (about 200 km) is also consistent with the findings of Reese et al. (1999).

Though efficient, the Cartesian or cylindric models of a single plume may suffer from an incorrect geometry. It has been pointed out by King (1997) that the predicted geoid could vary by about 50% among the different model geometries (cylindrical, Cartesian and spherical axisymmetric). Therefore the spherical models—axisymmetric (Kiefer and Kellogg, 1998) or even fully 3D models (Yoshida and Kageyama, 2006) are important in interpreting the geoid and topography data. Another advantage of these global models is the interaction of the plumes with the background mantle flow and a smaller dependence on the initial conditions. On the basis of 3D calculations with temperature dependent viscosity, Yoshida and Kageyama (2006) required a viscosity contrast of about 5 orders of magnitude over the mantle plus a step-wise increase in viscosity at the upper-lower mantle boundary to produce a stagnant lid convection with a realistic number of plumes. Their geoid spectra correspond to the observed ones for a small viscosity jump at the upper—lower mantle boundary.

Armann and Tackley (2012) run several 2D numerical convection models (in spherical annulus geometry) over 4.5 billions years to examine the thermochemical magmatic and tectonic evolution of Venus. They presented models both in stagnant lid and episodic overturn regime. They were able to produce Venus-like amplitudes of topography and geoid in both modes, however, the fit was far from perfect. Viscosity in their models was strongly temperature-dependent and resulting in Earth-like radial profiles with upper mantle viscosity 10^{19}–10^{20} Pa s.

2.1.3 Inferring mantle viscosity stratification

Here we will use long and intermediate-wavelength spectra of geoid and topography to constrain viscosity stratification of the Venusian mantle. Viscosity is clearly the key parameter controlling the dynamic regime of the mantle, number of plumes etc., and is crucial for understanding the relationship between the dynamic topography and the geoid. This relationship is studied systematically here, in a large group of models with various viscosity profiles and varying several other flow model parameters. Using 3D spherical simulations of thermal convection in a model with depth-dependent viscosity it is tested whether the spectra of our predicted geoid and topography correspond to the observed ones. The results obtained for convection runs with different viscosity profiles (profiles from Pauer et al. (2006), isoviscous mantle, constant viscosity mantle with a highly viscous lithosphere, linearly increasing viscosity) are compared here and the effect of Rayleigh number is tested. Besides of the fit of the spectra, the characteristic flow patterns (namely the number of plumes developed) are also compared. Further, in a 2D spherical axisymmetric model, the effect of lateral viscosity variations and internal heating is studied. In the 2D models, we further evaluate the evolution of the plumes and compare their geoid and topography signature with the observations at selected upwelling structures on Venus.

When the time dependent convection models are considered, an important question arises, how to compare the model results with the observations. The observed geoid and topography represent one snapshot of the system evolution. As the characteristics of the models may vary with time significantly, it is not clear which snapshot of the model run should be used for the comparison with the observed data. Kiefer and Kellogg (1998) have shown in a 2D model that the time-dependent convection generates substantial variations of the geoid and topography in time. It may thus be difficult to use these quantities to constrain the parameters like Ra and acceptable profiles of mantle viscosity. Therefore, rather than looking on the correspondence between the observed and predicted data at one time instant, the time averages of the L_2-norm differences are shown for the models, where these quantities change with time substantially.

Parameter	Symbol	Value	Units
surface radius	r_{top}	6050	km
core radius	r_{cmb}	3110	km
gravity acceleration	g	8.6	m s^{-2}
reference density	ρ_0	4200	kg m^{-3}
coefficient of thermal expansion	α	$2.5 \cdot 10^{-5}$	K^{-1}
specific heat at constant pressure	c_p	1200	J kg^{-1} K^{-1}
thermal diffusivity	κ	$5 \cdot 10^{-7}$	m^2s^{-1}
density at the surface	$\Delta\rho_{top}$	3200	kg m^{-3}
density contrast at CMB	$\Delta\rho_{cmb}$	4300	kg m^{-3}
density of the core	ρ_C	12500	kg m^{-3}
temperature on the surface	T_{top}	731	K
temperature on the core-mantle boundary	T_{cmb}	3700	K
gravitational constant	G	$6.67{\cdot}10^{-11}$	N m^2 kg $^{-2}$
rate of internal heating	Q_v	$7.5 \cdot 10^{-9}$	W m^{-3}
Clapeyron slope	γ_{730}	$-2.8 \cdot 10^6$	Pa K^{-1}
density jump at 730 km	$\Delta\rho_{730}$	390	kg m^{-3}
width of the phase transition	d_{ph}^{730}	40	km

Table 2.1: Model parameters for Venus (Schubert et al., 2001; Yoshida and Kageyama, 2006)

2.2 Model Description

We use both 2D axisymmetric and 3D spherical models as described in paragraph 1.2. Parameters of the models are summarised in Table 2.1 and for the list of the models see Table 2.2.

Both the radial and the lateral resolutions vary among individual models depending on their *Ra*, viscosity stratification, and the presence of the lateral variations of viscosity. Typically, the cut-off degree of the spherical harmonic expansion is 170 for models with lower *Ra* ($\approx 10^6$) and 250 for models with higher *Ra* ($\approx 10^7$). The radial resolution varies between 5 km (boundary layers) and 30 km (middle mantle).

An initial temperature distribution was obtained by executing a run in a model with a relatively low *Ra* of 10^5 and a uniform viscosity. After reaching the statistically steady state, temperature distribution was used as an initial condition of subsequent model runs with variable viscosity and varying *Ra*. All results presented here are taken after the system reached a statistically steady state.

Four basic radial profiles were used here. Besides the viscosity profile A based on Pauer et al. (2006), there are three simple viscosity stratifications: constant viscosity mantle (B), model C with linearly increasing viscosity, and model D

	η'	η_{um} [Pa s]	Ra	IH
3D models				
3A8$\times 10^{20}$	Pauer et al. (2006)	$8 \cdot 10^{20}$	$7 \cdot 10^{6}$	no
3A2$\times 10^{21}$		$2 \cdot 10^{21}$	$2.8 \cdot 10^{6}$	
3A6$\times 10^{21}$		$6 \cdot 10^{21}$	$9 \cdot 10^{5}$	
3A3$\times 10^{22}$		$3 \cdot 10^{22}$	$2 \cdot 10^{5}$	
3A5$\times 10^{22}$		$5 \cdot 10^{22}$	$1 \cdot 10^{5}$	
3A2$\times 10^{21}$IH	Pauer et al. (2006)	$2 \cdot 10^{21}$	$2.8 \cdot 10^{6}$	yes
3B5$\times 10^{21}$	constant	$5 \cdot 10^{21}$	$2.61 \cdot 10^{7}$	no
3B4$\times 10^{22}$		$4 \cdot 10^{22}$	$3.3 \cdot 10^{6}$	
3B1$\times 10^{23}$		$1 \cdot 10^{23}$	$1.3 \cdot 10^{6}$	
3C1$\times 10^{21}$	linear increase	$1 \cdot 10^{21}$	$3 \cdot 10^{6}$	no
3C3$\times 10^{21}$		$3 \cdot 10^{21}$	$1 \cdot 10^{6}$	
3C5$\times 10^{21}$		$5 \cdot 10^{21}$	$6 \cdot 10^{5}$	
3C3$\times 10^{22}$		$3 \cdot 10^{22}$	$1 \cdot 10^{5}$	
3D4$\times 10^{21}$	lithosphere	$4 \cdot 10^{21}$	$6.1 \cdot 10^{6}$	no
3D5$\times 10^{21}$		$5 \cdot 10^{21}$	$4.9 \cdot 10^{6}$	
3D1$\times 10^{22}$		$1 \cdot 10^{22}$	$2.5 \cdot 10^{6}$	
3D5$\times 10^{22}$		$5 \cdot 10^{22}$	$5 \cdot 10^{5}$	
2D models				
8 models varying Ra	Pauer et al. (2006)	from $1 \cdot 10^{20}$ up to $5 \cdot 10^{23}$	from $1 \cdot 10^{4}$ up to $5.48 \cdot 10^{7}$	no
2A2$\times 10^{21}$	Pauer et al. (2006)	$2 \cdot 10^{21}$	$2.8 \cdot 10^{6}$	no
2A2$\times 10^{21}$IH				yes
2B4$\times 10^{22}$	constant	$4 \cdot 10^{22}$	$3.3 \cdot 10^{6}$	no
2B4$\times 10^{22}$IH				yes
2C5$\times 10^{21}$	linear	$5 \cdot 10^{21}$	$6 \cdot 10^{5}$	no
2C5$\times 10^{21}$IH				yes
2D1$\times 10^{22}$	lithosphere	$1 \cdot 10^{22}$	$2.5 \cdot 10^{6}$	no
2D1$\times 10^{22}$IH				yes
2A2$\times 10^{21}$LV0	Pauer et al. (2006)			yes
2A2$\times 10^{21}$LV1	Pauer et al. (2006)			yes
2A2$\times 10^{21}$LV2	Pauer et al. (2006)			yes
2A2$\times 10^{21}$LV3	Pauer et al. (2006)			yes

Table 2.2: List of presented models. η' denotes radial viscosity profile (see Fig. 2.3), η_{um} is the upper mantle viscosity, Ra is Rayleigh number and IH denotes whether internal heating is or is not included in the model.

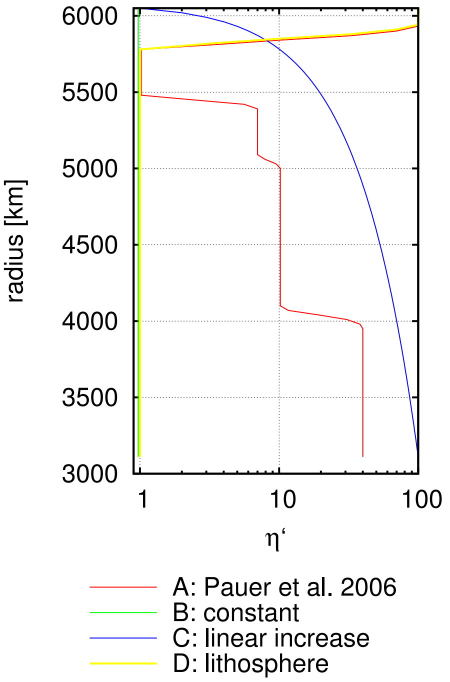

Figure 2.3: Four profiles of the radially dependent dimensionless viscosity $\eta^{'}(r)$ (cf. eq. (2.1)).

with a high a viscosity lithosphere underlain by an isoviscous mantle (Fig. 2.3). In 2D models lateral variations of viscosity were added on top of the depth variations of profiles A–D. These lateral variations of viscosity follow exponential approximation of the temperature dependence (Reese et al., 1999):

$$\eta(r,T) = \eta_{um}\eta'(r)\exp\left[-\ln c\,\frac{T-T_{um}}{T_{cmb}-T_{top}}\right]. \tag{2.1}$$

Here η_{um} is a constant (its choice controls Ra), $\eta' = \eta'(r)$ is a dimensionless reference viscosity at radius r (profiles A–D), T_{um} is the temperature of the upper mantle corresponding to η_{um} and c is a non-dimensional parameter that controls temperature-dependent viscosity variations. For models with constant viscosity $c = 1$, for models with temperature-dependent viscosity variations of 1, 2, and 3 orders, the parameter $c = 10, 100$ and 1000 respectively.

In the models where the effect of internal heating Q_v is included, prescribed rate ensures that the internal heating accounts for about 50% of the total surface heat flux. An estimate of the total amount of radiogenic heat production on Venus made on the base of scaling the Earth's value would make 16 TW. The value used here produce only 6 TW of internal heating, which may not be unrealistic, as it has been suggested (Smrekar and Sotin, 2012) that total internal heat budget may be even lower in case of Venus—as low as 3 TW.

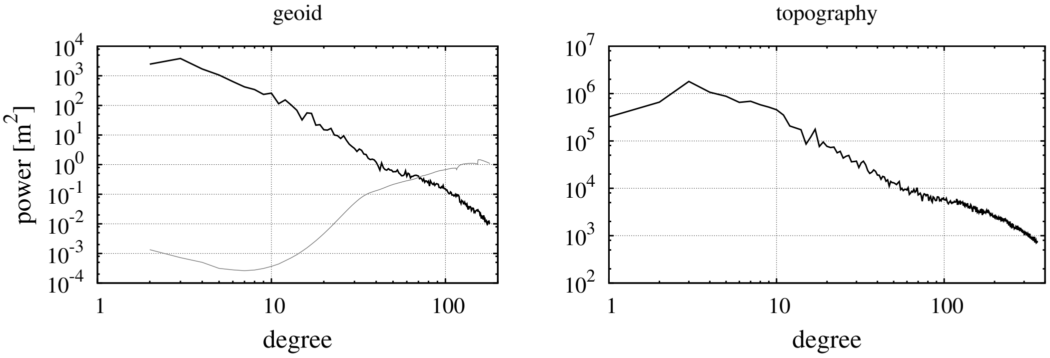

Figure 2.4: Spectra of the geoid (left) and topography (right) plotted in log-log scale. Grey line in geoid plot shows uncertainty of the geoid data.

On Venus, phase transitions are expected to occur deeper in the mantle in comparison to Earth (Schubert et al., 1997)—exothermic phase transition at 440 km and endothermic at 740 km. In some models effect of an endothermic spinel-perovskite phase change was included with parameters given in Table 2.1.

2.3 Data

The power spectra of observed geoid and topography plotted in a log-log scale (Fig. 2.4) show two changes of the slope: a more prominent one at about the degree of 40 and a slightly less pronounced but still significant one around the degree of 10. It has been hypothesised that the change of the slope at degree 40 is related to the change of the mechanism maintaining the geoid (topography) anomalies—the geoid of Venus is probably of a predominantly dynamic origin up to the degree 40 (Pauer et al., 2006; Steinberger et al., 2010). We will omit here the anomalous degree 2—both the admittance (geoid-to-topography ratio in spectral domain) and correlation for degree 2 are significantly smaller than for higher degrees which may suggest different origin than for signal at higher degrees (Wieczorek, 2007). In this work, we will therefore restrict observed and model geoid and topography analysis to the spectral range 3-40. Geoid anomalies at this spectral range are displayed in Fig. 2.1 and topography in Fig. 2.2.

In order to quantify the agreement between the observed and the predicted data, the quantity L_2d is introduced to evaluate the difference between the spectra in L_2-norm. Instead of comparing directly the power on individual degrees, we rather look at the slope of the geoid spectrum (Čížková et al., 1996). The slope should be characteristic for a given dynamic model, and is less affected by the errors of individual degrees. Since the observed log-log spectra change the slope at degree 10, each model can be characterised by two logarithmic slopes—one for degree range 3–9 and the other one for degrees 10–40. We are interested not only in the slopes but also in the amplitudes. Therefore, the decaying log-log spectra is approximated by two linear regression lines ($l^{3-9}(j)$ for degrees 3–9 and $l^{10-40}(j)$ for degrees 10–40) and then the difference between these linear functions of the predicted and observed geoid is calculated. The L_2-norm difference L_2d is then defined as:

$$L_2d = \sqrt{\frac{\sum\limits_{j=3}^{9}(l^{3-9}_{obs}(j) - l^{3-9}_{pred}(j))^2 + \sum\limits_{j=10}^{40}(l^{10-40}_{obs}(j) - l^{10-40}_{pred}(j))^2}{38}}, \qquad (2.2)$$

where $l^*_{obs}(j)$ and $l^*_{pred}(j)$ are the linear approximations of the observed and predicted spectra.The L_2d is normalised by the number of degrees, thus giving an average difference (L_2d equal to 1 means that the observed and predicted spectra have one order of magnitude difference on average). Similarly, the L_2d difference is calculated for the topography.

Besides the power spectra, we also compare the shape of the geoid and the topography anomaly above the plume developed on the pole in the 2D axisymmetric model with several topographic rises on Venus. Four upwellings were chosen—Atla (0.9°N, 194.6°E), Beta (22.7°N, 281.0°E), West Eistla (22.0°N, 352.4°E) and Themis Regio (11.0°N, 14.1°E), thus covering all three types of topographic rises. In order to compare the observed rises with the axially symmetric ones in 2D models, the observed anomalies are averaged here to get an axisymmetric shape. The degree range is chosen according to the diameter of the regiones (j=10–40) in order to avoid a long-wavelength shift. The difference between the observed and predicted data is evaluated using the following quantity:

$$A_vd = \frac{\int_\vartheta |o_{obs}(\vartheta) - o_{pred}(\vartheta)|\mathrm{d}\vartheta}{\int_\vartheta |o_{obs}(\vartheta)|\mathrm{d}\vartheta}, \qquad (2.3)$$

where $o_{obs}(\vartheta)$ and $o_{pred}(\vartheta)$ are observed, and predicted geoid and ϑ is the colatitude measured with respect to the centre of the plume. Integration range is $\vartheta = [0, 10]$ degrees, respecting the diameter of the four regiones considered. The A_vd equal to 0.1 yield a 10% difference between the observed and predicted data, A_vd of 1 means that the observed and predicted data differ by 100%. Similarly, A_vd is defined for topography.

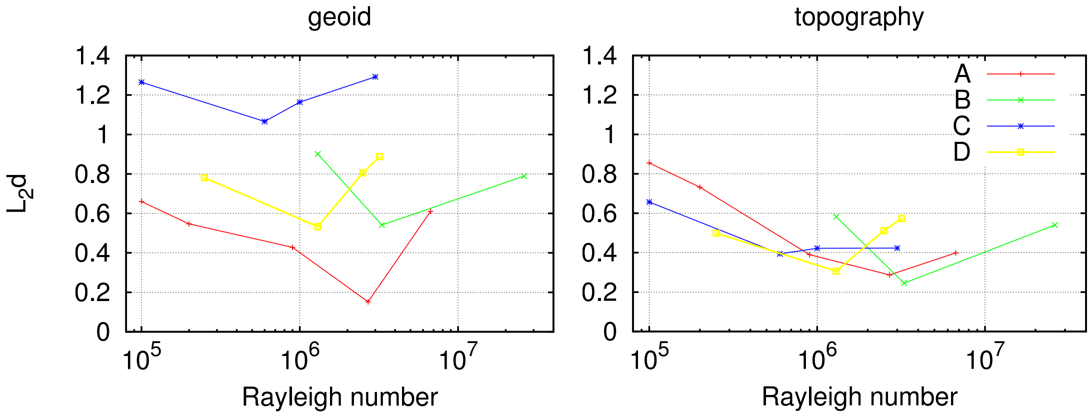

Figure 2.5: The difference L_2d (eq. (2.2)) between the observed and predicted geoid (left) and topography (right) for four viscosity profiles as a function of the Rayleigh number.

2.4 Results

2.4.1 3D models

For each 3D model, we have a time series of at least 1 Ga in a statistically steady-state. Before analysing these results, we should check how much do the spectra change with time, and whether one time snapshot can be representative of a given model. In case of 3D models, we have found that although the flow pattern changes with time, the character of the spectra—its slope on both long and intermediate wavelengths—is stable, and the conclusions could be drawn on the basis of one snapshot.

First, let us discuss the influence of upper mantle viscosity η_{um} (cf. eq. (2.1)). Though the geoid undulations are only dependent on the relative variations of viscosity with depth and not on its absolute value, the latter one defines the Rayleigh number, and thus the convection vigour and the character of the density anomalies. Therefore, it affects the geoid considerably. Fig. 2.5 demonstrates the sensitivity of the geoid and topography to the (volume averaged) Rayleigh number. The upper mantle viscosity η_{um} varies in the range $8 \cdot 10^{20}$–$1 \cdot 10^{23}$ Pa s while other parameters are fixed, so Rayleigh number changes in the range $9 \cdot 10^4$–$2.6 \cdot 10^7$. Clearly, the spectra are sensitive to the upper mantle viscosity—Rayleigh number. For each viscosity profile (A–D) one model with best fit in the sense of L_2d is obtained. The preferred value of Rayleigh number is usually found around 10^6 (η_{um} varies between 10^{21} and 10^{22} Pa s). In case of the viscosity profile A, the best fit is obtained for a model 3A2$\times 10^{21}$ with the upper mantle viscosity $\eta_{um} = 2 \cdot 10^{21}$ Pa s (average $Ra = 3 \cdot 10^6$). The best fitting constant viscosity model

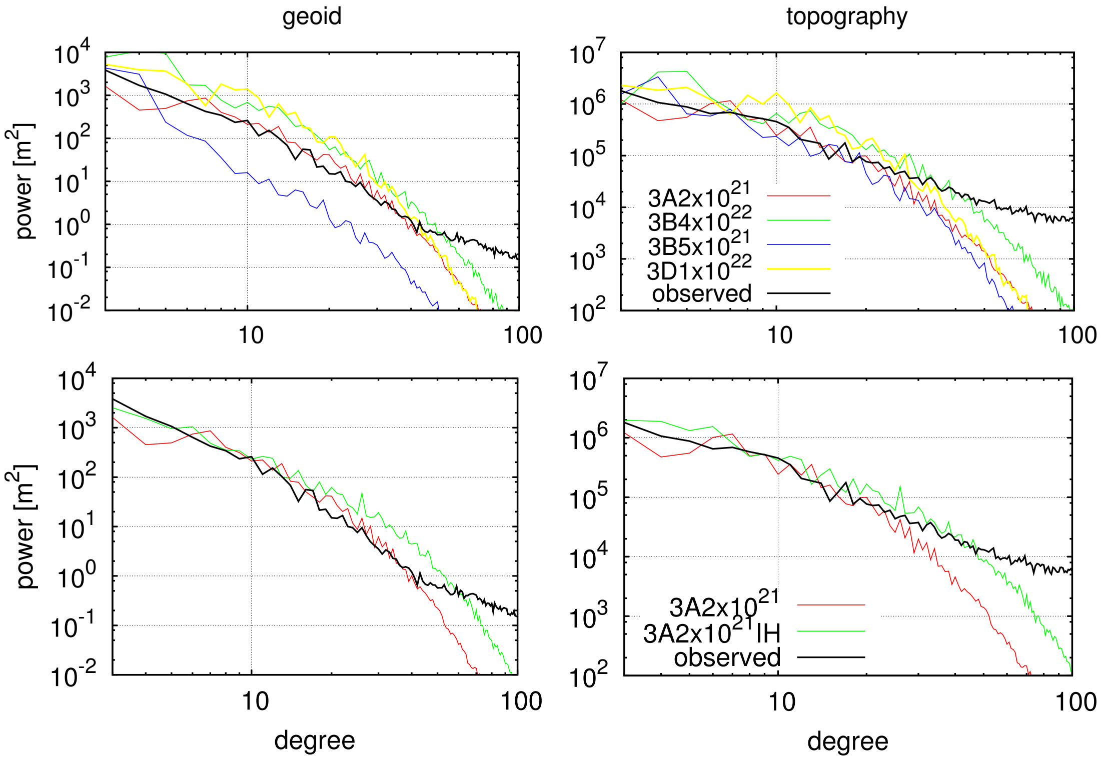

Figure 2.6: Power spectra of the geoid (left) and topography (right) of Venus. Top panels show results for four different viscosity profiles—each for its ideal *Ra*. Bottom panels show again the model 3A2×10^{21} (without internal heating and phase transition—red line) and model 3A2×10^{21}IH with phase transition and internal heating (green line). Black line shows the spectrum of the observed data.

3B4×10^{22} has $\eta_{um} = 4\cdot10^{22}$ Pa s ($Ra = 3\cdot10^6$). Linearly increasing viscosity (model 3C5×10^{21}) produces the best fit for the $\eta_{um} = 5\cdot10^{21}$ Pa s (average $Ra = 6\cdot10^5$). Finally profile D with a stiff lithosphere prefers the upper mantle viscosity of $\eta_{um} = 10^{22}$ Pa s with average $Ra = 10^6$ (model 3D1×10^{22}).

Fig. 2.6 shows the geoid (top left panel) and topography (top right panel) spectra of best fitting models for each viscosity profile (A–D). Black lines give the spectra of the observed quantities. Let's look at the geoid first. Both models B and D (green and yellow lines) overestimate the geoid by about the half an order of magnitude. Model C (blue line) is successful at long-wavelengths (degrees 3 and 4) but then deviates from the observed spectrum and underestimates the signal. Clearly, as for the geoid, the best fitting model is A that explains the observed data at degrees 5–40 very well. Let's now look at topography. Although models B and D have slightly better fit for topography than geoid, they still overestimate observed data. Both models A and C correspond with data quite well up to degreee 20.

Bottom panels of Fig. 2.6 show the effects of phase transition and internal heating. Red lines show the model $3A2\times10^{21}$ without a phase transition, and internal heating, the green line is for the model that incorporates both effects. Clearly, including the internal heating that suppresses the plume activity improves the intermediate-wavelength topography fit but decreases the geoid fit. The differences between the purely bottom heated case and the model partly heated from within are however not strikingly high.

Above degree 40 the predicted spectral slopes do not correspond for any model. At about that degree, the slopes of the observed geoid and topography change, thus indicating that possibly different mechanisms are responsible for the generation of the geoid and topography on the shorter wavelengths. That is in agreement with the hypothesis, that the long and intermediate-wavelength part of the geoid and topography have purely dynamic source, while above the degree of 40 they are of a predominantly lithospheric origin (Pauer et al., 2006).

One representation of the convection planform for each of the four above mentioned models is shown in Fig. 2.7 (each of them for the same time instant as the spectra in Fig. 2.6). The model $3D1\times10^{22}$ with the constant viscosity under the stiff lithosphere (Fig. 2.6d) has a rather warm mantle, and thus is characterised by a vigorous plume activity, with the total number of plumes of about 30. That is probably too much—there should be about 10 major plumes on Venus (Smrekar and Parmentier, 1996; Smrekar et al., 2010). Models A–C are generally in agreement with that criterion.

Four 3D models show rather different convection patterns. The differences are clear even in one snapshot (Fig. 2.8) but become even more apparent when looking on the time evolution. This is illustrated in Fig. 2.8. It shows time evolution of temperature (2000 K isosurface) at the depth of 1900 km (this spherical layer is expanded into plane). Model $3A2\times10^{21}$ (Fig. 2.8a) is dominated by sheet-like upwellings with plumes at their intersection which tend to move slightly but are persistent over long time period. Model $3B4\times10^{22}$ (Fig. 2.8b) shows similar behaviour but the plumes wander through the mantle and the convection looks more vigorous. Case $3C5\times10^{21}$ (Fig. 2.8c) is different from all other models. There are 7 solitary plumes that remain fixed for whole 2 Ga period displayed. Last model $3D1\times10^{22}$ (Fig. 2.8d), on the contrary shows vigorous convection with high number of relatively thin plumes, which change both their position and shape rapidly.

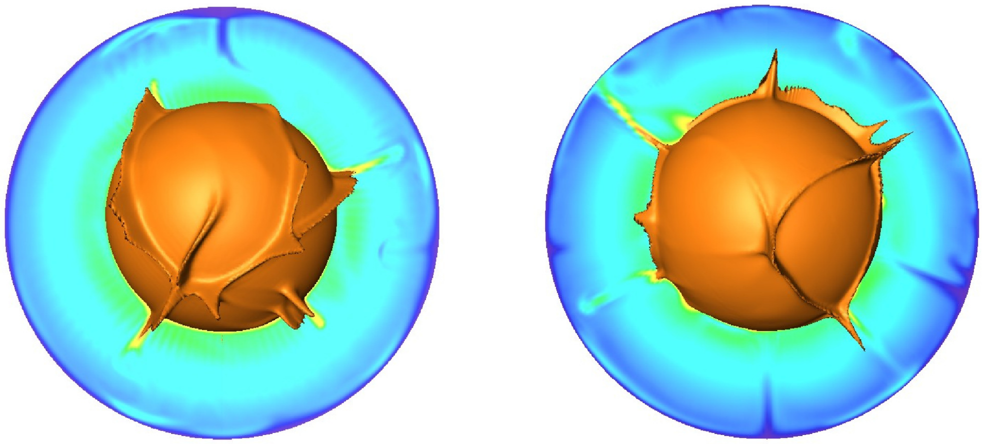

(a) 3A2$\times 10^{21}$ **(b)** 3B4$\times 10^{22}$

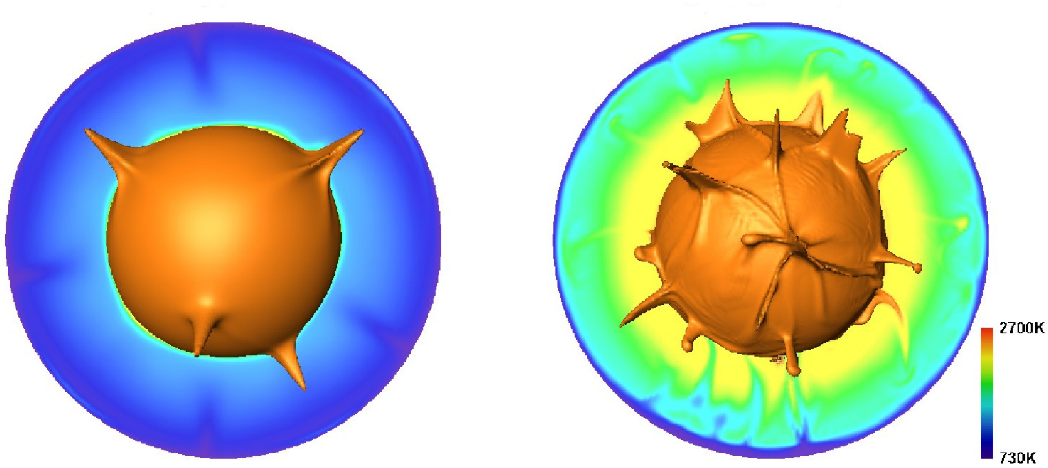

(c) 3C5$\times 10^{21}$ **(d)** 3D1$\times 10^{22}$

Figure 2.7: One snapshot of the temperature field in four convection models: a) viscosity profile A (3A2$\times 10^{21}$), b) profile B (3B4$\times 10^{22}$), c) profile C (3C5$\times 10^{21}$) and d) profile D (3D1$\times 10^{22}$) for their ideal Ra. Shown isosurface corresponds to a temperature of 2500 K.

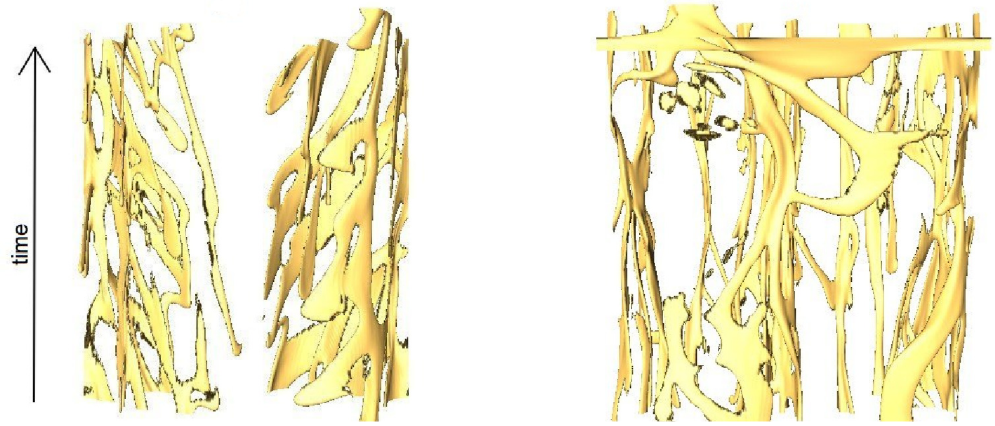

(a) 3A2$\times 10^{21}$ **(b)** 3B4$\times 10^{22}$

(c) 3C5$\times 10^{21}$ **(d)** 3D1$\times 10^{22}$

Figure 2.8: Time evolution of plumes for four 3D models (same as in Fig. 2.7). Each panel shows time evolution (vertical direction) of temperature isosurface of 2000 K at a depth of 1900 km. Time span is 2 Ga.

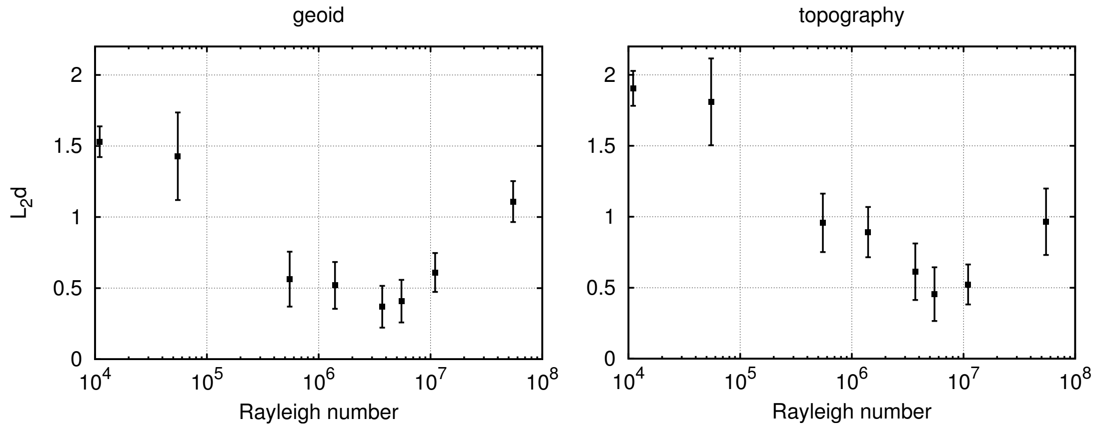

Figure 2.9: The difference L_2d between the observed and predicted geoid (left) and topography (right) in 2D models as a function of the Rayleigh number. The depth viscosity profile A was used.

2.4.2 2D models

First, we should note, that the 2D spectra of the geoid and the topography have different character than previously discussed spectra of the 3D models. Spectra of the 2D models are much more oscillatory and contrary to the 3D models, they vary with time considerably. Therefore rather than one value it is better to show time average with standard deviation taken over the whole calculation (in a statistically steady-state).

Fig. 2.9 (similarly to Fig. 2.5) shows the sensitivity of the geoid and the topography to the Rayleigh number. It depicts the L_2d difference between the observed and predicted spectra for the viscosity profile A. Similarly to the 3D models (cf. Fig. 2.5), the best fit is obtained for the (volume averaged) Rayleigh number of about $3 \cdot 10^6$. Such correspondence between the 2D and 3D results may suggest that the plumes indeed are the features controlling the style of the flow, and therefore, a 2D approximation could be used to describe the basic character of the flow.

Fig. 2.10 demonstrates the effect of internal heating. We have 10 models with different parameters (viscosity profile, Rayleigh number) without internal heating, and 10 corresponding models where internal heating was included. Fig. 2.10 gives scatter plot of L_2d of these models. Majority of the points is accumulated under the black identity line which means that the addition of the internal heating generally improves the L_2d fit of our models. The effect is larger when looking at the topography—almost all models (except one) have a better topography fit when internal heating is included, while the effect on the geoid is not so obvious. Some models have even worse fit with internal heating. That is in accordance

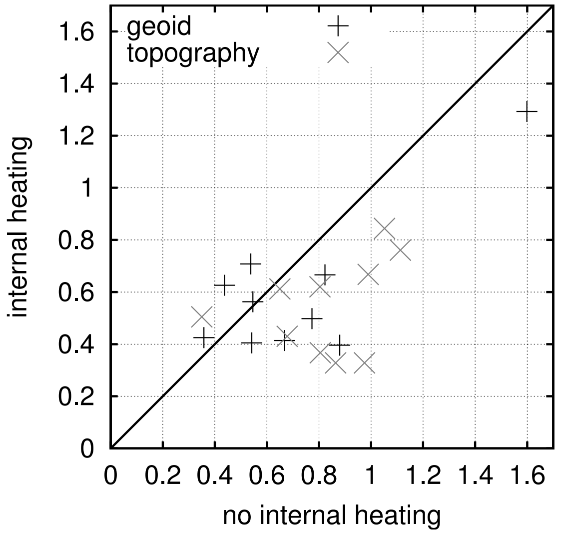

Figure 2.10: Scatter plot shows the effect of internal heating. Each cross represents two models. Those two models have the same viscosity profile (A–D) and the same Ra and one of them is without internal heating and one with internal heating. Position in scatter plot is given by L_2d without internal heating (horizontal axis) and by L_2d with internal heating (vertical axis) of the model pair.

with the results of 3D model runs (Fig. 2.6).

Further, the effects of the laterally variable viscosity were tested. For that purpose, we use four models 2A2$\times$10^{21}LV0–3 with the depth viscosity stratification of model A, but now the viscosity varies also laterally by 0-3 orders of magnitude with temperature (see eq. (2.1)—parameter c =1, 10, 100, 1000). Results are summarised in Fig. 2.11. Clearly, the moderate lateral variations of viscosity do not improve the fit to the observed geoid and topography. Actually, the models with lateral variations have slightly worse fits to observed quantities. We thus conclude that mild lateral viscosity variations do not play a major role, though we admit that a more detailed analysis of Ra dependence of L_2d fit should be performed for laterally variable cases in order to draw stronger conclusions.

Up until now, only the power spectra of the geoid and the topography were examined as the only model output to be compared with the data. Let us now look at another possible feature, that could be used to discriminate between the successful and unsuccessful models, and that is the actual shape of the geoid and topography above the assumed mantle plumes on Venus. Though there are certain doubts about the origin of some uplifted areas of the Venus' topography, others are generally believed to be associated with the mantle plumes. Four upwelling areas (Atla, Beta, West Eistla, and Themis) were chosen, and their observed topography and geoid are compared to the topography and the geoid

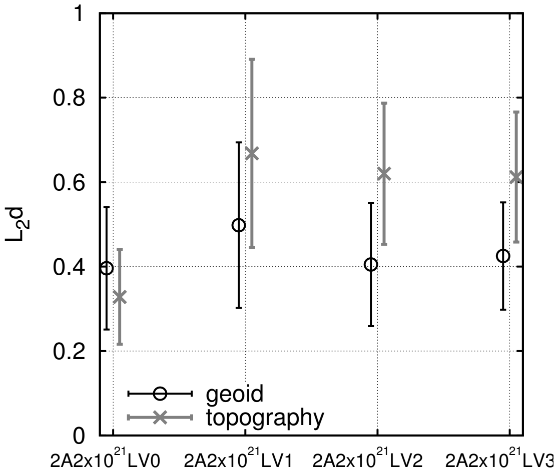

Figure 2.11: The difference L_2d between the observed and predicted data in four models with increasing lateral variations of viscosity (0, 1, 2 and 3 orders of magnitude). The depth viscosity profile A was used.

predicted in the polar plume area in the 2D axisymmetric model. We have a time evolution of 2 Ga for four models (the most successful for each viscosity profile - $2A2\times10^{21}$IH, $2B4\times10^{22}$IH, $2C5\times10^{21}$IH and $2D1\times10^{22}$IH), and evaluate the A_vd error (eq. (2.3)) in each time instant. The A_vd error is mostly high, thus indicating a poor correspondence between the predicted and observed topography and geoid over the plume. At certain moments, however, this error drops and a quite good fit ($A_vd < 0.1$, that means less than 10% difference) of the observed and predicted geoid or topography is observed. The results are shown in Fig. 2.12, which shows the histograms of the A_vd. When calculating the count, A_vd of both the geoid and topography were assumed. First let us look on the left panel showing the histograms for four viscosity stratifications A (red), B (green), C (blue) and D (yellow). Each histogram includes the A_vd of all four regiones (Atla, Beta, Western Eistla and Themis). The successful model characterised by a low A_vd should have a count maximum at low A_vd. Clearly, it is difficult to identify a really succesful model here as the moments with good fit are quite rare in all models. Model A may be considered the best, the count maximum at low A_vd is however not very significant.

We should note here, that the correspondence between the observed and the predicted topography and geoid differs among the considered Regia. Our models are more successful in explaining these quantities in Atla and Beta Regia, while for Western Eistla and Themis the fit is considerably lower. That is demonstrated in Fig. 2.12, on the right panel, where the histograms of A_vd are shown for individual Regia and for the best fitting model $2A1\times10^{21}$IH. Fig. 2.13 illustrates

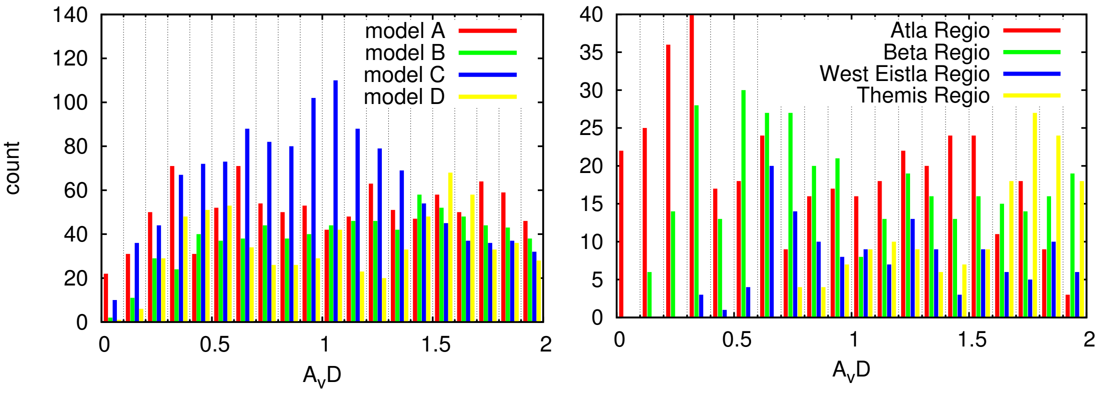

Figure 2.12: Histograms illustrating the distribution of the $A_v d$ (difference between observed and modelled data). Counts on the vertical axis denote the number of time instants giving the appropriate $A_v d$ - the higher the count is the more often model reaches the given $A_v d$ value. Left: comparison of four convection models based on profiles A, B, C and D. Counts are sums for four regiones (Atla, Beta, Western Eistla and Themis) both geoid and topography is considered. Right: distribution of the $A_v d$ values for individual regiones in most successful model A (both geoid and topography).

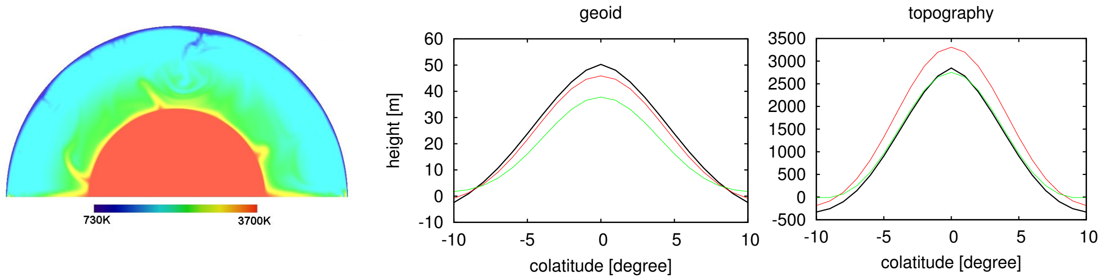

Figure 2.13: Left: Temperature field of the best fitting 2D model at one time instant. Middle panel: Observed geoid in Atla Regio (black line) with the model prediction (model 2A2x10^{21}IH). Green and red lines give the predictions in two different snapshots. Geoid and topography are calculated for degrees 10-40. Right: The same, but for topography.

the characteristic temperature distribution in the best fitting 2D model ($2A1 \times 10^{21}$IH) together with the observed geoid and topography in Atla Regio and the predicted quantities above the polar plume. It may be interesting that the worst fit is obtained for Themis Regio which has been suggested to overlay very late stage (possibly extinct) plume (Smrekar and Parmentier, 1996).

2.5 Concluding remarks

On the basis of combined evidence coming from the spectral fit, number of plumes developed in the mantle and the fit to the observed shape of the geoid and topography in several regiones on Venus, we can generally conclude, that profile A characterised by a 200 km thick lithosphere followed by a gradual increase of viscosity with depth gives the best correspondence between the observed and predicted quantities, though none of the models fits observed data perfectly. The best fitting model has the upper mantle viscosity of $2{\cdot}10^{21}$ Pa s, thus giving an average Rayleigh number of $2.8 \cdot 10^6$. For all viscosity profiles, the observed spectra and the predicted spectra coincide only up to the degree of about 40. At higher degrees the slopes of the predicted spectra differ from the observed ones considerably thus indicating other then dynamic origin of the geoid and topography anomalies.

While in 3D cases the spectra of the geoid and the topography are stable over time (the slopes of the log-log spectrum vary only very weakly), in 2D models the spectra themselves are much more oscillatory and their slopes oscillate quite wildly over time. Despite these differences, both 2D and 3D model runs prefer the same upper mantle viscosity. That may suggest that the plumes are indeed the main dynamic features controlling the dynamic processes in the Venus' mantle and the 2D axisymmetric model provides its good approximation.

In present work, it is assumed that all topography is the result of convection motion (dynamic topography). As recently suggested by Orth and Solomatov (2011), Venusian topography could be alternatively explained in the terms of the thermal isostasy of the laterally variable stagnant lithosphere. However, the amplitude of the stagnant lid thickness variations strongly depends on the convection model (e.g. internal vs. bottom heating, Newtonian vs. non-Newtonian viscosity). In some models the dynamic topography and the geoid contribution due to the flow below the lid may be comparable or larger than the lithosphere contribution (Solomatov and Moresi, 1997, 2000). Presented results could therefore be considered as an end-member case and the ratio of the stagnant lid thickness variations vs. convection induced topography should be subject to a further research. In combination with these two mechanisms the effects of the ratio of the internal and bottom heating should be tested in more detail.

The results of the presented 3D models are inevitably negatively influenced by the absence of the lateral variations of viscosity. However, it has been shown by Solomatov and Moresi (1996), that under the high viscosity stagnant lid the temperature variations are rather small and therefore also the temperature induced lateral variations of viscosity may not play a key role. That is in a good agreement with the results of 2D models, where the moderate temperature related lateral variations of viscosity do not improve the fit to the data. Further, Tackley (1996) pointed out, that the depth viscosity variations play primary role in influencing the dynamic regime of the mantle. Thus, though the thermally induced lateral variations of viscosity are potentially important in the 3D models due to the lithospheric thinning (Solomatov and Moresi, 1996; Moore et al., 1999), 3D results for a model with a high viscosity lid should be able to describe the basic features of the Venus mantle dynamics.

3. Mercury

Mercury is the smallest of the terrestrial planets and nearest to the Sun, orbiting once every 87.969 Earth days. Its orbit has high eccentricity (0.2056), the average distance from the Sun is 57,9 million km and it has a 3:2 spin-orbit resonance (it spins 3 times per 2 orbits around Sun).

Although the Mercury is not too far from the Earth, it is the least explored inner planet. Observations from the Earth are complicated due to Mercury's proximity to the Sun, which also eliminates Mercury as a target for Hubble telescope. Any spacecraft launched from the Earth must deal with a very hostile thermal environment. Moreover, as the planet is located deep in the gravity well of the Sun, a considerable amount of energy is needed to reach it. Up to now, only two spacecraft reached Mercury: Mariner 10 and MESSENGER.

Mariner 10 was NASA probe which started in November 1973 and its objective was to obtain information about the atmosphere, surface, and the physical characteristics of Mercury and Venus. During the Venus flyby, Mariner 10 took 2400 photographs of Venus and accomplished some atmospheric research. Then it continued on its way to Mercury. From March 1974 to March 1975 it realised three flybys, then the mission was terminated. Mariner sent more then 2700 photographs of Mercury's surface (resolution 100 m–4 km) but it was able to map only about 45% of the surface. Measurements provided data for estimating the degree 2 harmonic coefficients of the gravity field although the errors were quite large (50% for C_{22}). The mission did not involve surface composition measurements, thus it provided little guidance for compositional or thermal models of the interior.

However, the mission made an important and surprising discovery. The spacecraft passed nearly directly above the rotational north pole of the planet and measured a dipolar magnetic field. The variation and magnitude of this field along the spacecraft trajectory implied a planetary field of an internal origin. Although the field is relatively weak it appears to be too strong to be generated by remnant magnetism (Ness et al., 1976).

MESSENGER (MErcury Surface, Space ENvironment, GEochemistry and Ranging) is a NASA probe as well. It was launched in August 2004 and after two Venus flybys and three Mercury flybys it was put into the orbit in March 2011 and it started research. Its orbit is near-polar, period is 12 hours and the altitude is between 200–15 000 km. The main objectives of the orbital phase of the mission are determination of Mercury's gravity field (which can improve our understanding of the internal structure of the planet), state of the core, the thickness of the crust, and the tectonic and thermal history. Science equipment includes: two cameras that are able to observe the surface with a resolution up to 18 m; spectrometers for examining chemical composition of the crust; magnetometer to detect spatial distribution of the magnetic field; laser altimeter (resolution 30 m) and radio science equipment to measure probes' speed and the distance from the Earth, which will be used for gravitational field measurement. MESSENGER finished its one-year orbit mission in March 2012, then the mission was extended twice and it ended in April 2015.

In the near future, the exploration of Mercury should continue through BepiColombo mission. BepiColombo is a joint project of European Space Agency and Japanese Aerospace Exploration Agency. It is planned to be launched in 2017 and to reach the orbit in 2024 (it should orbit for 1 year). During its way to the orbit it should accomplish 2 Venus and 5 Mercury flybys. It is designed to have a complementary orbit to that of MESSENGER and it will extend geochemical, spectral, and photometric mapping of the planet (McNutt et al., 2004). It should be better adapted for estimating the gravity field than MESSENGER—up to degree 20 with maximum error 10% and coefficients C_{20} and C_{22} will be known with accuracy about 0.01%.

3.1 Structure and dynamics of Mercury

3.1.1 Surface

Mercury has extremely thin atmosphere (in principle vacuum; pressure about 10^{-12} bar) consisting mainly of helium, oxygen, sodium and hydrogen (Domingue et al., 2007). As the planet has basically no atmosphere to hold stable temperature and due to its proximity to the Sun, the temperature of the surface differs considerably between the sun-exposed and reversed side—from 90 K to 725 K (Strom, 1997). Despite the high surface temperatures, convincing evidence for a presence of water were found by Mariner 10 and on-ground radiotelescopic measurements. Strong reflection of radar signal and the polarization ratios in the polar region are interpreted as a presence of ice. Mercury's rotational axis is nearly perpendicular to its ecliptic plane, thus in the cratered polar area, there are regions never enlightened by the Sun.

Surface of the Mercury is dominated by craters and it has a lunar-like character with the average age of more than 4 Ga. Mercury's unique feature, lobate scarps (great curved cliffs) are believed to be high-angle thrust faults. Their length is from 20 to 500 km and heights from 100 m to about 3 km (Strom, 1997). They are probably caused by contraction of the planet during its cooling process. Recent estimates based on images of tectonic features yield value of the global contraction as high as 4 km (Di Achille et al., 2012). Other remarkable formation on the Mercury's surface is Caloris Basin, a huge impact crater with 1550 km diameter.

Images from MESSENGER provided evidence for a global volcanic activity in the early history of the planet. Images confirm that volcanism was a widespread process in the post-heavy bombardment epoch. On the other hand, there are no major shield volcanoes and little evidence for mantle hot spots was found (Head et al., 2009). Investigation of impact basins revealed that some of them are as young as 1 Ga (or maybe even younger) (Prockter et al., 2010). Blewett et al. (2011) described the Mercury's unique surface features—hollows (irregularly shaped depressions). They hypothesised that the hollows may be created by processes involving volatile compounds that could still be active.

Nittler et al. (2011) used the data from MESSENGER X-ray spectrometer (XRS) to constrain the major-element composition of the surface rocks. They found higher Mg/Si ratio and lower Al/Si and Ca/Si ratios than observed in the terrestrial and lunar crusts. This can provide a clue to what the precursor materials were.

Peplowski et al. (2011) reported average surface amounts of radioactive elements (potassium 1150 ± 220 ppm, thorium 220 ± 60 ppb and uranium 90 ± 20 ppb). This observation supports the formation from a volatile-enriched material. It also indicates that the internal heat production has declined significantly since planet's formation, supporting other evidence of a widespread volcanism at the end of the heavy bombardment and only a limited volcanic activity since then. This data is based on MESSENGER gamma-ray spectrometer (GRS) and it was measured in the northern hemisphere, north of 20°S latitude. Peplowski et al. (2012) specified the previous data on the basis of measurements from wider area. Potassium abundances vary from 300 to 2400 ppm over the surface. On the other hand, thorium abundances do not vary significantly in the terms of GRS spatial resolution (~ 1000 km). The relationship of K abundances with the main geological regions is not clear due to the poor resolution of GRS but, overall, the highest K abundances are found in the northern volcanic regions while the Caloris basin has low K abundances. They also found anti-correlation of K amounts with the temperature hypothesising that K may be lost from hot regions to exosphere or redistributed to polar regions.

3.1.2 Internal structure

Mercury's total mass of 3.302×10^{23} kg and mean radius of 2440 km implies that it has extremely high mean density 5440 kg/m^3 which is a value similar to the Earth. Considering the uncompressed density (average density materials would have at zero pressure) it is 5300 kg/m^3 for Mercury (while it is only 4400 kg/m^3 for the Earth). The radius of the core is 2030±37 km (Smith et al., 2012) which implies a core radius of about 0.8 of the radius of the planet. This value is large compared to the values for Venus, Earth and Mars, which are about 0.5. This is a considerable constraint on the formation of the planet which may be unusual, compared to other terrestrial bodies.

3.1.2.1 Formation scenarios

Several formation models have been proposed to explain this unusual observation, and they can be basically divided into two categories. In the first category of models, it is assumed that Mercury was formed in a similar way as other bodies in the Solar System, so that it originally consisted of chondrites with the same iron/silicate ratio as the other terrestrial planets. In these models early planet was bigger than today but than lost large part of its silicate shell through some process shortly after the formation. For example, the giant impact theory assumes that the planet collided with a planetesimal and a great deal of mantle evaporated, leaving the planet with the core as a dominant component (Benz et al., 1988). As a hypothetical territory of this giant collision is sometimes considered the area of Caloris Basin. Another possible process that may have lead to the reduction of silicate mantle is Sun-Mercury interaction in the early stages of the Solar System evolution, when silicate crust might have evaporated during enhanced energy flow from the Sun (Fegley and Cameron, 1987). On the other hand, the second category of models explains the anomalous composition as a result of anomalous formation which was different from other planets from the beginning. E.g. the model of equilibrium condensation of nebular material is based on the fact that the condensation temperature of iron is slightly higher than for magnesium silicates (Lewis, 1973). Weidenschilling (1978) hypothesised that iron and silicate particles could have been aerodynamically sorted in the early solar nebula before accretion.

Recent measurements performed by MESSENGER GRS revealed relatively high surface ratios of K/Th and K/U (Peplowski et al., 2011, 2012) which suggests that Mercury is a volatile-rich planet. The volatile depletion of a planet is assumed to be correlated to high temperature during the formation process. The volatile-rich Mercury seems to be inconsistent with formation scenarios requiring extreme heating in the early stages of the planet evolution like vaporization, condensation and probably also giant impact model (as it is associated with widespread melting and vaporization). However, McCubbin et al. (2012) pointed out that Mercury is in many ways an end-member planet and that knowledge of geochemistry of other terrestrial planets may not be adequate to make inferences about Mercury and argued that it is still uncertain if the Mercury's mantle is volatile-rich. Moreover Stewart et al. (2013) showed that at least the giant impact theory can be viable even under consideration of volatile-rich planet. Thus the formation scenario of the planet remains uncertain.

3.1.2.2 Magnetic field

Mariner 10 discovered that Mercury has an internal magnetic field. Later MESSENGER data provided more accurate measurements. The magnetic field has a dipolar character, the axis is tilted by less than 3° with the respect to the rotational axis, the intensity is 300 nT (Hiremath, 2012) and the field is highly axisymmetric (Anderson et al., 2011). The existence of an internal field together with the observation that the mantle is decoupled from the core which is at least partially molten (Margot et al., 2007) suggest the dynamo origin of the magnetic field, although other possibilities of the field generation, like remnant crustal field (Aharonson et al., 2004), cannot be completely ruled out. Model calculations imply that thermally driven dynamo for Mercury is unlikely. Thus, it is accepted that the existence of magnetic field suggests a growing inner core (Breuer et al., 2008). Since a pure iron core could not have remained molten due to the cooling of the planet since its origin, a small amount of sulphur is often introduced to depress the freezing temperature of the core alloy (Schubert et al., 1988). However, explaining surprisingly weak (in comparison with the Earth) Mercury's field with an Earth-like dynamo remains challenging .

3.1.2.3 Thickness of the mantle and crust

Density of the mantle is 3650±225 kg/m^3 (Smith et al., 2012) which is large compared to other terrestrial bodies. This is surprising because, based on measurements, the average surface abundance of iron is only 4% (Nittler et al., 2011). Volcanic rock abundances suggest that Mercury's silicate mantle iron content is also low, thus some deeper reservoir of dense material is needed to explain high average density of the mantle. It has been hypothesised that there may be a solid layer of FeS on the top of the Mercury's core (Smith et al., 2012). The radius of the core is 2030±37 km (Smith et al., 2012) which yields only 400 km thick mantle. Moreover, if the FeS layer is present it would further reduce the thickness of the silicate shell to about 300 km. On the other hand, the mantle thickness of 400 km was reported to be the most likely value by Tosi et al. (2013) who performed several numerical simulations with varying parameters and identified successful models that satisfied constraints from observations (e.g. presence of volcanic activity, high-melt fractions, net global contracion of 3–4 km at maximum).

Different methods were used to estimate the crustal thickness. Based on the faulting depth of lobate scarps (Nimmo and Watters, 2004), gravity and topography measurements (Smith et al., 2012; Padovan et al., 2015) and models of mantle thermal evolution (Grott et al., 2011; Tosi et al., 2013) it was estimated to 10–50 km.

3.1.2.4 Gravitational and topography data

MESSENGER radio science observations provided data for gravity field analysis (Smith et al., 2012). Spherical harmonic coefficients of the geoid are available at `http://pds-geosciences.wustl.edu/missions/messenger/rs.htm` up to degree 50. MESSENGER laser altimetry provides data for topography. Harmonic coefficients (up to degree 120) for the shape of Mercury are also available at `http://pds-geosciences.wustl.edu/missions/messenger/rs.htm`. Due to MESSENGER eccentric orbit and high northern periapsis, the northern hemisphere have considerably higher resolution (Zuber et al., 2012). For geoid and topography see Fig. 3.1 and 3.2 and for their spectra Fig. 3.3.

3.1.2.5 Mantle convection

It is usually assumed that mantle convection was operating at Mercury at least in the early stages of its evolution but an unanswered question is whether it persists until present. Several papers addressed this question. Redmond and King (2007) showed that weak convection can persist on Mercury with initial Ra of $6{\cdot}10^4$ (Newtonian rheology) or $8{\cdot}10^4$ (non-Newtonian rheology) without internal heating. King (2008) attempted to explain lobate scarps as a result of convective stresses. He found that for all models convection planform was characterised by long sheet upwellings. The distribution of resulting surface stresses was in

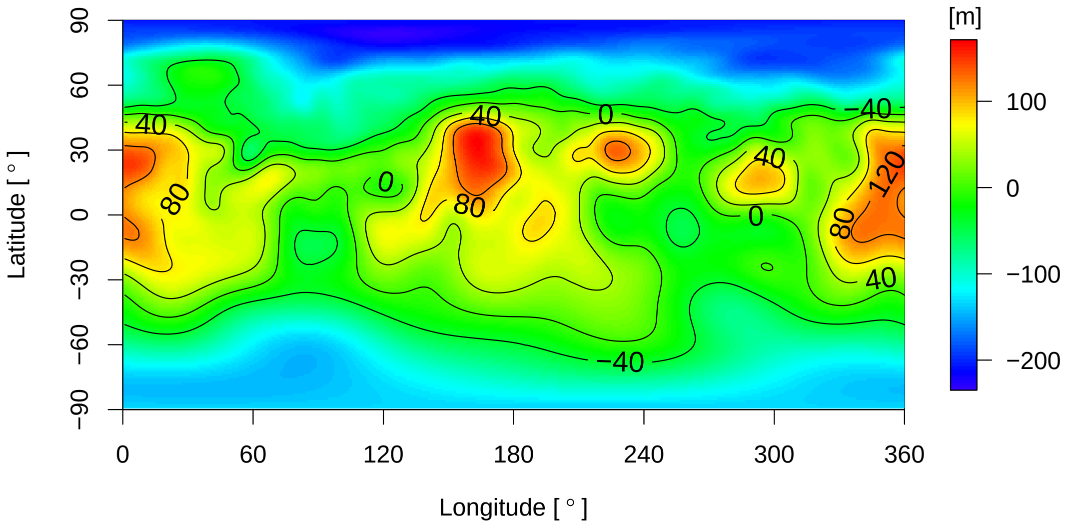

Figure 3.1: Geoid for degrees 2–50

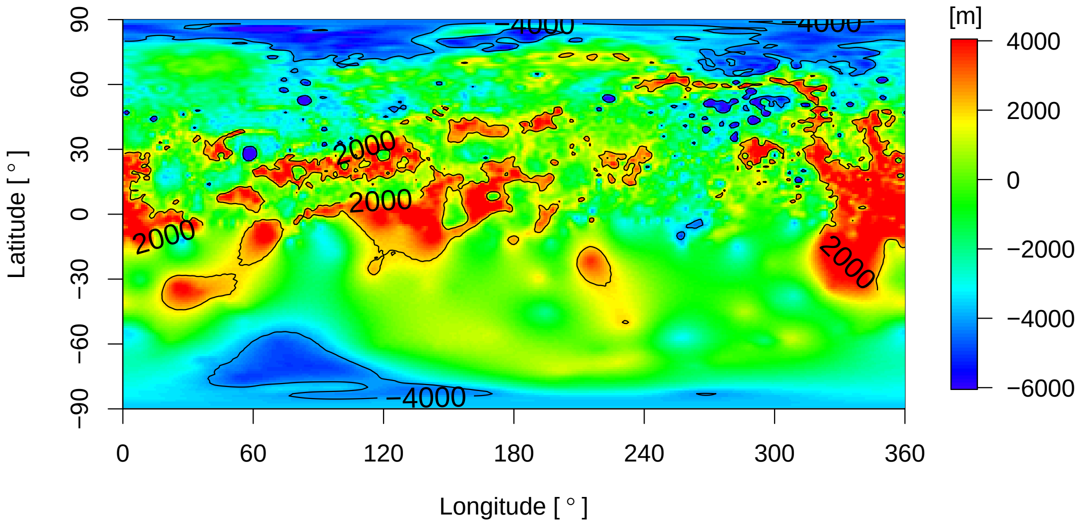

Figure 3.2: Topography for degrees 0–120.

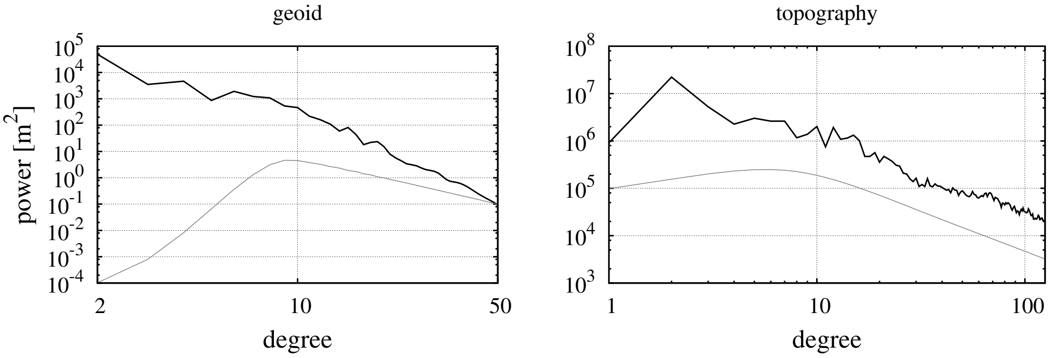

Figure 3.3: Spectra of the geoid (left) and topography (right) plotted in log-log scale. Grey line shows error spectrum.

agreement with the observed distribution of lobate scarps, thus this pattern can be a record of past mantle convection.

From mantle convection point of view, one of the most important MESSENGER findings is that the mantle is only 400 km thick (or even thinner). This is considerably lower than "pre-MESSENGER" estimate of 600 km. The thickness is one third thinner than previously thought. Keeping other parameters fixed, this results in approximately 3 times lower Rayleigh number and thus the results of previous models should be revisited under new MESSENGER constraints. Grott et al. (2011) performed calculations in several 1D thermo-chemical evolution models. All considered cases convect up to the present and convecting layer was 100–350 km thick. To identify models compatible with observations they defined the criteria of crustal thickness (larger than 10 km) and global contraction. Admissible models were characterised by viscosity greater than 10^{20} Pa s (global contraction not more than 3 km) or 10^{21} Pa s (global contraction 2 km at maximum).

Michel et al. (2013) performed spherical axisymmetric simulations. They varied several parameters like internal heat production (10–90% of the surface value), core radii (1800–2100 km), surface temperature boundary condition (constant or laterally varied) or mechanic boundary condition at the CMB (free-slip vs. no-slip). They found that for the mantle thickness larger than 400 km, mantle convection endures through the whole planet history. For thickness 366 km, the convection sustains until the present day only in some models (with CMB temperatures around 1700–1800 K) and for lower mantle thickness the duration of convection is limited to the early evolution of only 1–2 Ga. Higher internal heating rate ($> 30\%$) leads to a more vigorous and longer convection persistence. Extreme value of 90% internal heating leads to very warm mantle with pervasive melting. In some models, the final temperature at the base of the mantle was below the FeS solidus, thus allowing existence of an iron sulphide layer.

Tosi et al. (2013) ran a large set of Monte-Carlo 1D parametrized simulations complemented with 2D and 3D calculations with varying mantle parameters. They found a subset of admissible models that obey the criteria of less than 5 km global contraction, magmatic activity extending after the late heavy bombardment and production of at least 5 km thick crust. Successful models were characterised by mantle thickness of 400–500 km, crustal thickness of 80 km at maximum (but 20 km or less for majority of models) and crustal enrichment factors of radiogenic elements between 2.5 and 3.5, so the bulk silicate would be similar to other terrestrial planets: 35–62 ppb for Th, 20–36 ppb for U and 290–515 ppm for K. In most models the convective heat transfer ceased after 3–4 Ga.

3.2 Geoid and topography from mantle convection models

Taking into account above discussed evidence, currently operational mantle convection on Mercury can be neither confirmed nor completely rejected. Here we will assume that Mercurian mantle is convecting and we will test the hypothesis that its topography and geoid undulations are dynamically supported. We perform a similar analysis as in the previous chapter for Venus. We will assume three viscosity models with temperature dependent viscosity and address the question whether we can identify some characteristics of the modelled geoid and topography spectra (amplitude or slope) that would be consistent with observed data and thus allow a dynamic contribution.

3.2.1 Models

We use both 2D axisymmetric and 3D spherical models as described in paragraph 1.2 with parameters given in Table 3.1. Viscosity in our models follows the formula:

$$\eta(T) = \eta_0 \exp\left[-\ln c \, \frac{T - T_0}{T_{cmb} - T_{top}}\right], \tag{3.1}$$

where η_0 is constant and it represents the mean mantle viscosity value, $T_0 = \frac{T_{cmb}+T_{top}}{2}$ represents mean temperature and corresponds to η_0. Non-dimensional parameter c controls temperature-dependent viscosity variations. We have two

Table 3.1: Model parameters

Parameter	Symbol	Value	Units
radius of Mercury [a]	r_{top}	2440	km
mantle thickness [b]	r_{cmb}	400	km
gravity acceleration [c]	g	3.7	m s^{-2}
reference density [b]	ρ_0	3500	kg m^{-3}
coefficient of thermal expansion	α	$2 \cdot 10^{-5}$	K^{-1}
specific heat at constant pressure	c_p	1200	J kg^{-1} K^{-1}
thermal diffusivity	κ	$9.5 \cdot 10^{-7}$	m^2s^{-1}
reference viscosity [c]	η_0	10^{21}	Pa s
density at the surface [d]	$\Delta\rho_{top}$	2700	kg m^{-3}
density at CMB [d]	$\Delta\rho_{cmb}$	7300	kg m^{-3}
temperature at the surface [c]	T_{top}	440	K
temperature at the CMB	T_{cmb}	1800	K
gravitational constant	G	$6.67{\cdot}10^{-11}$	N m^2 kg $^{-2}$
rate of internal heating [b]	Q_v	$5.3 \cdot 10^{-12}$	W kg^{-1}

[a] Zuber et al. (2012)
[b] Tosi et al. (2013)
[c] Grott et al. (2011)
[d] Rivoldini and van Hoolst (2013)

models with constant viscosity $c = 1$: model 3DLV0 (3D model), and model 2DLV0 (2D model), and two models with temperature-dependent viscosity: 2DLV2 (variations of viscosity by 2 orders of magnitude, $c = 100$) and 2DLV4 (4 orders of magnitude, $c = 10000$). Phase transitions are not expected to be present in the mantle due to the small pressures (8 GPa at the CMB) (van Hoolst et al., 2007). The distribution of heat-producing elements between the crust and the mantle is not known, hence, the surface estimates (Peplowski et al., 2011) could be taken as the maximum estimate. Here we used internal heating rate that represents 30% of the surface value (Michel et al., 2013). Surface temperature of Mercury is both time and spatially variable (90–725 K (Strom, 1997)). Because it was shown (Michel et al., 2013) that the surface temperature condition influences the thermal evolution and the mantle regime only slightly, we assume the constant value of 440 K. The value of 1800 K for CMB temperature corresponds to case without FeS layer. Considering reference viscosity, Rayleigh number in our models is $2 \cdot 10^4$. An initial temperature distribution for models with radially dependent viscosity was obtained from conductive solution with perturbations. Models with temperature dependent viscosity were started from final time instant of model without temperature dependent viscosity.

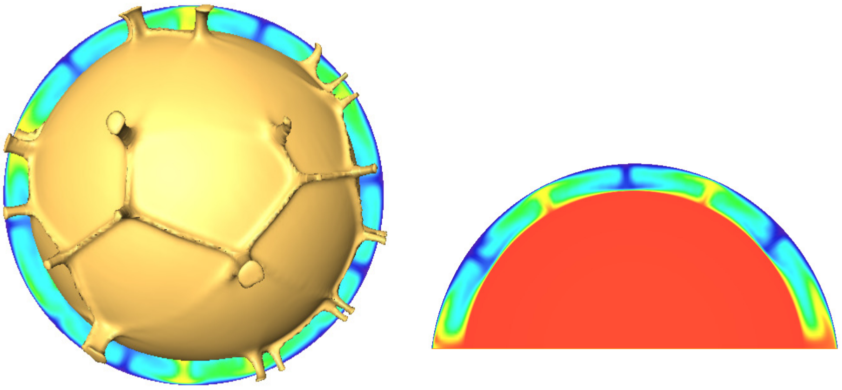

(a) 3DLV0 **(b)** 2DLV0

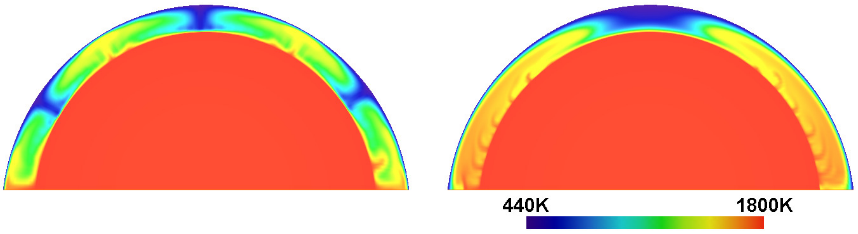

(c) 2DLV2 **(d)** 2DLV4

Figure 3.4: Temperature distribution in all models. Isosurface shown in 3D model marks 1550 K isotherm.

3.2.2 Results

The temperature distribution for all models is plotted in Fig. 3.4. 3D temperature field is characterised by several thin plumes, their distribution is not symmetric. In the 2D cases, the models without lateral variations and with lateral variations of 2 orders of viscosity result in a very similar flow pattern characterised by four thin upwellings symmetrically distributed in the mantle. In case of model 2DLV2 with lateral variations by 2 orders of magnitude, we can see that upwellings are thinner and moreover, additional small upwellings start to develop besides the main four plumes. Stronger lateral variations lead to markedly different convection pattern. It is characterised by numerous vigorous upwellings clustered in two regions at northern and southern hemisphere. Fig. 3.5 shows the radial profiles of horizontally averaged temperature and viscosity for all models. Corresponding 2D and 3D models without lateral variations (2DLV0 and 3DLV0) are characterised by almost identical geotherms. Including temperature variations of viscosity in 2D models results into warmer mantle (c.f. Fig. 3.4).

Spectra of the geoid and topography for the 3D model are plotted in Fig. 3.6 (blue line) in comparison with observed data (black line) and 2D models without

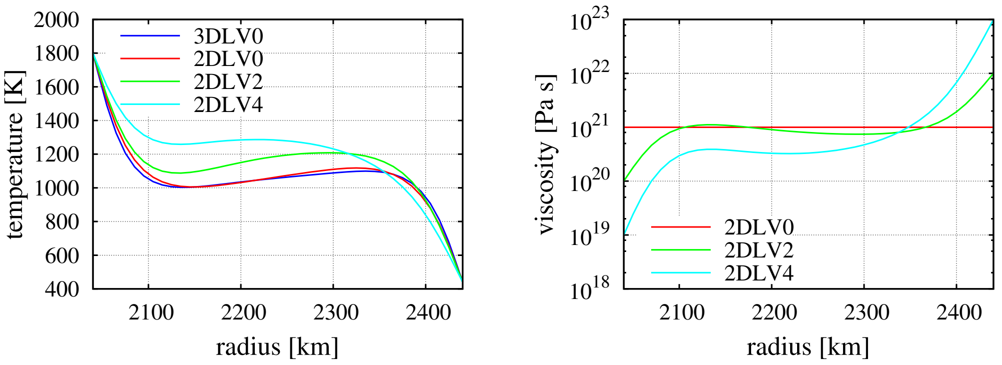

Figure 3.5: Left: radial profiles of horizontally averaged temperature. Right: horizontally averaged viscosity.

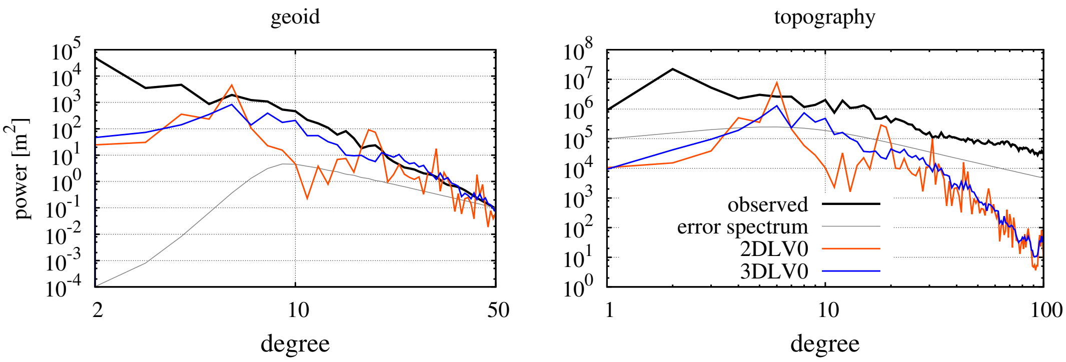

Figure 3.6: Comparison of spectra for 3D and 2D model with constant viscosity, plotted in log-log scale.

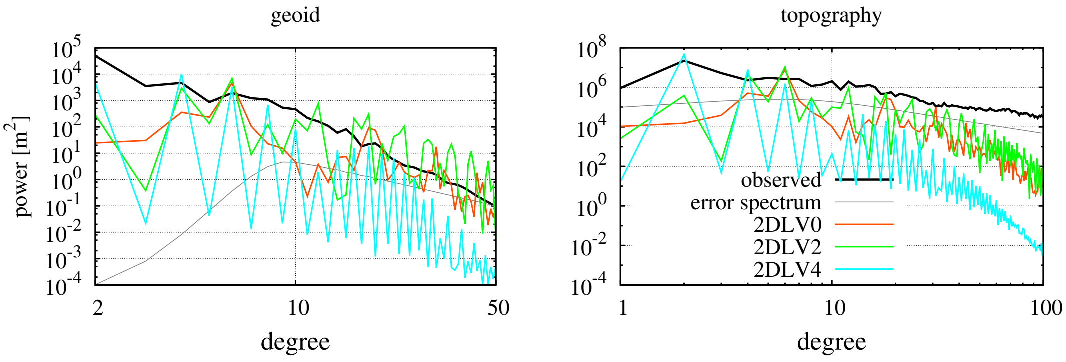

Figure 3.7: Spectra of geoid (left) and topography (right) for 2D models plotted in log-log scale.

lateral variations (red line). 3D spectra do not change considerably during the time evolution, thus we plot the last snapshot. Let us look at the geoid first. For lower degrees (2–4), modelled spectra are highly underestimated by several orders of magnitude. For degrees 5–18 the slope agrees with the observed data quite well although the amplitude is still somewhat underestimated. For degrees 20–50 both slope and amplitude agree with the observed spectra very well. On the other hand, looking at the topography, the fit is generally poor—neither amplitude nor slope of the spectra fits the observed data. Moreover, the modelled spectra are lower then uncertainties of measurements.

Now, let us look at the 2D model with constant viscosity. Similarly to the previously discussed results for Venus, in the axisymmetric case, spectra are varying with time. Therefore, the spectra averaged over the last 500 mil. yr of evolution in statistically steady-state are used in subsequent figures. In Fig. 3.6 model 2DLV0 with constant viscosity (red line) is compared to the 3D case and the observed data. 2D spectra (both geoid and topography) are more oscillatory but their slope is consistent with the spectra of the 3D model except of spectral range 7–13.

The spectra for 2D models with and without lateral variations are plotted in Fig. 3.7. Introducing mild lateral variations of viscosity (model 2DLV2) does not improve the fit to observed data. Especially for topography, the modelled spectra are very similar to model 2DLV0, which corresponds to the fact that also the temperature field is very similar. The fit of geoid is even worse than for model 2DLV0. Stronger lateral variations of viscosity (2DLV4—blue line) improve fit at some harmonic degrees, however generally we can conclude, that none of the models considered here is able to fit the observed spectra satisfactory.

3.2.3 Discussion and conclusions

Our brief and simple analysis shows that although our model is able to predict reasonable power spectra of geoid for degrees $j = 5$–50, it fails to predict both the slope and amplitudes for the topography spectra. This implies that either other mechanisms than a dynamic flow are important or more complex model should be employed in such an analysis.

Recently, the first interpretations of MESSENGER topography and gravity data in terms of chemical and mechanical structure of the Mercury's interior were published. Tosi (2015) reported that observed GTR ratios at intermediate wavelengths can be well explained by isostatic compensation associated with crustal thickness. Further, he found that the degree 2 and 4 of spectra can be explained by a long-wavelength deformation of the lithosphere caused by deep thermal anomalies associated with large temperature variations experienced by Mercury's surface.

James et al. (2015) explored the mechanisms of the support of surface topography by means of admittances and correlations of topography and gravity. They reported that long-wavelength (degree $j < 15$) topography is supported by a combination of crustal thickness variations and deep mass anomalies which may be similar in amplitude up to degree $j = 11$. The character of deep mantle anomalies is not clear but compositional stratification in the Mercury's mantle could play important role. Crustal compensation is expected to be important for all degrees less then $j = 30$.

Part II

Post-Perovskite Transition and Mantle Convection

Post-perovskite, high-pressure phase of perovskite, has been discovered about a decade ago in the D″ layer of the lowermost mantle. Here we discuss some implications this phase may have to the style of mantle convection and secular cooling of the Earth.

D″ layer

The D″ layer is complex and possibly the least understood part of the Earth mantle. It was named by Keith Bullen who (in 1942) labeled the Earth layers with letters in alphabetical order ('A'–'G'), so that 'D' denoted the lower mantle. In 1950, Bullen found that the lower mantle is not a homogeneous layer, but instead it consists of two layers. The upper one was renamed to D′, and the lowest 200 km of the mantle received the name D″.

Today, we consider the D″ layer to be the hot, basal thermal boundary layer of the convecting mantle. From the seismological point of view, it is known for its anomalous characteristics compared to the rest of the lower mantle. In some regions of the D″ layer, a discontinuity of the shear wave velocity (v_s) is observed on its top: an increase of v_s reaches 2.5–3.0% (Lay, 2007). A significant polarization anisotropy is observed within the layer—horizontally polarised seismic velocity v_s^h is 0.5–1.5% higher than the vertically polarised v_s^v (Lay, 2007). Seismic models also show anticorrelation between shear and bulk sound velocities.

The lower mantle material consists predominantly of (Mg,Fe,Al)SiO_3 with perovskite (PV) structure ($\sim$ 79%), calcium silicate perovskite $CaSiO_3$ ($\sim$ 5%) and (Mg,Fe)O magnesiowüstite ($\sim$ 16%) (Wood, 2000). Considering this mineralogy it was difficult for a long time to explain the observed sesmic anomalies in the lowermost mantle (Wysession et al., 1998).

Discovery of post-perovskite phase

The discovery of a high-pressure phase of perovskite was published in 2004 by two author groups independently within two months. Murakami et al. (2004) performed x-ray diffraction measurements of $MgSiO_3$ using laser-heated diamond anvil cell (LHDAC) at pressure and temperature similar to the conditions at the lower mantle, and demonstrated that $MgSiO_3$ perovskite transforms to a new high-pressure form (post-perovskite, PPV). It has the $CaIrO_3$ structure and consists of SiO_3 layers interleaved by Mg ions. This transition occurs at pressure above 125 GPa and temperature of 2500 K. As the pressure within the D″ layer varies between 120–136 GPa, this phase transition should happen in this layer.

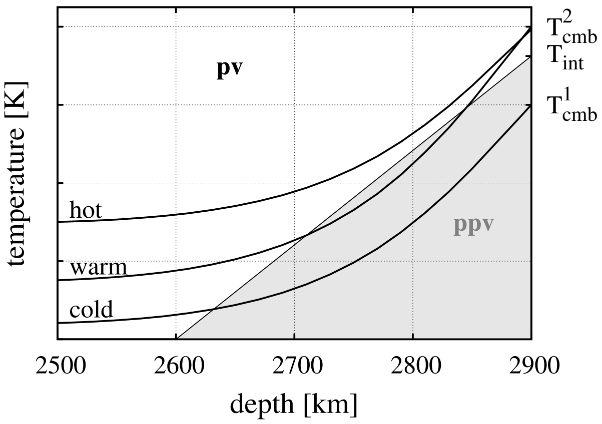

Figure 3.8: Schema of three geotherms (hot, warm and cold mantle), grey area depicts the PPV stability area.

Oganov and Ono (2004) used a joint approach of quantum-mechanical computations and LHDAC experiments. Ab initio simulations indicated that for $MgSiO_3$, the $CaIrO_3$-structured phase becomes thermodynamically more stable than perovskite within the range of lower-mantle pressures. After this theoretical prediction they found the transition experimentally. Their predicted density discontinuity due to the transition is 1.1% (1.4% for pure $MgSiO_3$), shear wave velocity (v_s) discontinuity 1.4% (1.9% for $MgSiO_3$) and a very small discontinuity for the compressional wave velocity v_p—0.3% for pure $MgSiO_3$. Obtained values of Clapeyron slope are 8.0–9.6 MPaK^{-1}.

Properties of the post-perovskite

Clapeyron slope and temperature intercept

The PV-PPV phase transition occurs at pressures and temperatures close to CMB values. However, both theoretically and experimentally determined values of Clapeyron slope and temperature intercept (T_{int}, the temperature of the PPV transition at the CMB pressure) have rather high uncertainties. Experimental studies (Hirose, 2006; Tateno et al., 2009) and ab initio calculations (Oganov and Ono, 2004; Tsuchiya et al., 2004) give values for Clapeyron slope in a broad interval from 7.5 MPaK^{-1} to 13.5 MPaK^{-1}, and the range for temperature intercept is from 3450 K to 4220 K.

The presence and the spatial distribution of the PPV phase depends on the lower mantle temperature distribution, as well as on the values of T_{int} and Clapeyron slope. As we do not know either of them precisely, different possible scenarios can occur in the lower mantle (Hernlund et al., 2005). If the mantle is cold

($T_{cmb} < T_{int}$), geotherm crosses the PPV stability field, PPV is present and forms a continuous layer with varying thickness depending on the local geotherm (Fig. 3.8, “cold” geotherm). If $T_{cmb} > T_{int}$, two scenarios are possible. If the mantle is hot, the geotherm does not cross the PPV stability area and no PPV is present (Fig. 3.8, “hot” geotherm). Considering the large Clapeyron slope and large thermal gradients expected in the thermal boundary layer, another scenario is possible: the PPV stability area is crossed by the geotherm twice. The first transition occurs at the depth where the pressure converts the PV to the PPV phase. The second transition occurs deeper, where a steep increase of the temperature converts PPV back to PV (Fig. 3.8, “warm” geotherm). If that is the case then laterally varying thermal structure in the D'' layer results in isolated lenses of PPV. It is present in cold regions where relatively cold subducted material is deposited while in hot plumes it may not be present at all. This third scenario seems to be in agreement with seismic observations which revealed a pair of inversely polarised discontinuities in the lowermost mantle (van der Hilst et al., 2007).

Density and seismic velocity

In an effort to obtain main characteristics of the newly-found phase of the mantle material, both high-pressure experiments and ab initio calculations were used. Both approaches agree in the results when the density increase associated with the transition is concerned. It was found to be only 1.0–1.5% (Irifune and Tsuchiya, 2007).

The PPV presence in the lowermost mantle could be responsible for the observed lattice preferred orientation. The distribution of the lowermost mantle seismic anisotropy as reported by Panning and Romanowicz (2006) shows the predominance of the horizontally polarized S-wave velocity over the vertically polarized one in the circum-Pacific belt. It supports the idea, that the PPV should be present only in the relatively cold areas connected to paleoslabs.

A successful explanation of some seismological observations near the core-mantle boundary provides the convincing evidence that PPV phase transition really occurs in the deep mantle. However, some features remain unexplained. E.g. observed seismic velocity jump is too large in comparison with the PPV predictions; the width of velocity transition is in the range of 50 to 70 km, while PPV is expected to coexist with PV in a wider interval. Hence, the most likely explanation of the deep mantle structure involves both PPV phase change and compositional variations (Hirose et al., 2006; Nakagawa and Tackley, 2012).

Viscosity and thermal diffusivity

The viscosity of the PPV is a subject of ongoing debate and this question was addressed by numerous studies. Several of them (based on both mineralogical experiments and first-principles calculations) indicate PPV to be by up to several orders ($3-6$) of magnitude weaker than PV (Yoshino and Yamazaki, 2007; Carrez et al., 2007; Hunt et al., 2009; Ammann et al., 2010). However, the viscosity of PPV is highly anisotropic and it has been argued (Karato, 2010) that currently available knowledge is insufficient to constraint the viscosity, and based on the calculations, it can actually be comparable or even higher to that of the PV. On the other hand, the presence of low viscosity material under the cold slabs in the lowermost mantle is consistent with the observed geoid. Long-wavelength geoid is highly sensitive to the presence of low viscosity areas located in the subducted slabs at the base of the mantle (Tosi et al., 2009). It has been shown by Čadek and Fleitout (2006) that the results of geoid inversion suggest low viscosity in the paleoslab areas in D$''$ layer, where PPV should be present thanks to relatively low temperatures.

Other PPV parameter which can be constrained by measurements is thermal diffusivity—experiments indicate at least 1.8 times higher value than that of PV (Hunt et al., 2012).

Electrical conductivity

Several studies were published on the topic of electrical conductivity of PPV. They consistently report that conductivity of PPV is up to 2 orders of magnitude higher than that of PV. E.g. Ono et al. (2006) predicted conductivity of PPV on the basis of measurements on $CaIrO_3$-structure Al_2O_3. Ohta et al. (2008) performed LHDAC measurements on $(Mg_{0.9}Fe_{0.1})SiO_3$ and reported PPV conductivity is greater then 100 S/m and does not vary greatly with temperature.

Implications of PPV for mantle dynamics

The discovery of PPV motivated many studies that investigated its effects on mantle convection. Density anomalies associated with the PPV phase change tend to enhance convective vigour and increase the number of plumes (Nakagawa and Tackley, 2004; Matyska and Yuen, 2005; Nakagawa and Tackley, 2006; Tackley et al., 2007) though this effect is not particularly strong due to a small density contrast. The presence of PPV could however enhance the effects of other parameters, such as strongly variable thermal conductivity (Matyska and Yuen, 2006). PPV phase transition was further found to destabilize chemically-dense material piling above the CMB and allow penetration of cold slabs into dense material (Nakagawa and Tackley, 2005), though this destabilising effect is less if the PPV transition depends on the composition, and occurs at lower pressure in chemically-dense material. However, it has been shown that the destabilizing effect of the PV-PPV transition can be overridden by introducing strongly depth-dependent thermal conductivity which in concert with depth-dependent thermal expansivity, stabilises plumes in the lower mantle for billions of years despite the presence of PV-PPV transition (Tosi et al., 2010). Finally, PPV transition was found to increase CMB heat flux (Nakagawa and Tackley, 2004, 2008).

Moderate effects of the lowermost mantle phase transition on convection may be further enhanced if we take into account different transport properties of PPV, especially its viscosity. Despite the fact that the rheology of PPV is still not sufficiently well described, there are some indications that it may be (possibly significantly) weaker than perovskite either through dislocation creep viscosity (Carrez et al., 2007) or due to a considerably lower diffusion creep viscosity (Ammann et al., 2010). Another possible mechanism that could produce PPV weaker than perovskite at the same pressure and temperature conditions could be the grain size reduction associated with the phase transition (Karato et al., 2001; Solomatov and Moresi, 2002). Rheologically weak PPV may considerably affect dynamics of cold downwelling slabs, further enhance lowermost mantle convective velocities and CMB heat flux (Čížková et al., 2010; Nakagawa and Tackley, 2011; Li et al., 2014) and increase mantle temperatures and mixing efficiency (Tosi et al. (2010); Samuel and Tosi (2012)). It also produces seismic velocity anomalies consistent with observations (van den Berg et al., 2010) and affects geoid above slabs through enhancement of flow in the lowermost mantle (Tosi et al., 2009). Furthermore, Amit and Choblet (2009) concluded that if the effect of PPV on enhancing CMB heat flux is taken into account, consistency of geodynamo models with the observations is improved.

In following chapter we will concentrate on the effects of PPV on the long-term evolution of the mantle and its secular cooling. We will be particularly interested in the influence of rheologically weak PPV that may significantly enhance the cooling process.

4. Influence of the Post-Perovskite Phase on the Thermal Evolution of the Earth[1]

In the early Earth, the mantle was probably too hot to allow for the PPV formation. During the mantle cooling, the PPV appeared at a certain moment, and may have exerted potentially strong effects on the mantle evolution by increasing the core-mantle heat flux and thus enhancing the core cooling. Some of these effects have already been discussed in terms of long-term models. The model of the mantle thermal evolution and the associated core cooling and inner-core growth of Nakagawa and Tackley (2010) included the PPV phase transition, but did not take into account the low viscosity of PPV. They report weak dependence of the system on the initial CMB temperature, and strong dependence on the chemical anomalies in the deep mantle. Dense piles accumulated at the CMB facilitate obtaining correct final inner core size and maintaining geodynamo. Weak sensitivity to initial CMB temperature was further confirmed in Nakagawa and Tackley (2012), where magmatism was identified as dominant mechanism of heat loss in early stages of the Earth evolution. Finally, Nakagawa and Tackley (2011) concentrated on the effect of weak PPV and concluded that it increases lateral extent of chemical anomalies and reduces CMB topography by weakening the slabs at the base of the mantle. As already pointed out before, it also increases CMB heat flux and should therefore potentially influence the rate of core cooling. Core cooling was however not included in their model.

Here we supplement these previous studies by investigating effects of rheologically distinct PPV on the mantle cooling in the model that includes decaying heat sources and heat extraction from the core. The core is assumed to be an isothermal heat reservoir with temperature controlled by heat flux through CMB. We simulate the long-term evolution of the mantle from a hot initial state, and we evaluate combined effects of the weak PPV and several other parameters (thermal expansivity, diffusivity, initial core temperature).

---

[1] The material contained in this chapter was submitted for publication as BENEŠOVÁ, N. and ČÍŽKOVÁ, H. Effect of post-perovskite rheology on thermal evolution of the Earth. *Physics of the Earth and Planetary Interiors*

Element	τ^i [Ga]	H(4.5 Ga)	H_0^i [W/m^3]
Uranium	4.5	$9.52 \cdot 10^{-9}$	$19.2 \cdot 10^{-9}$
Thorium	14	$8.92 \cdot 10^{-9}$	$11.2 \cdot 10^{-9}$
Potassium	1.3	$0.96 \cdot 10^{-9}$	$11.6 \cdot 10^{-9}$

Table 4.1: Values of half-lives and heating rates for internal heating model MH1.

4.1 Model description

Calculations were done in the 2D model using extended Boussinesq approximation. Table 4.2 summarises model parameters. List of all presented models is in Table 4.3.

Thermal coupling of the mantle and the core

When models of long-term secular cooling are considered CMB, temperature should not be kept constant, but should decrease as the mantle is cooling and heat is extracted from the core. Efficiency of mantle convection determines the rate of heat loss from the core. In our model the core is considered to be an isothermal heat reservoir and its temperature T_C is controlled by the total heat flux through core-mantle boundary Q_{cmb} (van den Berg et al., 2005b):

$$\frac{\mathrm{d}T_C}{\mathrm{d}t} = -\frac{Q_{cmb}(t)}{\varrho_C \, c_{pC} \, V_C'}. \tag{4.1}$$

Here ϱ_C is the density of the core, c_{pC} is the specific heat at a constant pressure of the core and V_C' is the volume of the core. The term $\varrho_C c_{pC} V_C'$ is the total heat capacity of the core. This equation is solved together with the thermal equation (1.3) and at each time step the new core temperature is evaluated and the boundary condition is updated so that $T_{cmb} = T_C$.

Internal heating

Internal heat production from radiogenic elements is an important source of energy for the mantle dynamics. Present-day internal heat production is about 20 TW (Korenaga, 2008). This value was of course larger in the early stages of the Earth's history. To be significant on Earth's age time scale, radiogenic elements need to have long enough half-life and be sufficiently abundant with enough decay energy. Four isotopes are usually considered ^{238}U, ^{235}U, ^{232}Th and ^{40}K.

We use two models of internal heating rate and its time decay. Model MH1

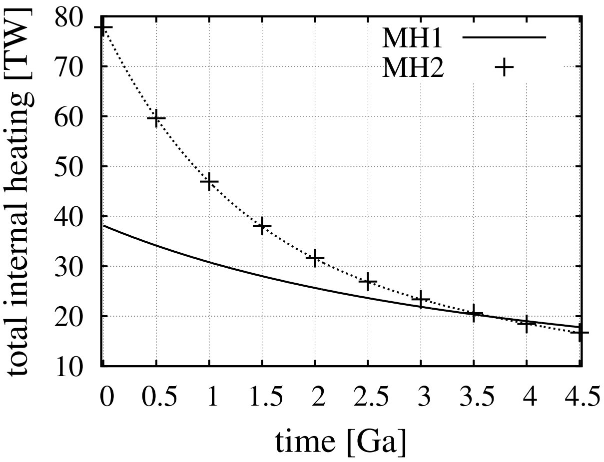

Figure 4.1: Comparison of two assumed models of internal heating. Model MH1 is based on Lowrie (2007), model MH2 is based on van Schmus (1995).

assumes equation

$$H(t) = \sum_{i=U,Th,K} H_0^i \exp\left(-\frac{t\ln 2}{\tau^i}\right), \tag{4.2}$$

where initial productions of individual radioactive elements H_0^i are calculated from their present-day values and half-lives τ^i (Lowrie, 2007), see Table 4.1. As the proportion of ^{235}U in natural uranium is about 0.71% while that of ^{238}U is 99.28%, the effect of ^{235}U is omitted here. It may be potentially more important in the early Earth due to its relatively short half-life (0.704 Ga) but still its contribution to the total internal heating budget was about 5 TW and rapidly decreasing.

The second model of internal heating MH2 follows relation

$$H(t) = \frac{1}{M}\Big((10.26t + 51.16)\exp(-t) - 2.49t + 26.78\Big), \tag{4.3}$$

where $M = 3.63216 \cdot 10^{24}$ kg is the mass of the Earth. This formula was interpolated from van Schmus (1995). Time evolution of the internal heating rate in both models is illustrated in Fig. 4.1.

Viscosity

Viscosity depends on pressure and temperature following formula

$$\eta(r,T) = \Delta\eta\,\eta_0 \exp\left[\ln a\,\frac{r_{top}-r}{r_{top}-r_{cmb}} - \ln c\,\frac{T-T_{top}}{T_{cmb}-T_{top}}\right]. \tag{4.4}$$

An arbitrarily chosen parameter η_0 controls Rayleigh number. Parameter a controls depth-dependence of viscosity. We use $a = 100$ that results in two orders of magnitude viscosity increase with depth while $c = 150$ determines temperature variations of viscosity of the order of 150. As this temperature dependence is relatively weak we apply additional viscosity contrast $\Delta\eta$ which is depth dependent. In uppermost 100 km of the model $\Delta\eta = 10$ to produce stronger lithosphere. In the rest of the mantle $\Delta\eta = 1$. Additional viscosity variations are introduced due to phase transitions (see below).

Phase transitions

All models include the spinel-perovskite endothermic phase transition which occurs at 660 km depth. In some models, PV to PPV exothermic transition is prescribed with moderate Clapeyron slope of 10 MPa/K and density contrast of 1 % (Irifune and Tsuchiya, 2007). Clapeyron slope and temperature intercept are both uncertain, as discussed above, and their values were chosen to lie within the range given by experimental and theoretical studies. Transition width of 660-km phase transition is 40 km, while for the PPV transition we assume relatively broad transition width of 200 km to facilitate numerical stability of the model runs. Such a wide transition is however supported by in situ experiments of Catalli et al. (2009) and Andrault et al. (2010). The PPV phase is either by one or two orders of magnitude weaker than the PV at the same pressure and temperature conditions. In these model cases viscosity according to formula (4.4) is multiplied by a factor $\Delta\eta_{PPV} = 0.1$ or 0.01 within the PPV stability area. Phase transition at 660-km depth is associated with a viscosity increase by factor $\Delta\eta_{660} = 10$.

Thermal conductivity and thermal expansivity

Thermal conductivity is either constant $k_0 = 5.9$ W m^{-1} K^{-1} or radially-dependent. The model of radially dependent $k(r)$ based on pressure and temperature dependent model of Hofmeister (1999) is taken from van den Berg et al. (2005b). The surface value of radially dependent conductivity is $k_{top} = 4.8$ W m^{-1} K^{-1}.

Thermal expansivity is either constant α_0 or radially stratified after Matyska et al. (2011):

$$\begin{aligned} \tfrac{\alpha}{\alpha_0} &= (1 + 0.78z)^{-5} && \text{if } 0 \le z \le 0.23, \\ \tfrac{\alpha}{\alpha_0} &= 0.44(1 + 0.35(z - 0.23))^{-7} && \text{if } 0.23 \le z \le 1. \end{aligned} \tag{4.5}$$

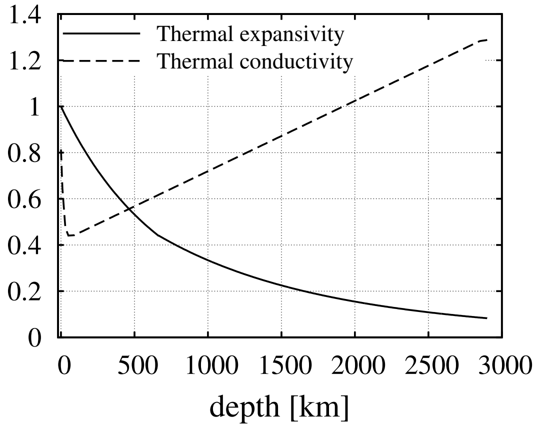

Figure 4.2: Dimensionless profiles of thermal conductivity and expansivity

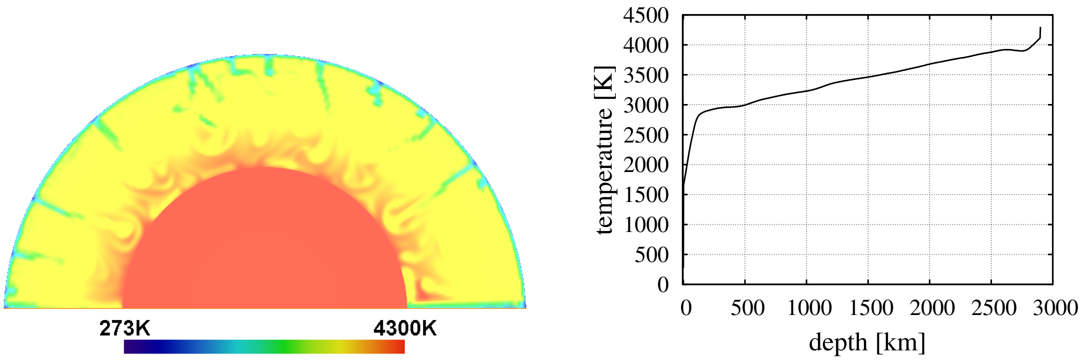

Figure 4.3: Initial temperature distribution (left) and its horizontally averaged geotherm (right).

where z is non-dimensional depth (Fig. 4.2).

Initial condition

Initial distribution of temperature should represent overheated early Earth. Following van den Berg et al. (2005b) we obtained this initial temperature from a statistical steady-state solution of a model run with extremely high internal heating rate (approximately ten times higher then present day value: $\sim 4.7 \cdot 10^{-11}$ W/kg) with thermal bottom boundary condition constant in time $T_{cmb} = 4300$ K. Rayleigh number of this initial run was $Ra = 10^7$ and viscosity was constant. All other parameters were the same as in regular model runs (see Table 4.2). Initial temperature distribution together with its geotherm is plotted in Fig. 4.3.

Parameter	Symbol	Value	Units
radius of the Earth	r_{top}	6371	km
core radius	r_{cmb}	3471	km
gravity acceleration	g	9.87	m s^{-2}
reference density	ρ_0	4000	kg m^{-3}
specific heat at constant pressure	c_p	1250	J kg^{-1} K^{-1}
thermal expansivity	α_0	$2.5 \cdot 10^{-5}$	K^{-1}
thermal conductivity	k_0	5.9	W m^{-1} K^{-1}
density of the core	ϱ_C	12500	kg m^{-3}
specific heat of the core	c_{pC}	500	J kg^{-1} K^{-1}
temperature on the surface	T_{top}	273	K
Clapeyron slope (660 km)	γ_{660}	-2.5	MPa K^{-1}
density jump (660km)	$\Delta\rho_{660}$	342	kg m^{-3}
temperature of 660 km phase tr.	T_{660}	1800	K
width of the 660 km transition	d_{ph}^{660}	40	km
relative viscosity change	$\Delta\eta_{660}$	10	
Clapeyron slope of PPV phase transition	γ_{PPV}	10	MPa K^{-1}
density jump at PPV phase transition	$\Delta\rho_{PPV}$	40	kg m^{-3}
temperature intercept	T_{int}	3800	K
width of PPV phase transition	d_{ph}^{PPV}	200	km
relative viscosity change	$\Delta\eta_{PPV}$	0, 0.1, 0.01	

Table 4.2: Model parameters

4.1.1 Model characteristics

In order to be able to evaluate the PPV influence on the thermal history in different models we have chosen a set of characteristics which we will observe in time evolution. Those characteristics are: snapshots of temperature and viscosity fields at five stages of evolution (0.5, 1.5, 2.5, 3.5 and 4.5 Ga); average geotherm and radial profile of viscosity at the end of the calculation ($t = 4.5$ Ga) both in comparison with initial state; time evolution of: volume average temperature; core-mantle temperature, heat fluxes on both boundaries in comparison with internal heating, Rayleigh number and thickness of PPV layer (it is defined as the mean thickness of the PPV layer assuming it is distributed as continuous layer above CMB).

4.2 Results

4.2.1 Models B-10^6

First let us discuss the results of models with lower initial $Ra = 10^6$ with constant expansivity and diffusivity. We will consider the model B0-10^6 (without PPV)

model name	PPV	$Ra^{t=0}$	H	$T_{cmb}^{t=0}$ [K]	k [W/mK]	α [K^{-1}]
B0-10^6	no	10^6	MH1	4300	5.9	$2 \cdot 10^{-5}$
B1-10^6	1					
B2-10^6	2					
B0-$10^6$4500	no			4500		
B2-$10^6$4500	2					
B0-10^6k	no			4300	$k(r)$	
B2-10^6k	2					
B0-10^6schm	no		MH2		5.9	
B2-10^6schm	2					
B0-$10^6\alpha$	no					$\alpha(r)$
B2-$10^6\alpha$	2					
B0-10^6kα	no				$k(r)$	
B2-10^6kα	2					
B0-10^6kα4500	no			4500		
B2-10^6kα4500	2					
B0-10^7	no	10^7				
B2-10^7	2					

Table 4.3: List of presented models. Column 'PPV' indicates whether there is a PPV phase transition or not—1(2) means PPV is 1(2) order(s) of magnitude weaker than perovskite. H indicates the type of internal heating. $Ra^{t=0}$ and $T_{cmb}^{t=0}$ are values at the beginning of the calculation, column k designates thermal conductivity ($k(r)$ denotes radial profile defined in the text), while $\alpha(r)$ in column α indicates radially dependent thermal expansivity.

to be a reference model. Cooling of the Earth in the reference model is shown in Fig. 4.4a, together with model B1-10^6 (PPV 1 order weaker, Fig. 4.4b) and model B2-10^6 (PPV 2 orders weaker, Fig. 4.4c). Five time snapshots of temperature and viscosity are shown. Time evolution of the corresponding characteristic quantities is plotted in Fig. 4.5. For the first c. 500 millions years, all three cases evolve similarly as no PPV is present (see Fig. 4.5, layer of PPV). After that period the cold downwellings reach the bottom of the mantle and PPV starts to appear in the models where PPV phase transition is included. First, let us look at model B0-10^6 (without PPV, Fig. 4.4a). In the second snapshot, the mantle is hot with four plumes rising from the CMB region. Some of the cold downwellings are hindered at the 660-km boundary due to the combined effects of the endothermic phase transition and a viscosity increase. Both the mantle and the core are cooling with time, tendency to layered flow is decreasing and in the final snapshot, most downwellings reach the lower mantle, though some of them are temporarily deflected at the 660-km interface. (The only exception is the polar region where the plume-slab interaction occurs. This is however an anomalous position where vertical cylindrical features are enforced by axisymmetric geometry.) The evolution of the core temperature is demonstrated in Fig. 4.5 (CMB temperature, red curve). The core cooling is ineffective in the first 0.5 Ga, mainly due to the 660-km phase transition. In the hot early mantle, this phase transition enforces layered flow and the overheated lower mantle is blanketing the core and reducing the core cooling. Both the surface and the CMB heat fluxes are decreasing (Fig. 4.5, heat flux) and very short periods of a negative heat flux may even appear when the core is temporarily warming. After this initial period, the phase transition effects are getting weaker, as the mantle is cooling and Ra decreasing. The CMB heat flux increases and the core temperature is decreasing steadily.

If PPV weaker by one order of magnitude is taken into account, we observe some changes in character of flow (Fig. 4.4b). After about 0.5 Ga of evolution, PPV appears in the coldest material above CMB. In the second snapshot (1.5 Ga) of Fig. 4.4e, reduced viscosity of PPV is visible in both massive polar downwellings. Weakening of the cold foot of the slab results in an enhanced lateral flow above the CMB, and consequently the downwellings are thinner than in the case without bottom weakening. Higher mobility of cold material in the bottom boundary layer increases the CMB heat flux (Fig.4.5, heat flux at CMB, green curve) and makes the core cooling more efficient (Fig. 4.5, CMB temperature, green curve). The resulting core temperature is thus 150 K lower than in the model without weak PPV. As a consequence also Rayleigh number is lower (Fig. 4.5, Rayleigh number). There is no significant difference in the surface heat flux.

Model B2-10^6 with even lower PPV viscosity (Figs. 4.4b and 4.4e) further enhances phenomena observed in model B1-10^6. CMB heat flux is higher and more oscillatory (Fig. 4.5, heat flux at CMB, blue curve), especially in the time intervals when massive cold downwellings arrive at the CMB. The resulting CMB temperature is thus about 30 K lower than in the case of intermediate PPV viscosity (Fig. 4.5, CMB temperature). Both models B1-10^6 and B2-10^6 end up with similar Rayleigh number, and also the amount of PPV is similar through the calculation. Consequently, the thickness of PPV layer is about 250 km (Fig. 4.5, layer of PPV).

Rheologically weak PPV reduces the core temperature, however, this effect seems to be localised in the lowermost parts of the mantle and does not strongly affect the average mantle temperature (Fig. 4.5, average temperature). This is also demonstrated in Fig. 4.6 (left panel), where the initial mantle geotherm (black curve) is plotted together with the average geotherms of final snapshots for all three models B0-10^6, B1-10^6 and B2-10^6. Geotherms only differ in the bottom 1000 km. Even these relatively small differences can affect radially averaged viscosity (right panel), and together with PPV viscosity reduction are thus responsible for a different core cooling efficiency and mobility of the lowermost mantle.

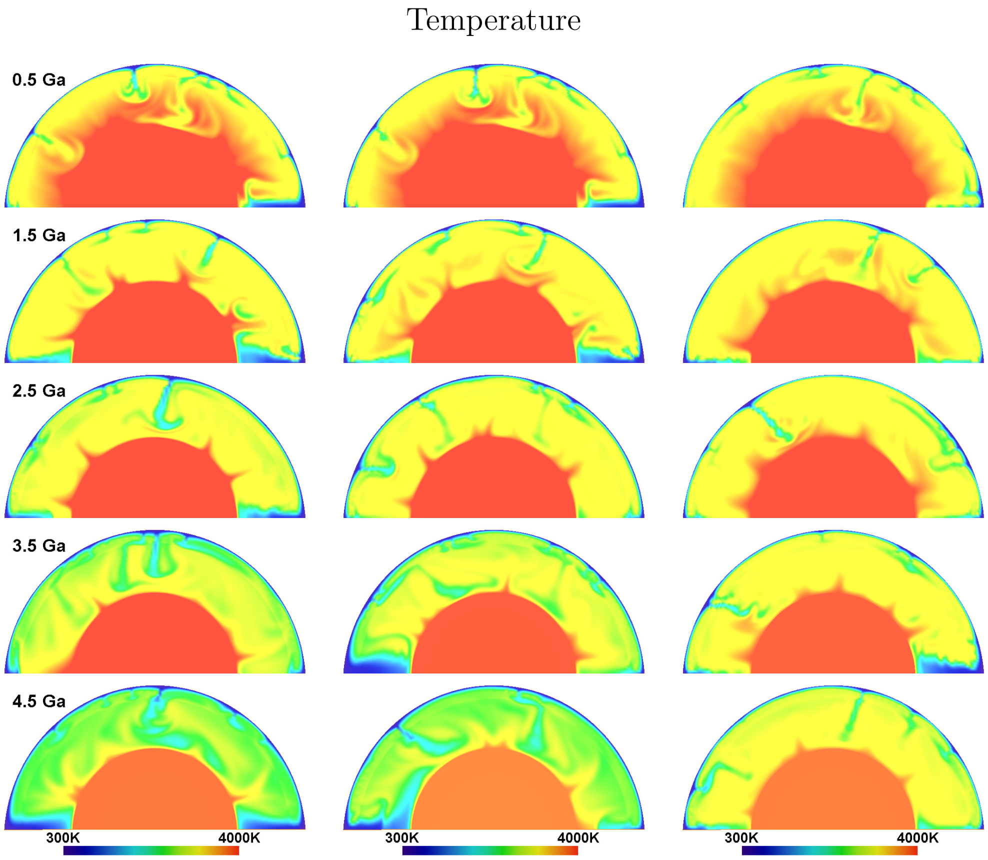
Temperature

(a) B0-$10^6$4500 **(b)** B0-10^6schm **(c)** B0-10^6k

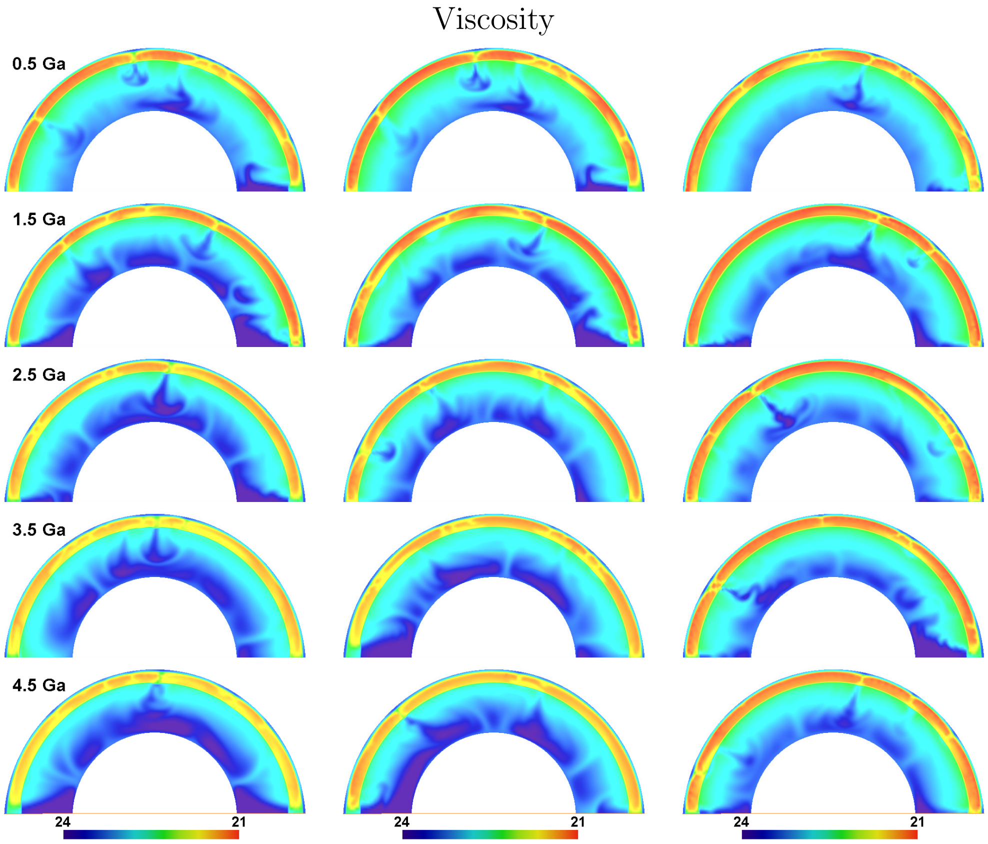
Viscosity

(d) B0-$10^6$4500 **(e)** B0-10^6schm **(f)** B0-10^6k

Figure 4.4: Models B-10^6: evolution of temperature and viscosity (in log-scale)

4.2.2 Models B-10^6P - effect of other material parameters

Except of PPV viscosity, there are apparently some other model parameters that affect the cooling efficiency. In this section we tested several parameters and their influence on the thermal evolution, namely the initial core temperature, the internal heating rate, the depth-dependent thermal conductivity, the depth-dependent thermal expansivity and the combination of these. First let us compare the effect of different parameters without PPV. Snapshots of temperature and viscosity evolution are in Fig. 4.7 and 4.8, the time evolution of different quantities is in Fig. 4.9, and radial profiles of temperature and viscosity in Fig. 4.10.

Model B0-$10^6$4500 with a higher initial CMB temperature (Fig. 4.7a, 4.7d) results in a rather similar flow pattern as the reference model B0-10^6 (Fig. 4.4a, 4.4d), though the average mantle temperature and the final CMB temperature is somewhat higher than in the reference case (Fig.4.9). The overall cooling rate is higher in the case of a higher initial CMB temperature (as a consequence of a higher CMB heat flux and also Rayleigh number). Model B0-10^6schm with a higher initial internal heating rate produces also a similar flow pattern (Fig. 4.7b, 4.7e) as the reference model, although both the average mantle and the CMB temperatures are slightly higher (about 50 K), thanks to the fact that the cooling rate in the initial 1 Ga is much less efficient than in the reference case. A much more pronounced effect on the mantle temperature is however observed in the model with depth-dependent conductivity (Fig. 4.7c, 4.7f). Here relatively low conductivity at shallow depths suppresses the heat extraction from the mantle, and results in significantly higher mantle temperatures (of about 400 K, Fig. 4.9, green curve). A warmer mantle is in turn less efficient in extracting heat from the core, and the final CMB temperature is thus by about 100 K higher than in the reference case. Finally, thermal expansivity decreasing with depth (model B0-$10^6\alpha$) results in long-wavelength lower-mantle downwellings (Fig.4.8a), and sluggish convection that is significantly less efficient in removing heat from the core. Both the average mantle temperature and the CMB temperatures are thus higher than in the reference model. We can also see that model B0-$10^6\alpha$ yields the highest surface heat flux $\sim$ 65 TW, considerably higher than the reference model ($\sim$ 40 TW).

A combination of depth-dependent expansivity and conductivity is further studied in models B0-10^6kα (initial CMB temperature 4300 K) and B0-10^6kα4500 (initial CMB temperature 4500 K). Both parameters tend to stabilize the lower-mantle circulation, and result in a relatively slow long-wavelength flow (Fig. 4.8b and 4.8c) and consequently, in significantly higher temperatures of both the man-

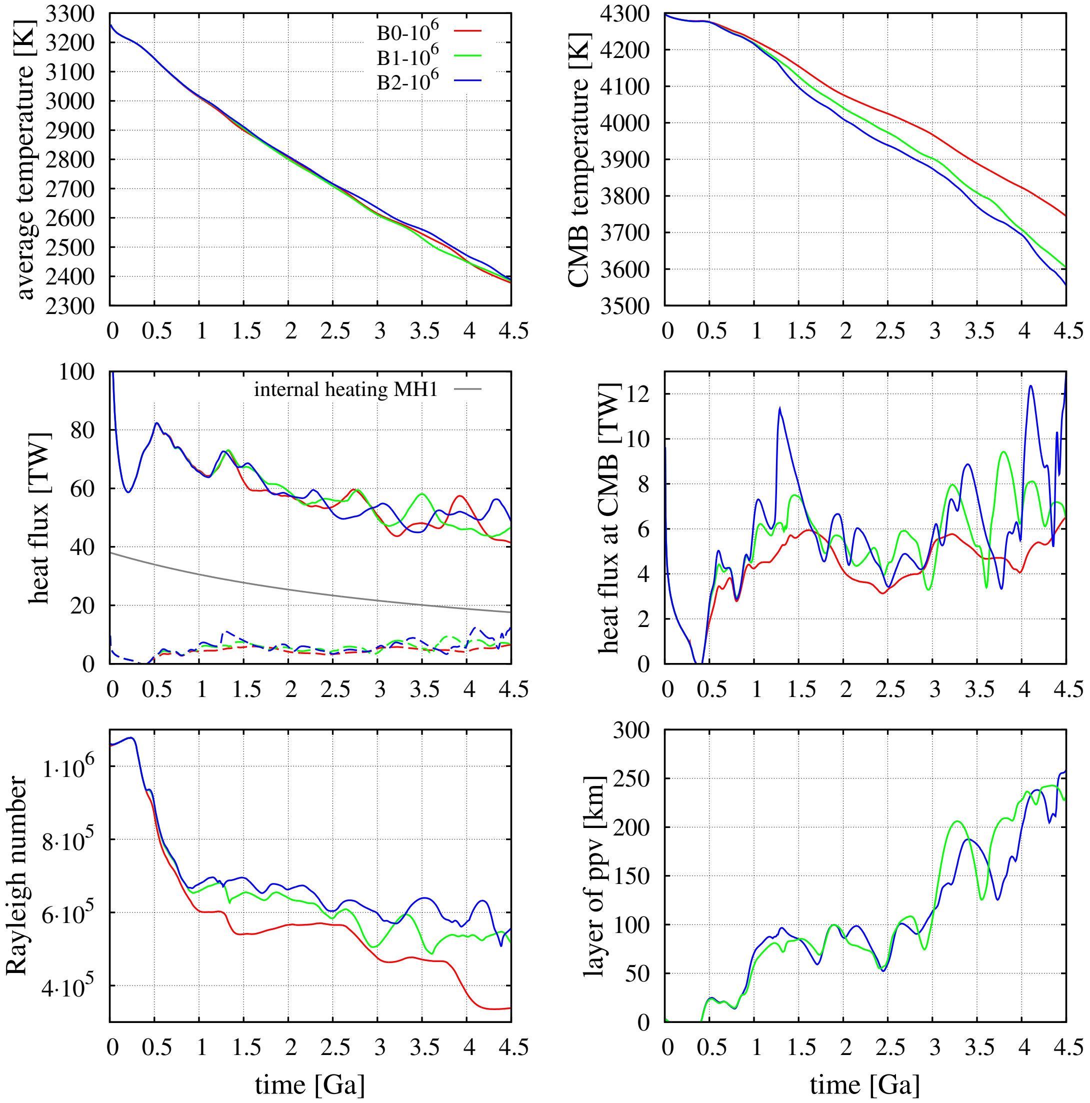

Figure 4.5: Models B-10^6: time evolution of selected quantities.

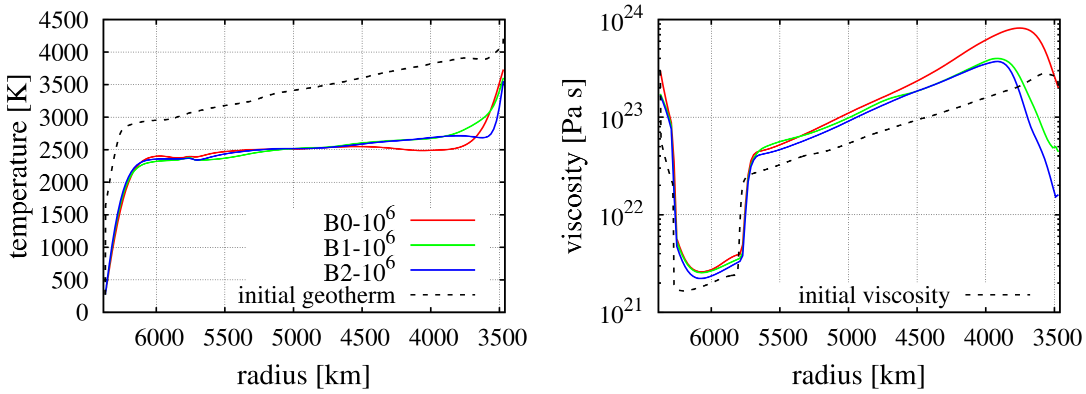

Figure 4.6: Models B-10^6: radial profiles of the horizontally averaged temperature (left) and viscosity (right) at $t = 0$ and 4.5 Ga

tle and the core. Endothermic phase transition at 660-km depth acts as a more effective barrier in these models and we observe partially layered convection that is so inefficient in removing heat from the lower mantle, that the average mantle temperature is increasing within the first 1.5 Ga of the mantle evolution. Due to a hot mantle we observe a negative CMB heat flux. Layering of the mantle can be observed also in geotherms (Fig. 4.10) in all models which include depth-dependent expansivity, where 660-km phase transition prevents the material exchange, and consequently, a thermal boundary layer is formed around this depth.

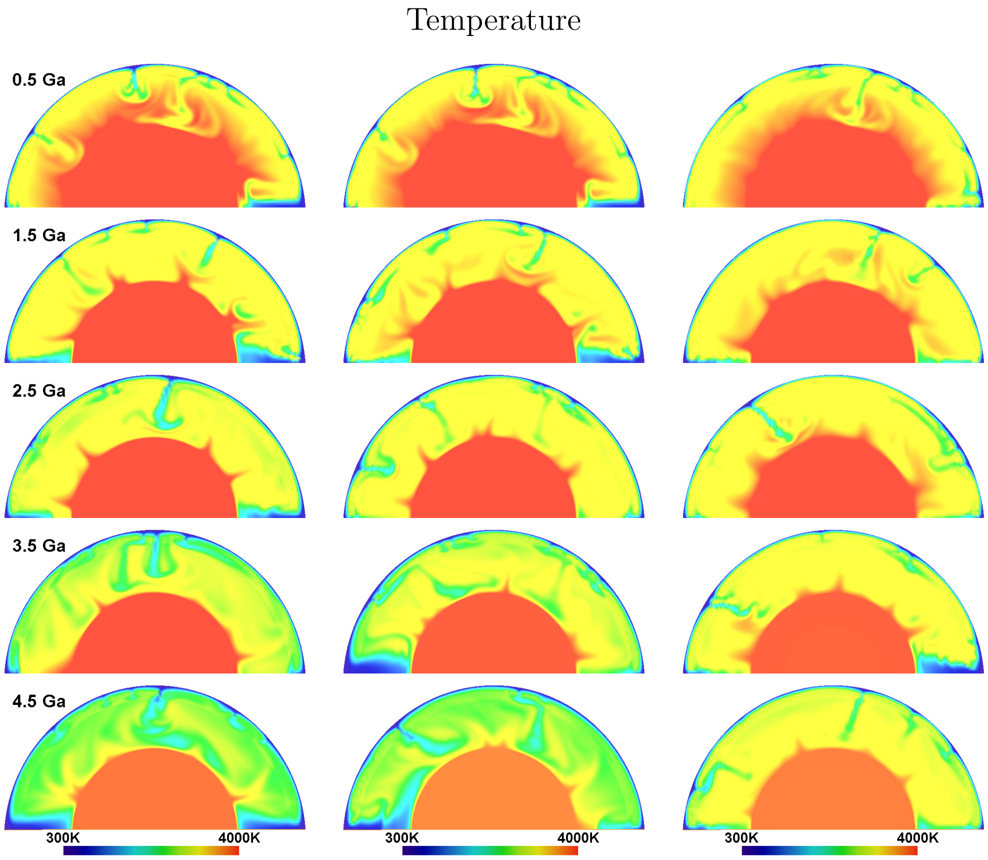

(a) B0-$10^6$4500 **(b)** B0-10^6schm **(c)** B0-10^6k

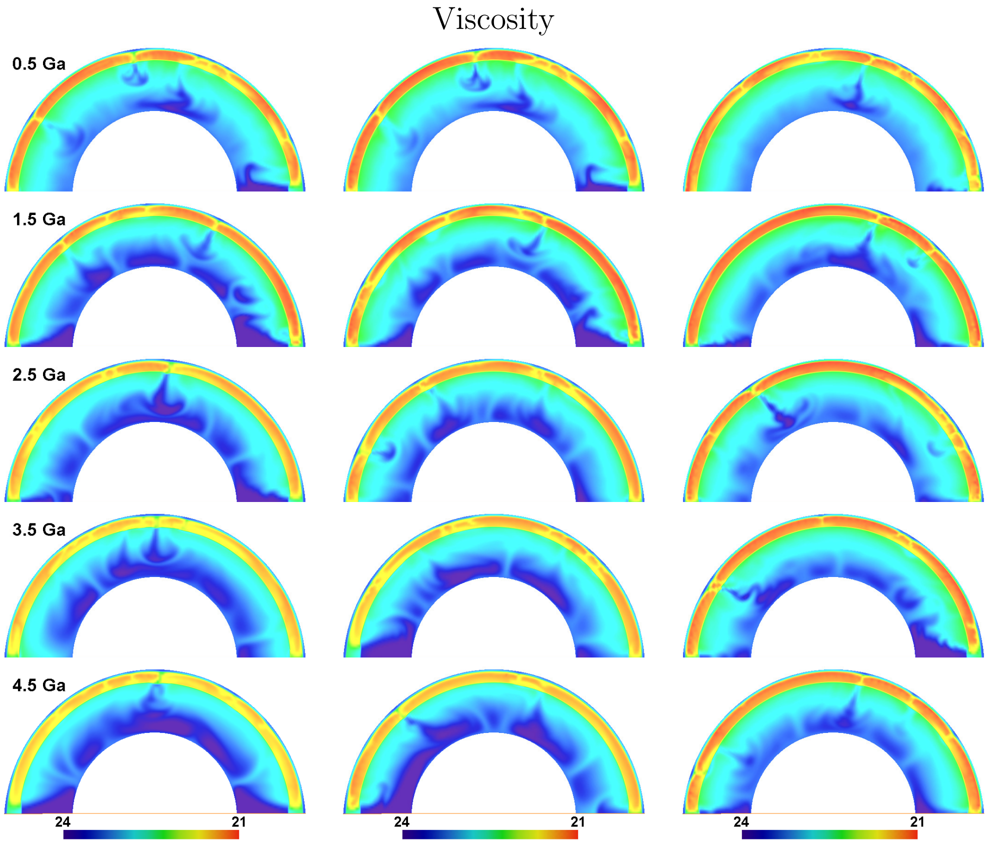

(d) B0-$10^6$4500 **(e)** B0-10^6schm **(f)** B0-10^6k

Figure 4.7: Models B-10^6P: evolution of temperature and viscosity (in log-scale)

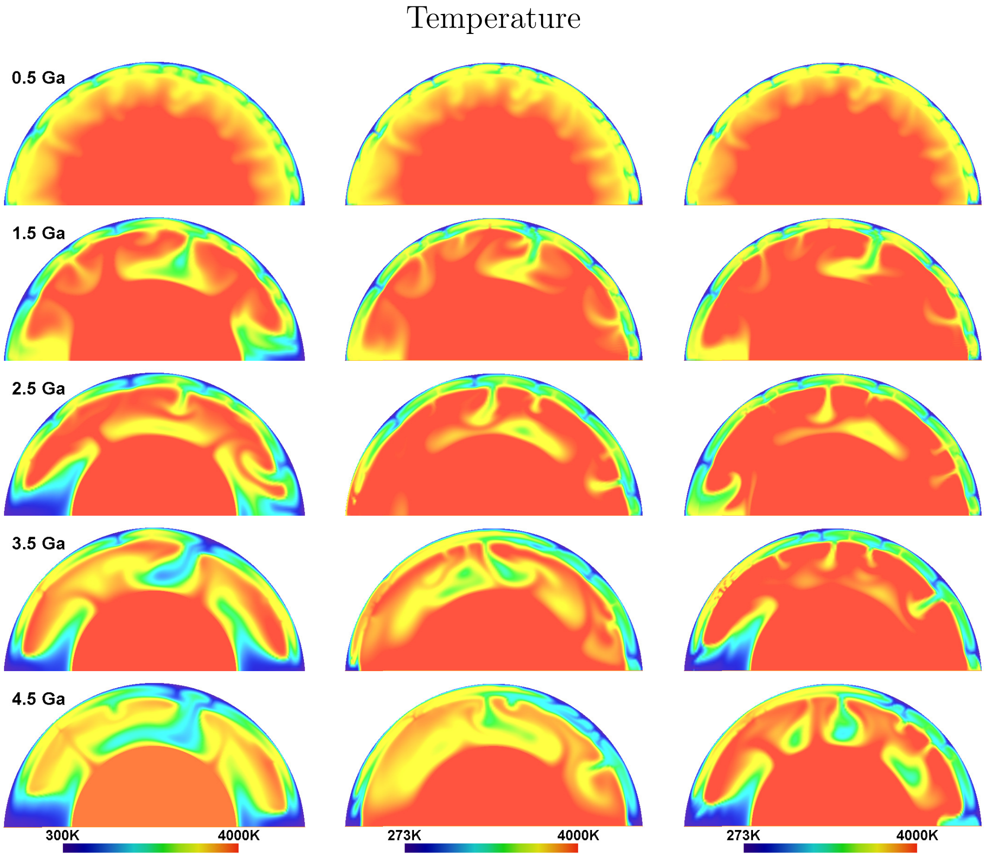

(a) B0-$10^6\alpha$ **(b)** B0-10^6kα **(c)** B0-10^6kα4500

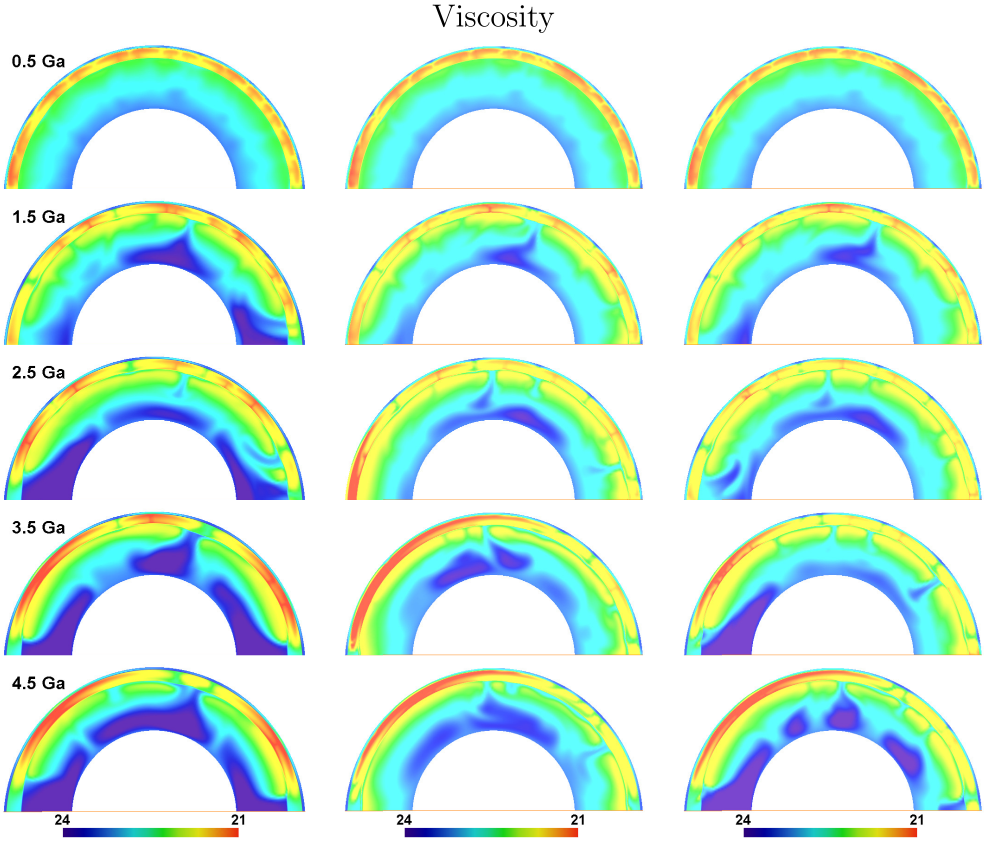

(d) B0-$10^6\alpha$ **(e)** B0-10^6kα **(f)** B0-10^6kα4500

Figure 4.8: Models B0-10^6P: evolution of temperature and viscosity (in log-scale)

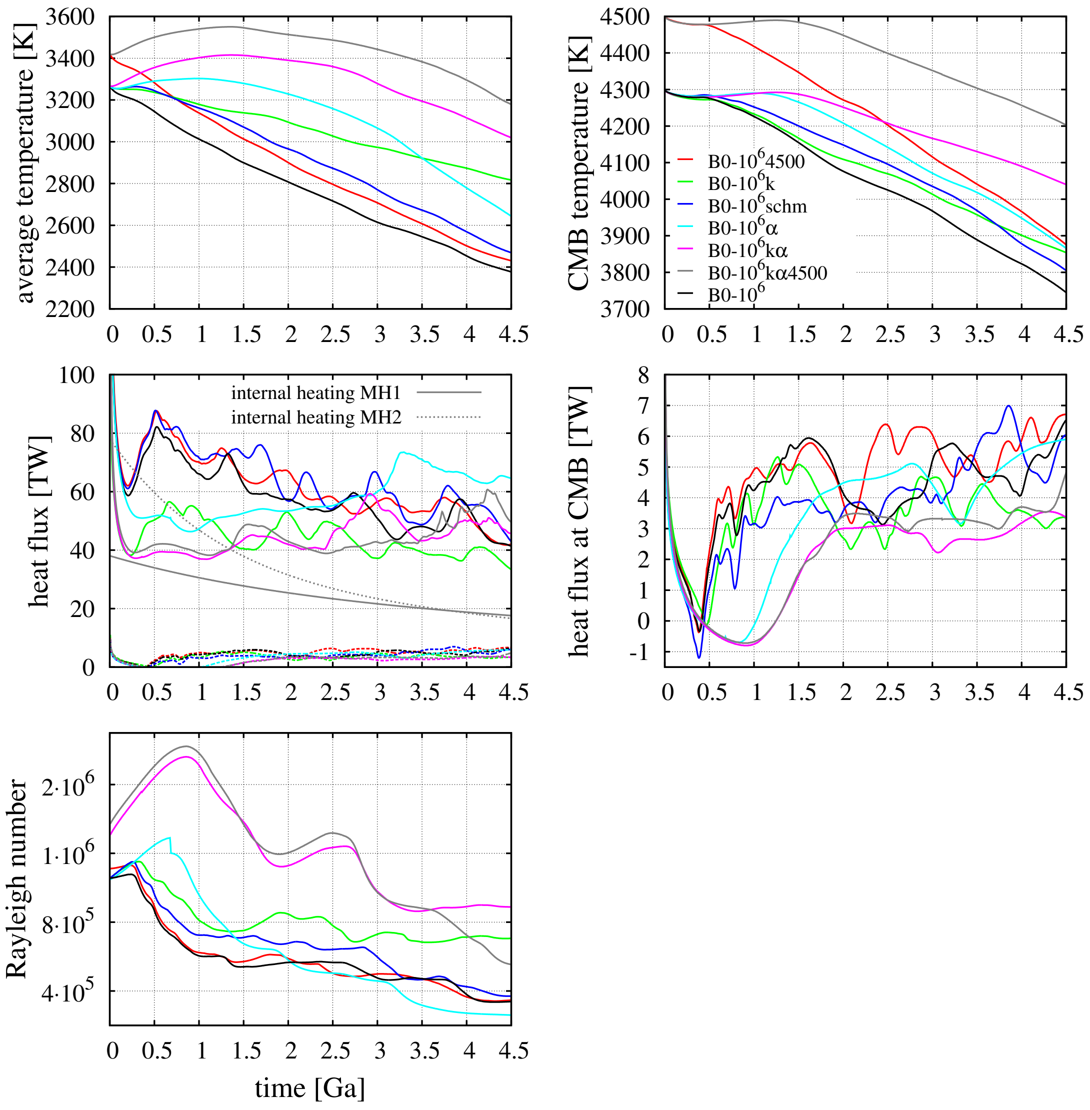

Figure 4.9: Models B0-10^6P: time evolution of selected quantities.

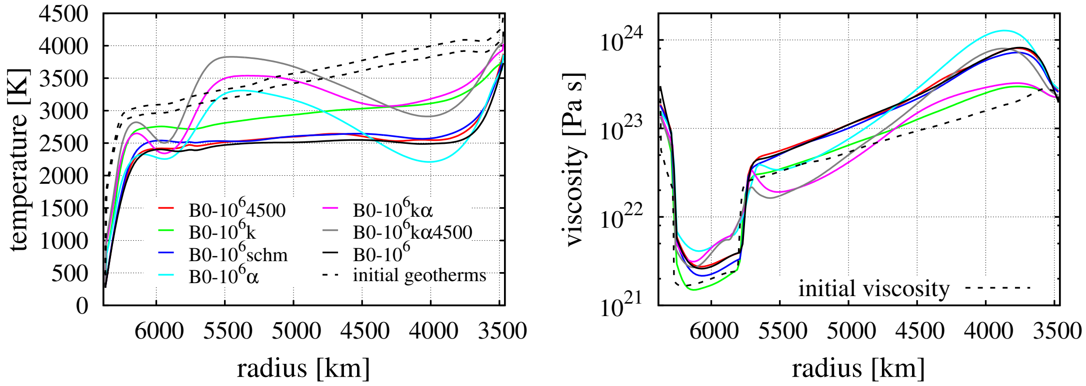

Figure 4.10: Models B0-10^6P: radial profiles of the horizontally averaged temperature (left) and viscosity (right) at $t = 0$ and 4.5 Ga

Now let us look at the same models but with weak PPV included. Snapshots of the temperature and the viscosity evolutions are in Fig. 4.11 and 4.12. We can observe similar behaviour as described for models B0-10^6 and B2-10^6. After about 500 mil. years, production of PPV starts (Fig. 4.13, layer of ppv), which highly enhances the CMB heat flux. This effect is most remarkable in model B2-$10^6\alpha$. In the thermal evolution (Fig. 4.12a), we observe massive downwellings, which, after reaching the bottom boundary expand along this boundary. Those regions of cold material are associated with thick large PPV lenses. The thickness of PPV layer in this model is the highest—about 450 km. Geotherm (Fig. 4.14, blue line) is characterised by an untypical decreasing trend throughout the mantle—massive heaps of cold material above CMB lower the average temperature considerably, and cause the above mentioned high CMB heat flux. Also the cooling rate is the highest here—CMB temperature falls from the initial 4300 K to 3500 K (Fig. 4.13, CMB temperature) at the end of the simulation in the model including PPV. This is about 400 K lower then in the model without PPV (see Fig. 4.15, where all models—with and without PPV phase change—are plotted together).

On the other hand model B2-10^6k (Fig. 4.11c) shows only minor differences compared to its corresponding model B0-10^6k without PPV (Fig. 4.7c). Depth-dependent conductivity suppresses the cooling, and thus the production of PPV is only moderate. A considerable amount of PPV appears after $\sim$ 3.5 Ga of evolution, and reaches 120 km thick layer at the maximum (Fig. 4.13, green line). Consequently, the decrease in CMB temperature is only about 50 K compared to model B0-10^6k without PPV (Fig. 4.15), which is too mild to affect the average temperature or the surface heat flux, and also the final geotherm and the average viscosity are the same (Fig. 4.16). As mentioned while discussing the reference model, the introduction of PPV phase results in a slightly different convection pattern. Looking at the temperature evolution of models B0-$10^6$4500 (Fig. 4.7a) and B2-$10^6$4500 (Fig. 4.11a), we can see that in the model without PPV, downwellings are thicker and after reaching CMB spread there and form a broad cold anomaly at the base of the mantle. This cold anomaly is large enough to considerably affect volume average mantle temperature. This effect is not as strong in the model with PPV and although the CMB temperature is lower (about 100 K), the average temperature is about 50 K higher, compared to model B0-$10^6$4500 (Fig. 4.15, red lines). Similar observation can be made for models B-10^6schm, only the effect is weaker.

Temperature

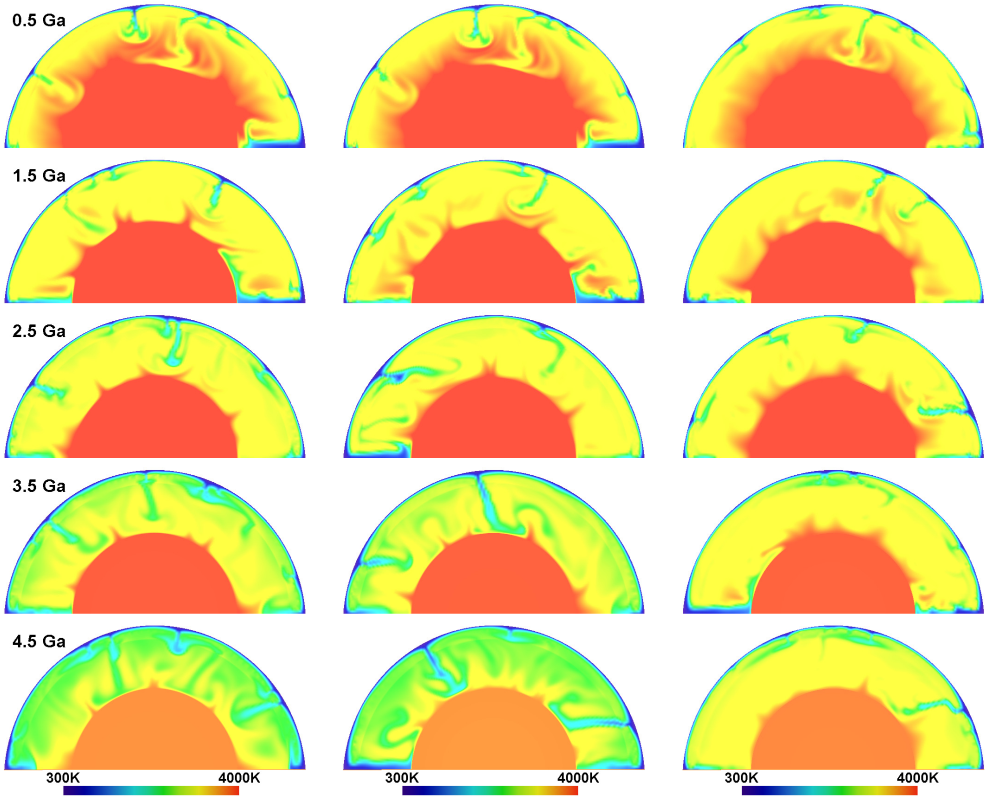

(a) B2-$10^6$4500 **(b)** B2-10^6schm **(c)** B2-10^6k

Viscosity

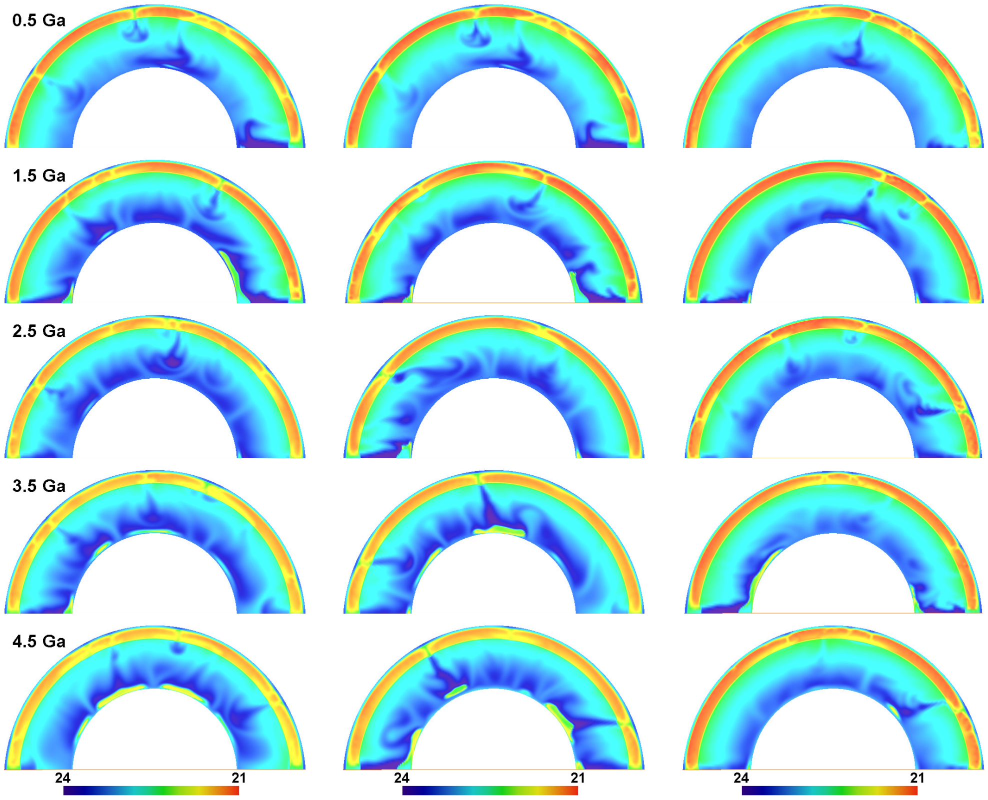

(d) B2-$10^6$4500 **(e)** B2-10^6schm **(f)** B2-10^6k

Figure 4.11: Models B2-10^6P: evolution of temperature and viscosity (in log-scale)

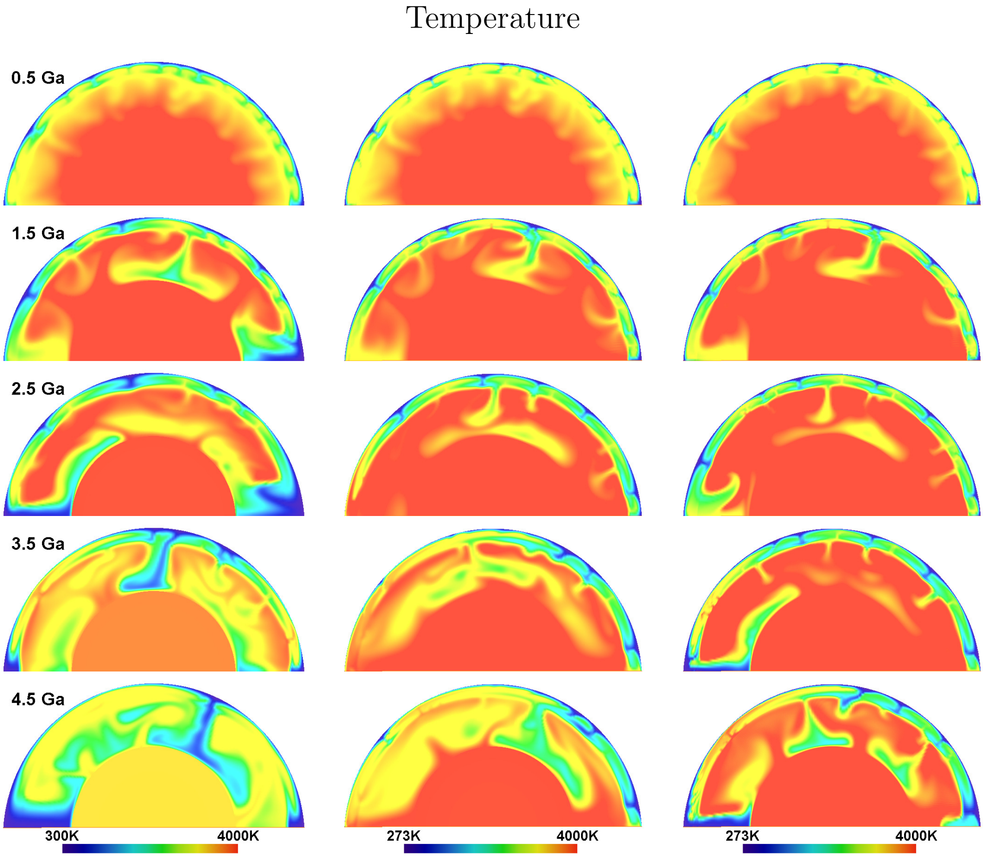

Temperature

(a) B2-$10^6\alpha$ **(b)** B2-10^6kα **(c)** B2-10^6kα4500

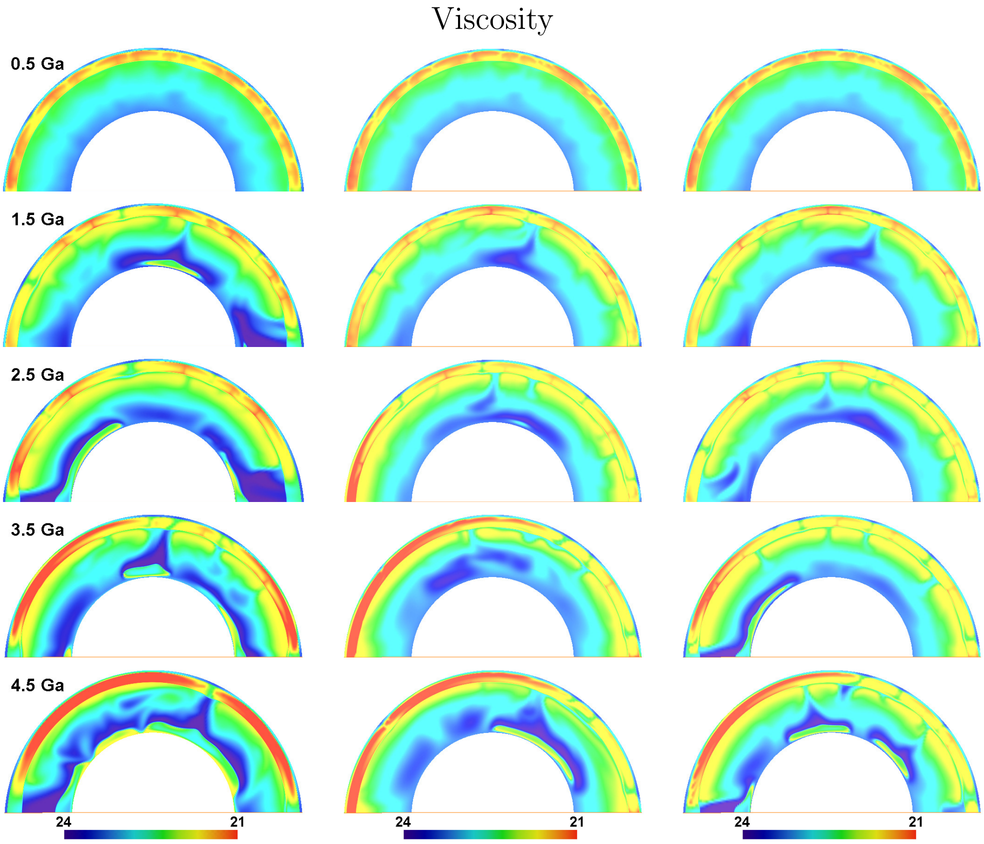

Viscosity

(d) B2-$10^6\alpha$ **(e)** B2-10^6kα **(f)** B2-10^6kα4500

Figure 4.12: Models B2-10^6P: evolution of temperature and viscosity (in log-scale)

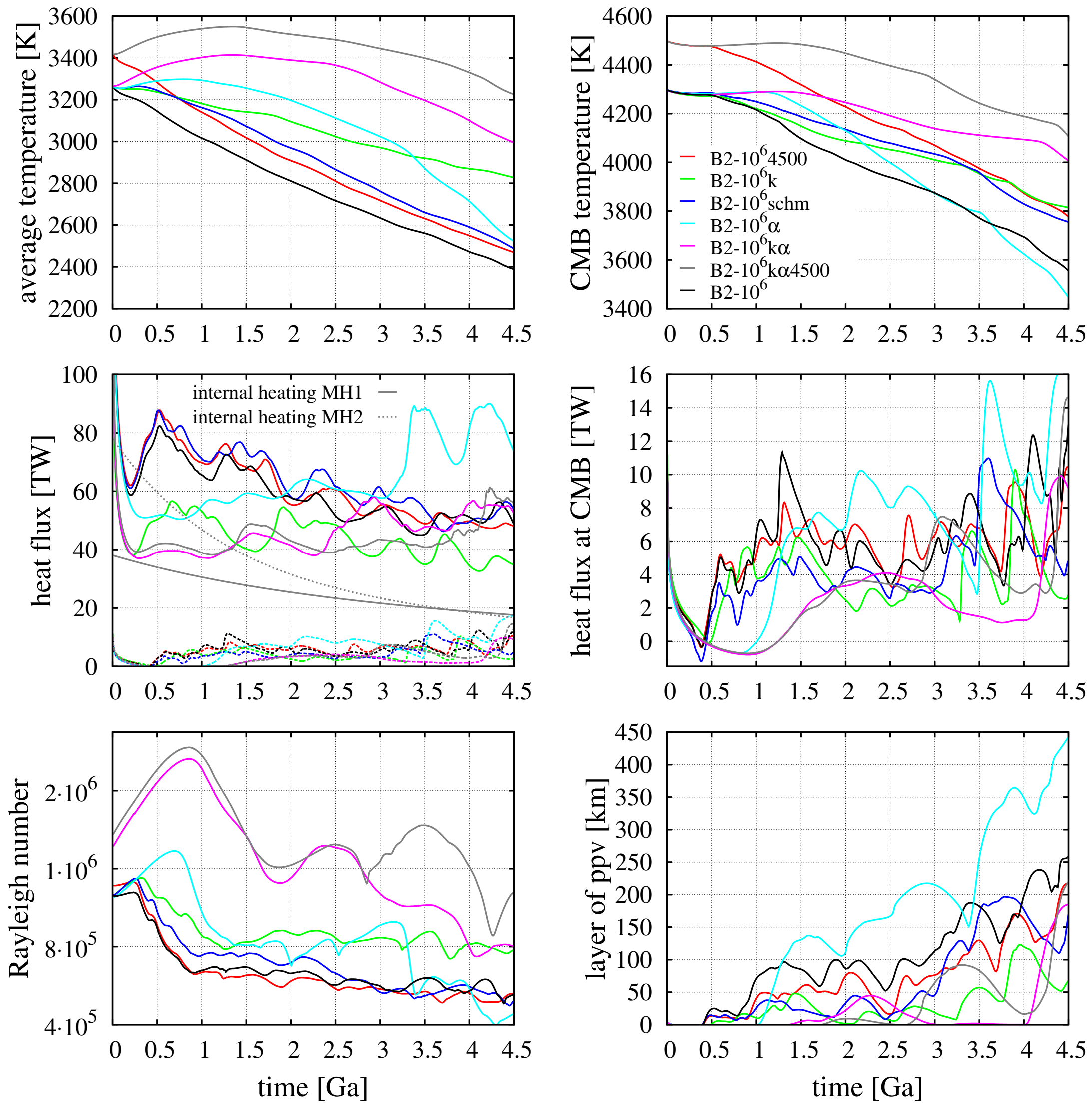

Figure 4.13: Models B2-10^{6}P: time evolution of selected quantities.

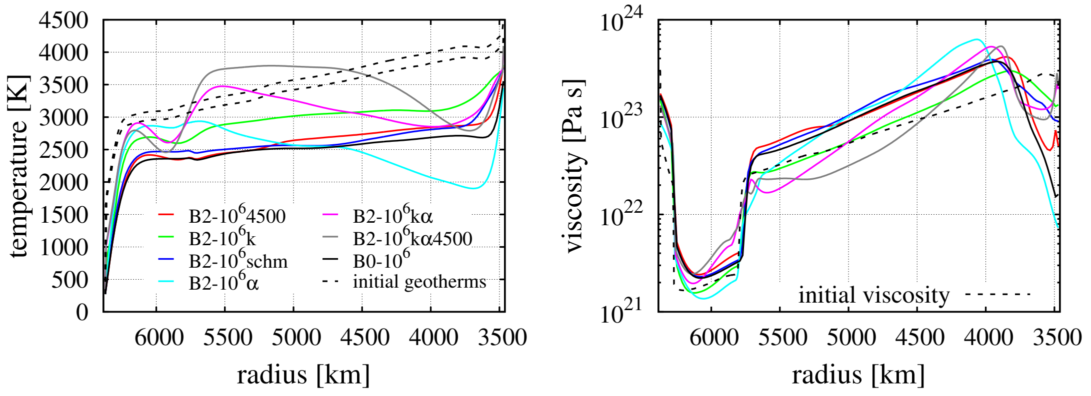

Figure 4.14: Models B2-10^{6}P: radial profiles of the horizontally averaged temperature (left) and viscosity (right) at $t = 0$ and 4.5 Ga

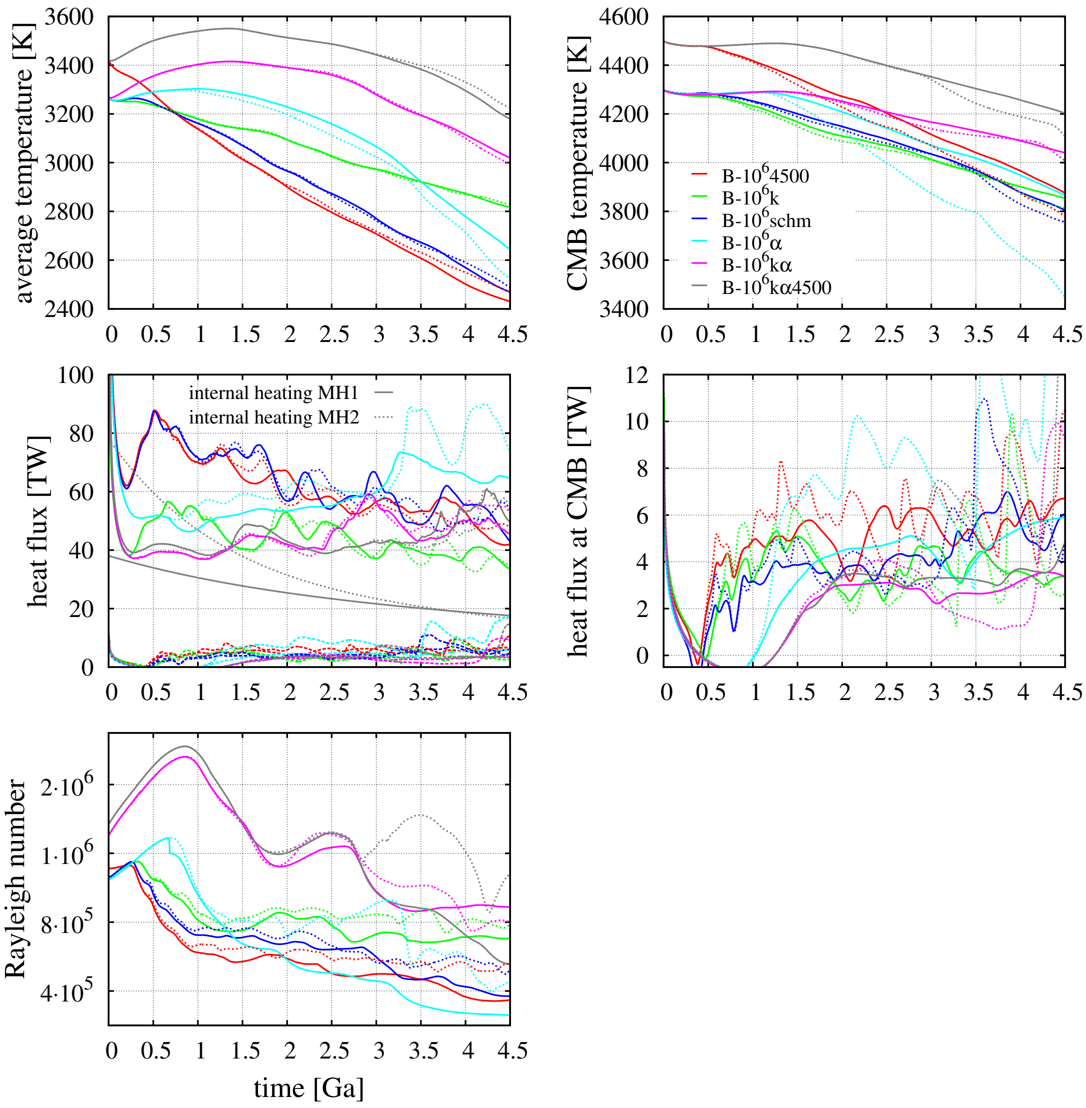

Figure 4.15: Models B-10^{6}P: time evolution of selected quantities. Solid line is for models without PPV and dashed line with PPV transition.

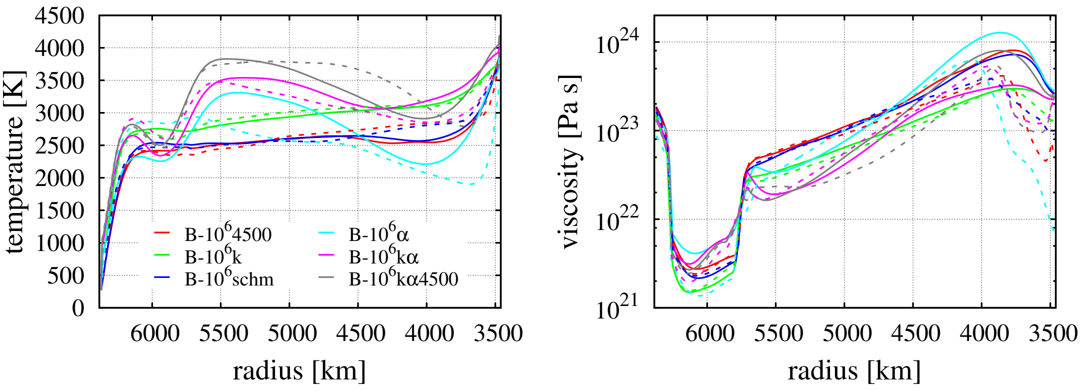

Figure 4.16: Models B-10^{6}P: radial profiles of the horizontally averaged temperature (left) and viscosity (right) at $t = 0$ and 4.5 Ga. Solid line is for models without PPV and dashed line with PPV transition.

4.2.3 B-10^7

Finally, we will evaluate effects of higher initial $Ra = 10^7$. We will use the model with combined effects of depth-dependent parameters $k(r)$ and $\alpha(r)$ and higher initial CMB temperature. This model is thus comparable to the model B-10^6kα4500—the only difference is in Ra. The temperature and viscosity evolution is displayed in Fig. 4.17, time evolution selected quantities are displayed in Fig. 4.18 (plotted together with the corresponding $Ra = 10^6$ model) and the resulting profile of temperature and viscosity is in Fig. 4.19.

Weak PPV in combination with depth-dependent properties have much stronger effect in this more vigorous convection model with depth-dependent parameters. Endothermic phase transition at 660 km associated with viscosity increase now enforces partially layered convection. Strong features penetrate the boundary and therefore, we observe downwellings reaching CMB (Fig. 4.17a, 4.17b). However, the boundary is blocking small-scale flow which results in substantial temperature contrast between the upper and lower mantle (see also geotherm in Fig. 4.19). PPV first appears in the model after 1 Ga evolution from the initial state in sporadic isolated patches (Fig. 4.18 layer of PPV)—earlier than in a corresponding model with lower Ra. These patches are caused by an avalanche of cold upper mantle material penetrating 660 km boundary and arriving at the CMB. Presence of weak PPV is reflected in increased CMB heat flux (Fig. 4.18 heat flux at CMB) and somewhat enhanced core cooling (Fig. 4.18 CMB temperature). PPV then temporarily disappears and until 2.5 Ga plays hardly any role. At 2.5 Ga next massive avalanche of cold material cools lowermost mantle and since that moment PPV lenses are present and core cooling is much more efficient. Final core temperature is thus by more than 400 K lower than in the case without weak PPV and average mantle temperature is by about 70 K higher (Fig. 4.18 average temperature). Vigorous convection of higher Ra models is much more efficient in removing heat from the lower mantle and therefore, we do not observe temporary increase of mantle temperature.

Enhanced mobility of the lowermost mantle is further demonstrated in the shift of the spectra of temperature anomalies (Fig. 4.20). While model without PPV is characterised by longer wavelength anomalies in the lower half of the mantle, including weak PPV shifts the spectral content towards higher degrees thus indicating smaller-scale features.

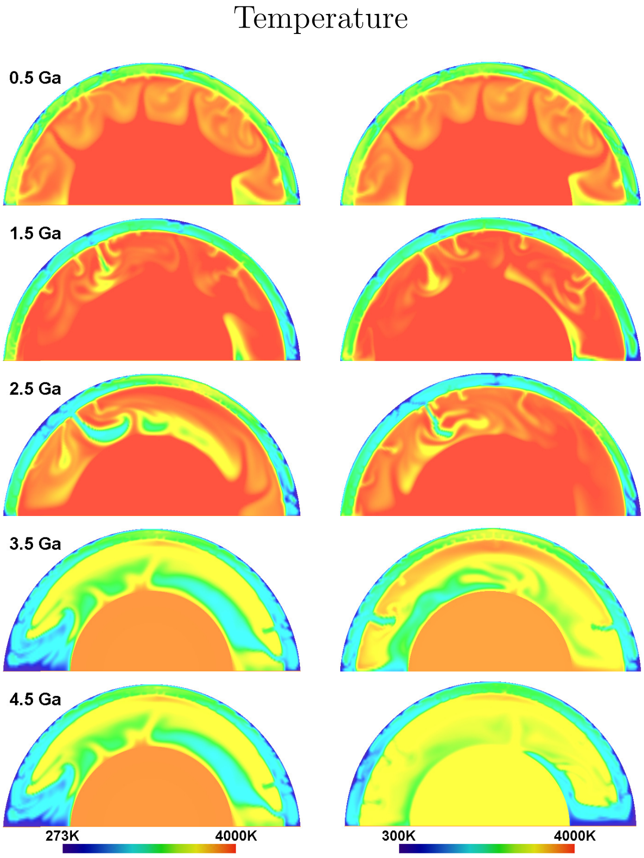

(a) B0-10^7 **(b)** B2-10^7

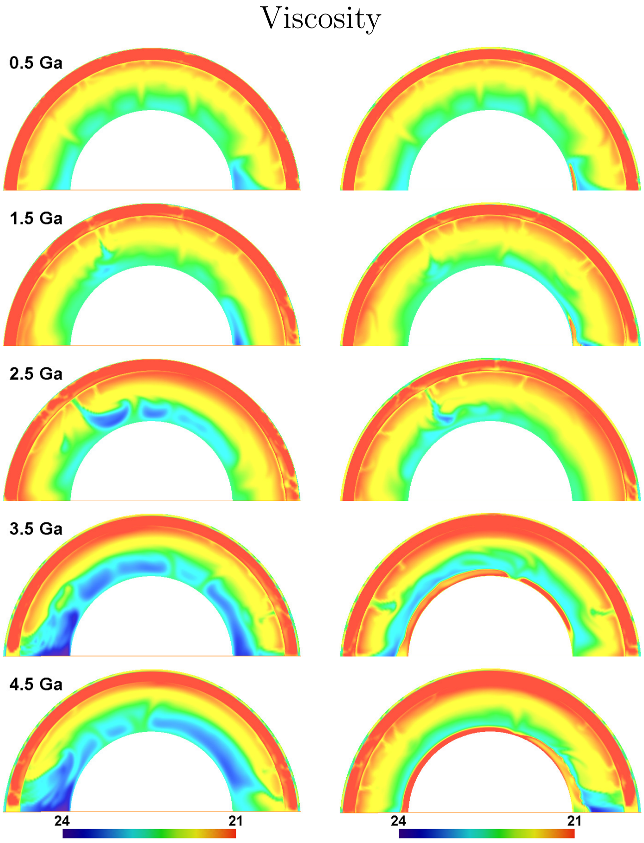

(c) B0-10^7 **(d)** B2-10^7

Figure 4.17: Models B-10^7: evolution of temperature and viscosity (in log-scale)

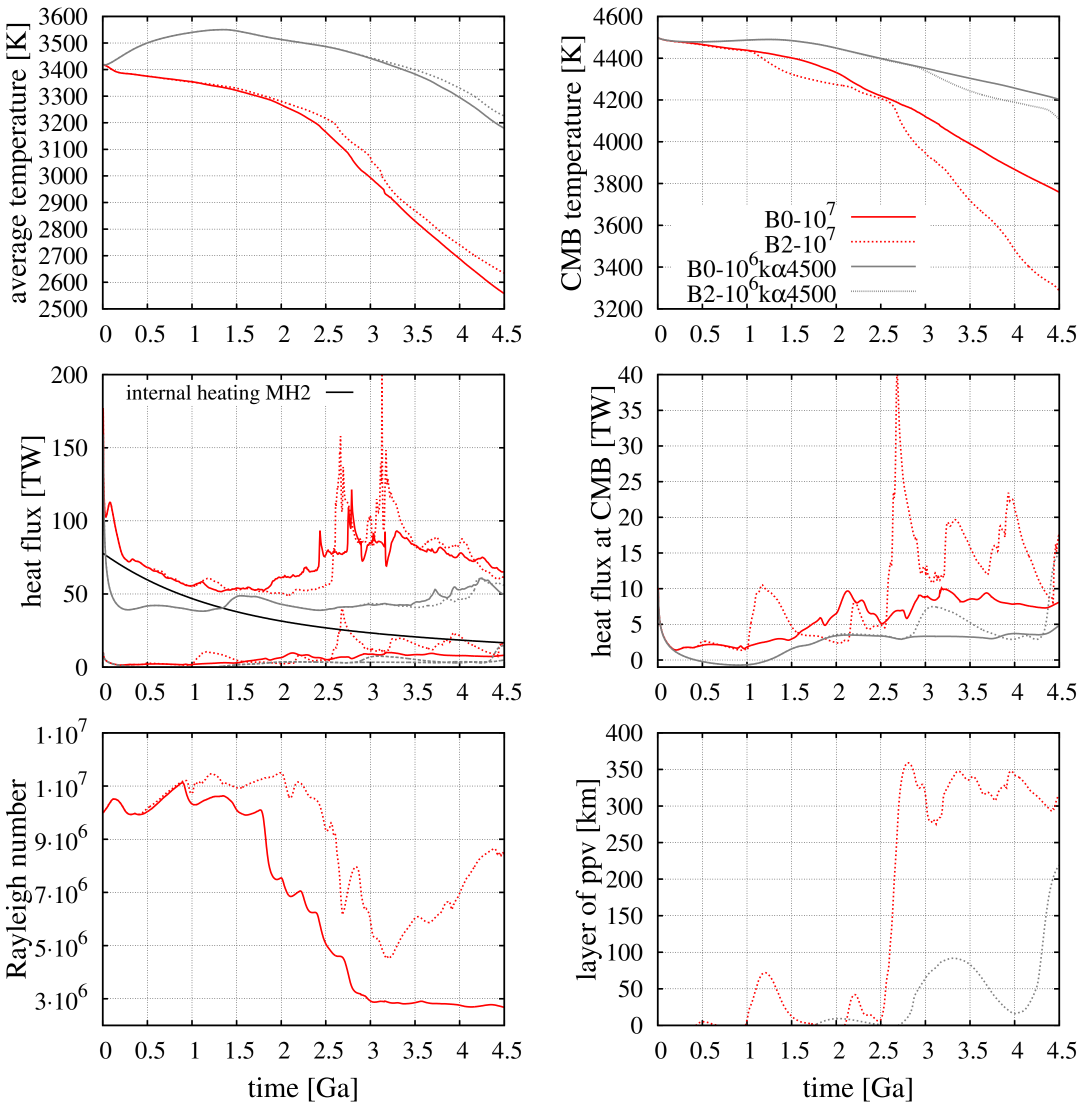

Figure 4.18: Models B-10^7: time evolution of selected quantities.

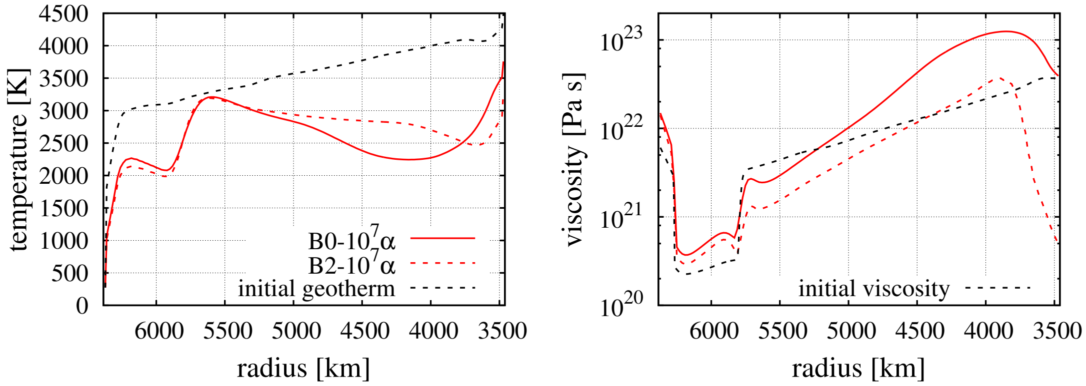

Figure 4.19: Models B-10^7: radial profiles of the horizontally averaged temperature (left) and viscosity (right) at $t = 0$ and 4.5 Ga.

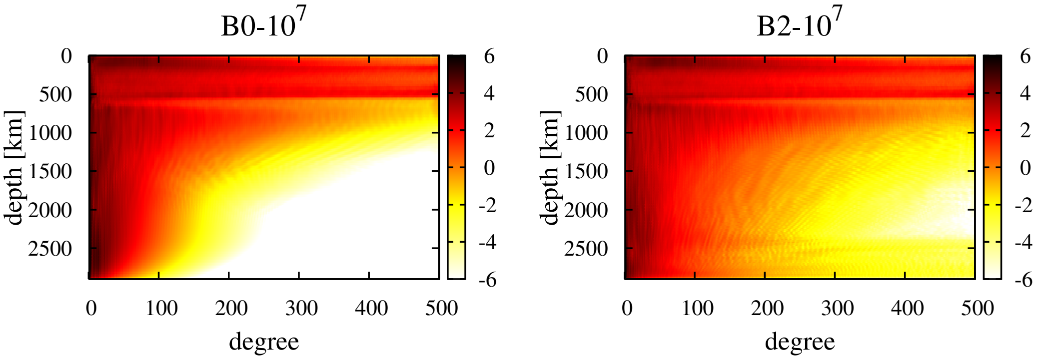

Figure 4.20: Models B-10^7: averaged temperature spectra over last 0.5 Ga

4.3 Concluding remarks

The effects of variable material properties (thermal expansivity, diffusivity) on mantle convection were already discussed in numerous studies. Decreasing expansivity and increasing diffusivity both suppress convective vigour in the deep mantle and they result in larger scale structures. Increase of thermal conductivity in the lower mantle supports generation of broad lower mantle plumes (e.g. Matyska et al., 1994; Dubuffet et al., 2002) and increases mantle temperature (van den Berg and Yuen, 2002; Monnereau and Yuen, 2010). van den Berg et al. (2005a) studied effects of thermal conductivity on mantle thermal evolution and concentrated on contributions from both phonon and radiative components of conductivity (Hofmeister (1999)). They report that temperature and pressure dependent phonon conductivity delays cooling thanks to relatively low conductivity at shallow depths, while radiative contribution that increases lowermost mantle conductivity supports heat extraction from the core and enhances cooling. Here, we also observe that including depth-dependent conductivity and expansivity in the models with lower Ra and without weak PPV increases average mantle temperature and delays secular cooling through the formation of a less conductive layer in the uppermost mantle and through less vigorous flow in the lower mantle. Weak PPV has only mild effects on the average mantle temperature, however, it significantly affects resulting core temperature and heat flux.

In agreement with previous studies (e.g. Nakagawa and Tackley, 2011), we show that weak PPV in the bottom thermal boundary layer tends to destabilize flow and enhance convective vigour. Core-mantle temperature decreases faster in the presence of PPV phase at the base of the mantle (resulting temperature may be by more than 400 K lower). On the other hand, it seems that this effect is localised in the bottom mantle and effects of weak PPV on the average mantle temperature are rather small (up to ~ 100 K). This is also in accordance with published results (Tackley et al., 2007). Weak PPV further enhances CMB heat flux (Nakagawa and Tackley, 2011; Čížková et al., 2010; Li et al., 2014). Heat flux variations over time reflect episodes of massive cold downwellings arriving at the CMB associated with PPV formation. Such episodic heat flux variations may be required to induce changes in geodynamo reversal behaviour (Biggin et al., 2012).

The presented model is certainly oversimplified in several aspects. Among them, the axisymmetric 2D approximation of a 3D process, the absence of compositional heterogeneity in the lowermost mantle and rheology yielding a mobile-lid instead of plate tectonics are perhaps most limiting ones. Therefore, the model cannot provide complex and fully realistic description of the cooling process. On the other hand, our results demonstrate that rheologically weak PPV significantly enhances core cooling and its effect on the core temperature is opposite and comparable in amplitude with the effects of other key parameters such as thermal conductivity or expansivity. Associated CMB heat flux variations, especially during massive cold downwelling events, may affect core dynamo action.

5. Detectability of 3D Post-Perovskite Distribution by Electromagnetic Induction

As discussed above, though the presence of PV-PPV change is now generally accepted, the spatial distribution of PPV is still not well described. Despite some evidence for possible PPV lens (e.g. Lay et al., 2006; van der Hilst et al., 2007; Hutko et al., 2008), reliable seismic detection of PV-PPV transition is still difficult. It is thus not clear whether PPV forms a continuous layer, a layer interrupted in the areas of hot rising plumes or rather isolated lenses in the areas of cold downwellings. An independent information constraining the PPV spatial distribution would be extremely useful.

The electromagnetic (EM) induction can potentially provide such a source of information. The electrical conductivity of PPV has been reported to be by up to 2 orders of magnitude higher than that of PV (Ono et al., 2006; Ohta et al., 2008, 2010). The conductivity anomaly of this order (though buried in the deepest mantle) should be reflected in the geomagnetic data. The EM induction by variations of external fields requires long-periodic or strong transient excitation in order to detect deep mantle structures. Geomagnetic storms, excited by the Sun, and manifested in the magnetosphere by energizing of the equatorial ring current, represent such a signal. They are capable of inducing secondary electric currents in the deepest regions of the Earth, including the core (Velímský and Finlay, 2011). The magnetic field generated by the ring current has dominantly dipolar structure in the geomagnetic coordinate system defined by the Earth's main field. Although smaller non-axisymmetric contributions are also present (Balasis et al., 2004). While numerical methods for global 3D inversion of geomagnetic data is available and computationally feasible, so far, they have been applied only to the upper parts of the mantle (Kelbert et al., 2009) down to the depth of 1600 km. Below that, available data allow to study only 1D conductivity. The 1D conductivity profile obtained by Velímský (2010) in the inversion of CHAMP satellite data did not show any significant increase in D$''$ and thus did not agree with the experimental data by Ono et al. (2006) and Ohta et al. (2008, 2010).

However, that does not necessarily mean that a highly conductive PPV is not present there. If the PPV does not form a continuous layer, but rather isolated patches, their high conductivity may not show up unless they are interconnected

Figure 5.1: 3D images of PPV distribution A (left) and B (right).

in the equatorial direction, that is in the direction of prevailing currents. Velímský et al. (2012) tested this possibility by performing a synthetic EM data inversion. His synthetic models of external field were constructed for 6 distributions of highly conductive material in the lowermost mantle. Four of them were simple geometric structures (continuous highly conductive PPV layer, circular conductive belt in equatorial or meridional direction and model without PPV). We supplemented this study by producing two lowermost mantle conductivity structure derived from the 3D mantle convection simulation.

5.1 Construction of PPV distribution

These two PPV distributions should reflect two scenarios of PPV distribution: A) global PPV layer interrupted only in the areas of hottest upwellings. B) isolated PPV lenses present only in the areas where cold downwelling material is deposited. Here we constructed the syntetic PPV distribution corresponding to the above mentioned scenarios, by executing 3D convection model with varying T_{int}. In order to obtain global layer of PPV (A) we used $T_{int} = 3900$ K while to obtain isolated PPV patches (B) we used $T_{int} = 3000$ K. Other parameters were fixed for both scenarios: Clapeyron slope is $9 \cdot 10^6$ Pa K^{-1}, Rayleigh number is 10^6, radial profile of viscosity is characterised by 100 km thick lithosphere (relative viscosity 100), in the upper mantle viscosity is 1 and under 660 km viscosity is 50 and is constant in the rest of the mantle. Resolution of the model was 20 km in radial direction and cut-off degree was 200. Resulting PPV distributions in both cases are shown in Fig. 5.1.

5.2 PPV detection

Both our PPV distribution models were used for synthetic EM inversion (Velímský et al., 2012). Results show that geometry of this layer is crucial for PPV visibility in 1D conductivity inversion. If there is a continuous layer of highly conductive PPV, it is visible in 1D inversion results. On the other hand, if conductive PPV is not interconnected in the equatorial direction (which is the direction of prevailing induced currents) it is not detected by 1D inversion. Thus significant amount of PPV can be present, even if it is not revealed in 1D results. This can be the case of the real Earth, where the presence of hot plumes below central Pacific and Africa probably interrupts PPV layer. As no highly conductive layer was reported in the lowermost mantle in real EM data inversions, results of (Velímský et al., 2012) suggest that discontinuous (lens) PPV distribution from our convection model may reflect the real situation.

Conclusions

In this thesis, we addressed several questions concerning mantle convection in the terrestrial bodies. We developed and tested the code for numerical simulations of mantle convection in 2D axisymmetric and 3D spherical geometry and applied it to problems related to Earth, Venus and Mercury thermal evolution.

We concentrated on three main issues: i) constraining viscosity structure of Venus using its gravity and topography data, ii) finding out whether Mercury geoid and topography could be supported by mantle convection and iii) evaluating the effects of rheologically distinct post-perovskite on secular cooling of the Earth.

In the first part, we tried to extend knowledge of the structure and dynamics of the Venusian mantle. We performed a search for the viscosity and density models that would most closely fit the spectra of observed geoid and dynamic topography. We selected four possible radial viscosity profiles and for each of them we generated a broad group of models with varying Rayleigh number (that controls the character of thermally induced density anomalies) and with weaker or stronger lateral variations of viscosity. Further, we monitored the topography and the geoid developing above individual plumes and compared them with the observed elevations of Venus' geoid and topography in several Regii. We conclude that the best fitting viscosity profile is characterised by the upper mantle viscosity of $2{\cdot}10^{21}$ Pa s, with a strong 200 km thick lithosphere, without an asthenosphere and with a gradual viscosity increase in the underlying mantle. Lateral variations of viscosity play only a minor role and do not significantly improve the fit. Our models predict the observed spectra well only up to the degree of about 40 thus indicating other then dynamic origin of the geoid and topography anomalies for higher degrees.

Similar analysis applied to Mercury employed recent measurements of MESSENGER mission. We assumed that Mercurian mantle is currently still convecting and we tried to predict the spectra of its geoid and topography in terms of our convection models. Contrary to the above summarised results for Venus, we were not able to predict the observed geoid and topography. This negative result is in agreement with recently published analysis of geoid and topography data, that suggests other mechanisms to be important, namely variations of crustal thickness and (possibly compositional) deep mantle anomalies. It also provides an indirect indication that perhaps Mercurian mantle convection already ceased as suggested by several authors.

Last part of the thesis is focused on the effects of PPV in the Earth mantle convection and on its spatial distribution. Simulations of a long-term evolution of the mantle take into account decaying radiogenic heat sources, variable material properties and thermal coupling between the mantle and the core. We conclude that weak PPV in the bottom thermal boundary layer tends to destabilize flow, increase convective vigour and enhance CMB heat flux. This results in a considerably lower CMB temperature, but the effect on the average mantle temperature is small. On the other hand, while presence of weak PPV enhances the secular cooling, depth-dependent material parameters (thermal expansivity and diffusivity) tend to delay the secular cooling.

Finally, thermal structures produced in our numerical models were used in the synthetic inversion of EM data that tried to determine possible detectability of highly conductive PPV lenses. PPV distribution obtained in our 3D thermal convection models was used as one possible synthetic input for EM inversion. Results suggest that highly conductive PPV is only visible if its spatial distribution is interconnected in the equatorial direction. Isolated conductive PPV lenses resulting from our convection simulations could not be detected by 1D EM inversion. The fact that 1D inversion of real data did not detect highly conductive layer at the base of the mantle thus indicates that PPV is probably indeed present there in isolated patches rather than in a continuous layer.

Bibliography

AHARONSON, O., ZUBER, M. T. and SOLOMON, S. C. Crustal remanence in an internally magnetized non-uniform shell: a possible source for Mercury's magnetic field? *Earth Planet. Sci. Lett.* 2004, 218, 3–4, pp. 261 – 268.

AMIT, H. and CHOBLET, G. Mantle-driven geodynamo features-effects of post-perovskite phase transition. *Earth Planets Space.* 2009, 61, 11, pp. 1255–1268.

AMMANN, M. W. et al. First-principles constraints on diffusion in lower-mantle minerals and a weak D″ layer. *Nature.* May 2010, 465, 7297, pp. 462–465.

ANDERSON, B. J. et al. The Global Magnetic Field of Mercury from MESSENGER Orbital Observations. *Science.* 2011, 333, 6051, pp. 1859–1862.

ANDRAULT, D. et al. Experimental evidence for perovskite and post-perovskite coexistence throughout the whole D" region. *Earth Planet. Sci. Lett.* 2010, 293, 1–2, pp. 90 – 96.

ARMANN, M. and TACKLEY, P. J. Simulating the thermochemical magmatic and tectonic evolution of Venus's mantle and lithosphere: Two-dimensional models. *J. Geophys. Res.* 2012, 117, E12.

BALASIS, G., EGBERT, G. D. and MAUS, S. Local time effects in satellite estimates of electromagnetic induction transfer functions. *Geophys. Res. Lett.* 2004, 31, 16.

BARNETT, D. N., NIMMO, F. and MCKENZIE, D. Flexure of Venusian lithosphere measured from residual topography and gravity. *J. Geophys. Res.* 2002, 107, E2, pp. 5007.

BĚHOUNKOVÁ, M. et al. Coupling mantle convection and tidal dissipation: applications to Enceladus and Earth-like planets. *J. Geophys. Res.* 2010, 115, pp. E09011.

BENEŠOVÁ, N. and ČÍŽKOVÁ, H. Geoid and topography of Venus in various thermal convection models. *Stud. Geophys. Geod.* 2012, 56, 2, pp. 621–639.

BENZ, W., SLATTERY, W. L. and CAMERON, A. Collisional stripping of Mercury's mantle. *Icarus.* 1988, 74, 3, pp. 516 – 528.

BERCOVICI, D. et al. Three-dimensional thermal convection in a spherical shell. *J. Fluid Mech.* 1989, 206, pp. 75–104.

BERCOVICI, D., SCHUBERT, G. and GLATZMAIER, G. A. Modal growth and coupling in three-dimensional spherical convection. *Geophys. Astro. Fluid.* 1991, 61, pp. 149–159.

BIGGIN, A. J. et al. Possible links between long-term geomagnetic variations and whole-mantle convection processes. *Nature Geosci.* 2012, 5, 9, pp. 674.

BLEWETT, D. T. et al. Hollows on Mercury: MESSENGER Evidence for Geologically Recent Volatile-Related Activity. *Science.* 2011, 333, 6051, pp. 1856–1859.

BREUER, D. and MOORE, W. 10.09 - Dynamics and Thermal History of the Terrestrial Planets, the Moon, and Io. In SCHUBERT, G. (Ed.) *Treatise on Geophysics.* Amsterdam: Elsevier, 2007. pp. 299 – 348.

BREUER, D. et al. Interior Evolution of Mercury. In BALOGH, A., KSANFOMALITY, L. and STEIGER, R. (Ed.) *Mercury,* 26 / *Space Sciences Series of ISSI.* Springer New York, 2008. pp. 47–78.

BUSSE, F. H. Patterns of convection in spherical shells. *J. Fluid Mech.* 1975, 72, pp. 67–85.

BUSSE, F. H. and RIAHI, N. Patterns of convection in spherical shells. Part 2. *J. Fluid Mech.* 1982, 123, pp. 283–301.

ČADEK, O. and FLEITOUT, L. Effect of lateral viscosity variations in the top 300 km on the geoid and dynamic topography. *Geophys. J. Int.* 2003, 152, 3, pp. 566–580.

ČADEK, O. and FLEITOUT, L. Effect of lateral viscosity variations in the core-mantle boundary region on predictions of the long-wavelength geoid. *Stud. Geophys. Geod.* 2006, 50, pp. 217–232.

CARREZ, P., FERRÉ, D. and CORDIER, P. Peierls−Nabarro model for dislocations in $MgSiO_3$ post-perovskite calculated at 120 GPa from first principles. *Philos. Mag.* 2007, 87, 22, pp. 3229–3247.

CATALLI, K., SHIM, S.-H. and PRAKAPENKA, V. Thickness and Clapeyron slope of the post-perovskite boundary. *Nature.* 2009, 462, 7274, pp. 782–785.

CHOBLET, G. et al. ŒDIPUS: a new tool to study the dynamics of planetary interiors. *Geophys. J. Int.* 2007, 170, 1, pp. 9–30.

CHRISTENSEN, U. R. and YUEN, D. A. Layered convection induced by phase transitions. *J. Geophys. Res.* 1985, 90, B12, pp. 10291–10300.

ČÍŽKOVÁ, H. and ČADEK, O. Effect of a Viscosity Interface at 1000 km Depth on Mantle Circulation. *Stud. Geophys. Geod.* 1997, 41, pp. 297–306.

ČÍŽKOVÁ, H. and MATYSKA, C. Layered convection with an interface at a depth of 1000 km: stability and generation of slab-like downwellings. *Phys. Earth Planet. Inter.* 2004, 141, 4, pp. 269 – 279. Structure and tectonics of convergent plate margins.

ČÍŽKOVÁ, H. et al. Slope of geoid spectrum and constraints on mantle viscosity stratification. *Geophys. Res. Lett.* 1996, 23, pp. 3063–3066.

ČÍŽKOVÁ, H. et al. Implications of post-perovskite transport properties for core–mantle dynamics. *Phys. Earth Planet. In.* 2010, 180, pp. 235–243.

DI ACHILLE, G. et al. Mercury's radius change estimates revisited using MESSENGER data. *Icarus.* 2012, 221, 1, pp. 456 – 460.

DOMINGUE, D. et al. Mercury's Atmosphere: A Surface-Bounded Exosphere. In DOMINGUE, D. and RUSSELL, C. (Ed.) *The Messenger Mission to Mercury.* Springer New York, 2007. pp. 161–186.

DUBUFFET, F., YUEN, D. A. and RAINEY, E. S. G. Controlling thermal chaos in the mantle by positive feedback from radiative thermal conductivity. *Nonlinear Proc. Geoph.* 2002, 9, 3/4, pp. 311–323.

FEGLEY, B. and CAMERON, A. A vaporization model for iron/silicate fractionation in the Mercury protoplanet. *Earth. Planet. Sc. Lett.* 1987, 82, 3–4, pp. 207 – 222.

FORNBERG, B. Generation of finite-difference formulas on arbitrarily spaced grids. *Math. Comput.* 1988, 51, pp. 699–706.

GROTT, M., BREUER, D. and LANEUVILLE, M. Thermo-chemical evolution and global contraction of Mercury. *Earth. Planet. Sc. Lett.* 2011, 307, 1–2, pp. 135 – 146.

HAGER, B. H. and CLAYTON, R. W. *Constraints on the structure of mantle convection using seismic observations, flow models and the geoid*, pp. 657–763. Gordon and Breach Scientific Publishers, 1989.

HEAD, J. W. et al. Volcanism on Mercury: Evidence from the first MESSENGER flyby for extrusive and explosive activity and the volcanic origin of plains. *Earth. Planet. Sc. Lett.* 2009, 285, 3–4, pp. 227 – 242.

HEISKANEN, W. and MORITZ, H. *Physical geodesy.* Series of books in geology. W. H. Freeman, 1967.

HERNLUND, J. W., THOMAS, C. and TACKLEY, P. J. A doubling of the post-perovskite phase boundary and structure of the Earth's lowermost mantle. *Nature.* 2005, 434, pp. 882–886.

HIREMATH, K. Magnetic field structure of Mercury. *Planet. Space. Sci.* 2012, 63–64, pp. 8 – 14.

HIROSE, K. et al. Unsolved problems in the lowermost mantle. *Geophys. Res. Lett.* 2006, 33, L13S01.

HIROSE, K. Postperovskite phase transition and its geophysical implications. *Rev. Geophys.* 2006, 44, pp. RG3001.

HOFMEISTER, A. M. Mantle Values of Thermal Conductivity and the Geotherm from Phonon Lifetimes. *Science.* 1999, 283, 5408, pp. 1699–1706.

HUNT, S. A. et al. Weakening of calcium iridate during its transformation from perovskite to post-perovskite. *Nat. Geosci.* 2009, 2, pp. 794–797.

HUNT, S. A. et al. On the increase in thermal diffusivity caused by the perovskite to post-perovskite phase transition and its implications for mantle dynamics. *Earth. Planet. Sc. Lett.* 2012, 319–320, 0, pp. 96–103.

HUTKO, A. R. et al. Anticorrelated Seismic Velocity Anomalies from Post-Perovskite in the Lowermost Mantle. *Science.* 2008, 320, 5879, pp. 1070–1074.

IRIFUNE, T. and TSUCHIYA, T. 2.03 - Mineralogy of the Earth – Phase Transitions and Mineralogy of the Lower Mantle. In SCHUBERT, G. (Ed.) *Treatise on Geophysics.* Amsterdam: Elsevier, 2007. pp. 33–62.

ITA, J. and KING, S. D. Sensitivity of convection with an endothermic phase change to the form of governing equations, initial conditions, boundary conditions, and equation of state. *J. Geophys. Res.* 1994, 99, B8, pp. 15919–15938.

JAMES, P. B. et al. Support of long-wavelength topography on Mercury inferred from MESSENGER measurements of gravity and topography. *J. Geophys. Res.* 2015, 120, 2, pp. 287–310.

KARATO, S. The influence of anisotropic diffusion on the high-temperature creep of a polycrystalline aggregate. *Phys. Earth Planet. In.* 2010, 183, 3–4, pp. 468 – 472.

KARATO, S., RIEDEL, M. R. and YUEN, D. A. Rheological structure and deformation of subducted slabs in the mantle transition zone: implications for mantle circulation and deep earthquakes. *Phys. Earth Planet. Inter.* 2001, 127, 1–4, pp. 83 – 108.

KAULA, W. M. and PHILLIPS, R. J. Quantitative tests for plate tectonics on Venus. *Geophys. Res. Lett.* 1981, 8, 12, pp. 1187–1190.

KELBERT, A., SCHULTZ, A. and EGBERT, G. Global electromagnetic induction constraints on transition-zone water content variations. *Nature.* 2009, 460, pp. 1003 – 1006.

KIEFER, W. S. and HAGER, B. H. A mantle plume model for the Equatorial Highlands of Venus. *J. Geophys. Res.* 1991, 96, E4, pp. 20947–20966.

KIEFER, W. S. and KELLOGG, L. H. Geoid anomalies and dynamic topography from time-dependent, spherical axisymmetric mantle convection. *Phys. Earth Planet. In.* 1998, 106, 3–4, pp. 237–256.

KING, S. D. Geoid and topographic swells over temperature-dependent thermal plumes in spherical-axisymmetric geometry. *Geophys. Res. Lett.* 1997, 24, 23, pp. 3093–3096.

KING, S. D. Radial models of mantle viscosity: results from a genetic algorithm. *Geophys. J. Int.* 1995, 122, 3, pp. 725–734.

KING, S. D. Pattern of lobate scarps on Mercury's surface reproduced by a model of mantle convection. *Nat. Geosci.* 2008, 1, 4, pp. 229–232.

KING, S. et al. A Community Benchmark for 2D Cartesian Compressible Convection in th Earth's Mantle. *Geophys. J. Int.* 2010, 180, pp. 73–87.

KLIKA, M. Modelling the flow in a mantle with laterally dependent rheology. Master's thesis, Charles University, Prague, 1995.

KONOPLIV, A. S., BANERDT, W. B. and SJOGREN, W. L. Venus gravity: 180th degree and order model. *Icarus.* 1999, 139, pp. 3–18.

KORENAGA, J. Urey ratio and the structure and evolution of Earth's mantle. *Rev. Geophys.* 2008, 46, pp. 229–243.

LAY, T. 1.18 - Deep Earth Structure – Lower Mantle and D". In SCHUBERT, G. (Ed.) *Treatise on Geophysics.* Amsterdam: Elsevier, 2007. pp. 619 – 654.

LAY, T. et al. A Post-Perovskite Lens and D″ Heat Flux Beneath the Central Pacific. *Science.* 2006, 314, 5803, pp. 1272–1276.

LEWIS, J. S. Chemistry of the Planets. *Annu. Rev. Phys. Chem.* 1973, 24, 1, pp. 339–351.

LI, Y., DESCHAMPS, F. and TACKLEY, P. J. Effects of low-viscosity post-perovskite on the stability and structure of primordial reservoirs in the lower mantle. *Geophys. Res. Lett.* 2014, 41, 20, pp. 7089–7097.

LOWRIE, W. *Fundamentals of Geophysics.* Cambridge University Press, 2007.

MARGOT, J. L. et al. Large Longitude Libration of Mercury Reveals a Molten Core. *Science.* 2007, 316, 5825, pp. 710–714.

MARTINEC, Z. Program to calculate the spectral harmonic expansion coefficients of the two scalar fields product. *Comput. Phys. Commun.* 1989, 54, 1, pp. 177–182.

MATYSKA, C. and YUEN, D. Lower mantle material properties and convection models of multiscale plumes. In FOULGER, G. and JURDY, D. (Ed.) *Plates, plumes, and planetary processes: Geological Society of America Special Paper 430.* The Geological Society of America, 2007. pp. 137–163.

MATYSKA, C. and YUEN, D. A. The importance of radiative heat transfer on superplumes in the lower mantle with the new post-perovskite phase change. *Earth Planet. Sci. Lett.* 2005, 234, 1–2, pp. 71 – 81.

MATYSKA, C. and YUEN, D. A. Lower mantle dynamics with the post-perovskite phase change, radiative thermal conductivity, temperature- and depth-dependent viscosity. *Phys. Earth Planet. Inter.* 2006, 154, 2, pp. 196 – 207.

MATYSKA, C., MOSER, J. and YUEN, D. A. The potential influence of radiative heat transfer on the formation of megaplumes in the lower mantle. *Earth Planet. Sci. Lett.* 1994, 125, 1–4, pp. 255 – 266.

MATYSKA, C. et al. The impact of variability in the rheological activation parameters on lower-mantle viscosity stratification and its dynamics. *Phys. Earth Planet. In.* 2011, 188, 1–2, pp. 1 – 8.

McCUBBIN, F. M. et al. Is Mercury a volatile-rich planet? *Geophys. Res. Lett.* 2012, 39, 9.

McNUTT, R. L. J. et al. An international program for Mercury exploration: synergy of MESSENGER and BepiColombo. *Advances in Space Research.* 2004, 33, 12, pp. 2126 – 2132. Mercury, Mars and Saturn.

MICHEL, N. C. et al. Thermal evolution of Mercury as constrained by MESSENGER observations. *J. Geophys. Res.* 2013.

MONNEREAU, M. and YUEN, D. A. Seismic imaging of the D$''$ and constraints on the core heat flux. *Phys. Earth Planet. Inter.* 2010, 180, 3–4, pp. 258 – 270.

MOORE, W. B., SCHUBERT, G. and TACKLEY, P. J. The role of rheology in lithospheric thinning by mantle plumes. *Geophys. Res. Lett.* 1999, 26, 8, pp. 1073–1076.

MURAKAMI, M. et al. Post-Perovskite Phase Transition in $MgSiO_3$. *Science.* 2004, 304, 5672, pp. 855–858.

NAKAGAWA, T. and TACKLEY, P. J. Effects of a perovskite-postperovskite phase change near core-mantle boundary in compressible mantle convection. *Geophys. Res. Lett.* 2004, 31, 16.

NAKAGAWA, T. and TACKLEY, P. J. The interaction between the post-perovskite phase change and a thermo-chemical boundary layer near the core–mantle boundary. *Earth Planet. Sci. Lett.* 2005, 238, 1–2, pp. 204 – 216.

NAKAGAWA, T. and TACKLEY, P. J. Three-dimensional structures and dynamics in the deep mantle: Effects of post-perovskite phase change and deep mantle layering. *Geophys. Res. Lett.* 2006, 33, 12.

NAKAGAWA, T. and TACKLEY, P. J. Lateral variations in CMB heat flux and deep mantle seismic velocity caused by a thermal–chemical-phase boundary layer in 3D spherical convection. *Earth. Planet. Sc. Lett.* 2008, 271, 1–4, pp. 348–358.

NAKAGAWA, T. and TACKLEY, P. J. Influence of initial CMB temperature and other parameters on the thermal evolution of Earth's core resulting from thermochemical spherical mantle convection. *Geochem. Geophys. Geosyst.* 2010, 11, pp. Q06001.

NAKAGAWA, T. and TACKLEY, P. J. Effects of low-viscosity post-perovskite on thermo-chemical mantle convection in a 3-D spherical shell. *Geophys. Res. Lett.* 2011, 38, pp. L04309.

NAKAGAWA, T. and TACKLEY, P. J. Three-dimensional structures and dynamics in the deep mantle: Effects of post-perovskite phase change and deep mantle layering. *Geophys. Res. Lett.* 2012, 33, pp. L12S11.

NESS, N. et al. Observations of Mercury's magnetic field. *Icarus.* 1976, 28, 4, pp. 479 – 488.

NIMMO, F. and WATTERS, T. R. Depth of faulting on Mercury: Implications for heat flux and crustal and effective elastic thickness. *Geophys. Res. Lett.* 2004, 31, 2.

NITTLER, L. R. et al. The Major-Element Composition of Mercury's Surface from MESSENGER X-ray Spectrometry. *Science.* 2011, 333, 6051, pp. 1847–1850.

OGANOV, A. R. and ONO, S. Theoretical and experimental evidence for a post-perovskite phase of $MgSiO_3$ in Earth's D'' layer. *Nature.* 2004, 430, pp. 445–448.

OHTA, K. et al. The Electrical Conductivity of Post-Perovskite in Earth's D" Layer. *Science.* 2008, 320, pp. 89–91.

OHTA, K. et al. Electrical conductivities of pyrolitic mantle and MORB materials up to the lowermost mantle conditions. *Earth Planet. Sci. Lett.* 2010, 289, 3–4, pp. 497 – 502.

O'NEILL, C., JELLINEK, A. and LENARDIC, A. Conditions for the onset of plate tectonics on terrestrial planets and moons. *Earth. Planet. Sc. Lett.* 2007, 261, 1–2, pp. 20 – 32.

ONO, S. et al. Stability and compressibility of the high-pressure phases of Al_2O_3 up to 200 GPa: Implications for the electrical conductivity of the base of the lower mantle. *Earth. Planet. Sc. Lett.* 2006, 246, 3–4, pp. 326 – 335.

ORTH, C. P. and SOLOMATOV, V. S. The isostatic stagnant lid approximation and global variations in the Venusian lithospheric thickness. *Geochem. Geophys. Geosyst.* 2011, 12, 7.

PADOVAN, S. et al. Thickness of the crust of Mercury from geoid-to-topography ratios. *Geophys. Res. Lett.* 2015, 42, 4, pp. 1029–1038.

PANNING, M. and ROMANOWICZ, B. A three-dimensional radially anisotropic model of shear velocity in the whole mantle. *Geophys. J. Int.* 2006, 167, 1, pp. 361–379.

PAUER, M., FLEMING, K. and ČADEK, O. Modeling the dynamic component of the geoid and topography of Venus. *J. Geophys. Res.* 2006, 111, E11.

PEPLOWSKI, P. N. et al. Radioactive Elements on Mercury's Surface from MESSENGER: Implications for the Planet's Formation and Evolution. *Science.* 2011, 333, 6051, pp. 1850–1852.

PEPLOWSKI, P. N. et al. Variations in the abundances of potassium and thorium on the surface of Mercury: Results from the MESSENGER Gamma-Ray Spectrometer. *J. Geophys. Res.* 2012, 117, E12.

PROCKTER, L. M. et al. Evidence for Young Volcanism on Mercury from the Third MESSENGER Flyby. *Science.* 2010.

RAPPAPORT, N. J. et al. An Improved 360 Degree and Order Model of Venus Topography. *Icarus*. 1999, 139, 1, pp. 19 – 31.

RATCLIFF, J. T., SCHUBERT, G. and ZEBIB, A. Three-dimensional variable viscosity convection of an infinite Prandtl Number Boussinesq fluid in a spherical shell. *Geophys. Res. Lett.* 1995, 22, 16, pp. 2227–2230.

REDMOND, H. L. and KING, S. D. Does mantle convection currently exist on Mercury? *Phys. Earth Planet. In.* 2007, 164, 3–4, pp. 221 – 231.

REESE, C. C., SOLOMATOV, V. S. and MORESI, L.-N. Heat transport efficiency for stagnant lid convection with dislocation viscosity: Application to Mars and Venus. *J. Geophys. Res.* 1998, 103, E6, pp. 13643–13657.

REESE, C. C. et al. Stagnant lid convection in a spherical shell. *Phys. Earth Planet. Inter.* 1999, 116, pp. 1 – 7.

REESE, C. C., SOLOMATOV, V. S. and ORTH, C. P. Mechanisms for cessation of magmatic resurfacing on Venus. *J. Geophys. Res.* 2007, 112, E4.

RICARD, Y. and VIGNY, C. Mantle dynamics with induced plate tectonics. *J. Geophys. Res.* 1989, 94, B12, pp. 17543–17559.

RICARD, Y., VIGNY, C. and FROIDEVAUX, C. Mantle heterogeneities, geoid, and plate motion: A Monte Carlo inversion. *J. Geophys. Res.* 1989, 94, B10, pp. 13739–13754.

RICHARDS, M. A. et al. Role of a low-viscosity zone in stabilizing plate tectonics: Implications for comparative terrestrial planetology. *Geochem. Geophys. Geosyst.* 2001, 2.

RIVOLDINI, A. and van HOOLST, T. The interior structure of Mercury constrained by the low-degree gravity field and the rotation of Mercury. *Earth Planet. Sc. Lett.* 2013, 377–378, pp. 62 – 72.

SAMUEL, H. and TOSI, N. The influence of post-perovskite strength on the Earth's mantle thermal and chemical evolution. *Earth. Planet. Sc. Lett.* 2012, 323–324, pp. 50–59.

SCHUBERT, G. et al. Mercury's thermal history and the generation of its magnetic field. In VILAS, F., CHAPMAN, C. R. and MATTHEWS, M. S. (Ed.) *Mercury.* Tucson, Arizon: University of Arizona Press, 1988.

SCHUBERT, G. et al. Mantle convection and the thermal evolution of Venus. In BOUGHER, S. W., HUNTEN, D. M. and PHILLIPS, R. J. (Ed.) *Venus II - Geology, Geophysics, Atmosphere, and Solar Wind Environment.* Tucson, Arizon: University of Arizona Press, 1997. pp. 1245–1288.

SCHUBERT, G., TURCOTTE, D. L. and P., O. *Mantle Convection in the Earth and Planets.* New York : Cambridge Univ. Press, 2001.

SIMONS, M., HAGER, B. H. and SOLOMON, S. C. Global variations in the geoid/topography admittance of Venus. *Science.* 1994, 264, 5978, pp. 798 – 803.

SMITH, D. E. et al. Gravity Field and Internal Structure of Mercury from MESSENGER. *Science.* 2012, 336, 6078, pp. 214–217.

SMREKAR, S. E. et al. Recent Hotspot Volcanism on Venus from VIRTIS Emissivity Data. *Science.* 2010, 328, 5978, pp. 605 – 608.

SMREKAR, S. E. and PARMENTIER, E. M. The interaction of mantle plumes with surface thermal and chemical boundary layers: Applications to hotspots on Venus. *J. Geophys. Res.* 1996, 101, B3, pp. 5397 – 5410.

SMREKAR, S. E. and PHILLIPS, R. J. Venusian highlands: geoid to topography ratios and their implications. *Earth. Planet. Sc. Lett.* 1991, 107, 3–4, pp. 582 – 597.

SMREKAR, S. E. and SOTIN, C. Constraints on mantle plumes on Venus: Implications for volatile history. *Icarus.* 2012, 217, 2, pp. 510 – 523.

SOLOMATOV, V. S. and MORESI, L.-N. Stagnant lid convection on Venus. *J. Geophys. Res.* 1996, 101, pp. 4737–4753.

SOLOMATOV, V. S. and MORESI, L. N. Three regimes of mantle convection with non-Newtonian viscosity and stagnant lid convection on the terrestrial planets. *Geophys. Res. Lett.* 1997, 24, 15, pp. 1907 – 1910.

SOLOMATOV, V. S. and MORESI, L.-N. Scaling of time-dependent stagnant lid convection: Application to small-scale convection on Earth and other terrestrial planets. *J. Geophys. Res.* 2000, 105(B9), pp. 21795–21817.

SOLOMATOV, V. S. and MORESI, L.-N. Small-scale convection in the D$''$ layer. *J. Geophys. Res.* 2002, 107, B1, pp. ETG 3–1–ETG 3–10.

STEINBERGER, B., WERNER, S. C. and TORSVIK, T. H. Deep versus shallow origin of gravity anomalies, topography and volcanism on Earth, Venus and Mars. *Icarus.* 2010, 207, 2, pp. 564 – 577.

STEWART, S. T., LEINHARDT, Z. M. and HUMAYUN, M. Giant Impacts, Volatile Loss, and the K/Th Ratios on the Moon, Earth, and Mercury. *LPI Contributions.* March 2013, 1719, pp. 2306.

STOFAN, E. R. and SMREKAR, S. E. Large topographic rises, coronae, large flow fields, and large volcanoes on Venus: Evidence for mantle plumes? In FOULGER, G. and JURDY, D. (Ed.) *Plates, Plumes, and Planetary Processes.* Geological Society of America Special Paper 338, 2005. pp. 841–861.

STROM, R. G. Mercury: An overview. *Adv. Space Res.* 1997, 19, 10, pp. 1471 – 1485.

TACKLEY, P. J. Effects of strongly variable viscosity on three-dimensional compressible convection in planetary mantles. *J. Geophys. Res.* 1996, 101.

TACKLEY, P. J., NAKAGAWA, T. and HERNLUND, J. W. Influence of the Post-Perovskite Transition on Thermal an Thermo-Chemical Mantle Convection. In HIROSE, K. et al. (Ed.) *Post-perovskite: The Last Mantle Phase Transition.* AGU, 2007. pp. 229–247.

TATENO, S. et al. Determination of post-perovskite phase transition boundary up to 4400 K and implications for thermal structure in D$''$ layer. *Earth. Planet. Sc. Lett.* 2009, 277, 1–2, pp. 130–136.

TOSI, N. et al. Is the long-wavelength geoid sensitive to the presence of post-perovskite above the core-mantle boundary? *Geophys. Res. Lett.* 2009, 36, 5.

TOSI, N. et al. Thermochemical evolution of Mercury's interior. *J. Geophys. Res.* 2013, 118, 12, pp. 2474–2487.

TOSI, N. *Numerical modeling of present-day mantle convection.* PhD thesis, Charles University, Prague, 2007.

TOSI, N. Evolution and structure of Mercury's interior from MESSENGER observations. In *EGU General Assembly Conference Abstracts*, 17, 2015.

TOSI, N., YUEN, D. A. and ČADEK, O. Dynamical consequences in the lower mantle with the post-perovskite phase change and strongly depth-dependent thermodynamic and transport properties. *Earth. Planet. Sc. Lett.* 2010, 298, 1–2, pp. 229–243.

TSUCHIYA, T. et al. Phase transition in $MgSiO_3$ perovskite in the Earth's lower mantle. *Earth Planet. Sc. Lett.* 2004, 224, 3-4, pp. 241–248.

TURCOTTE, D. et al. Catastrophic Resurfacing and Episodic Subduction on Venus. *Icarus.* 1999, 139, 1, pp. 49 – 54.

van den BERG, A., RAINEY, E. G. and YUEN, D. The combined influences of variable thermal conductivity, temperature- and pressure-dependent viscosity and core–mantle coupling on thermal evolution. *Phys. Earth Planet. Inter.* 2005a, 149, 3–4, pp. 259 – 278.

van den BERG, A. P. and YUEN, D. A. Delayed cooling of the Earth's mantle due to variable thermal conductivity and the formation of a low conductivity zone. *Earth Planet. Sci. Lett.* 2002, 199, 3–4, pp. 403 – 413.

van den BERG, A. P., RAINEY, E. G. and YUEN, D. The combined influences of variable thermal conductivity, temperature- and pressure-dependent viscosity and core–mantle coupling on thermal evolution. *Phys. Earth Planet. In.* 2005b, 149, 3–4, pp. 259 – 278.

van den BERG, A. P. et al. Geodynamical modeling and multiscale seismic expression of thermo-chemical heterogeneity and phase transitions in the lowermost mantle. *Phys. Earth Planet. In.* 2010, 180, 3–4, pp. 244 – 257.

van der HILST, R. D. et al. Seismostratigraphy and thermal structure of Earth's core-mantle boundary region. *Science.* 2007, 315, 5820, pp. 1813–7.

van HOOLST, T. et al. Mercury's Interior Structure, Rotation, and Tides. *Space. Sci. Rev.* 2007, 132, 2-4, pp. 203–227.

van HUNEN, J. *Shallow and buoyant lithospheric subduction: causes and implications from thermo-chemical numerical modeling.* PhD thesis, Utrecht University, 2001.

van SCHMUS, W. R. Natural radioactivity of the crust and mantle. In AHRENS, T. J. (Ed.) *Global Earth Physics: A Handbook of Physical Constants.* AGU, 1995. pp. 283–291.

VARŠALOVIČ, D., MOSKALEV, A. and HERSONSKIJ, V. *Kvantovaja teoria uglovogo momenta.* Leningrad : Nauka, 1975.

VELÍMSKÝ, J. and FINLAY, C. C. Effect of a metallic core on transient geomagnetic induction. *Geochem. Geophys. Geosyst.* 2011, 12, 5.

VELÍMSKÝ, J. Electrical conductivity in the lower mantle: Constraints from CHAMP satellite data by time-domain EM induction modelling. *Phys. Earth Planet. In.* 2010, 180, 3–4, pp. 111 – 117.

VELÍMSKÝ, J., BENEŠOVÁ, N. and ČÍŽKOVÁ, H. On the detectability of 3-D postperovskite distribution in D" by electromagnetic induction. *Phys. Earth Planet. In.* 2012.

WEIDENSCHILLING, S. Iron/silicate fractionation and the origin of Mercury. *Icarus.* 1978, 35, 1, pp. 99 – 111.

WIECZOREK, M. 10.05 - Gravity and Topography of the Terrestrial Planets. In SCHUBERT, G. (Ed.) *Treatise on Geophysics.* 2007. pp. 165 – 206.

WOOD, B. J. Phase transformations and partitioning relations in peridotite under lower mantle conditions. *Earth. Planet. Sc. Lett.* 2000, 174, 3–4, pp. 341 – 354.

WRIGHT, G. B., FLYER, N. and YUEN, D. A. A hybrid radial basis function–pseudospectral method for thermal convection in a 3-D spherical shell. *Geochem. Geophys. Geosyst.* 2010, 11.

WYSESSION, M. E. et al. *The D'' Discontinuity and its Implications*, pp. 273–297. American Geophysical Union, 1998.

YOSHIDA, M. and KAGEYAMA, A. Application of the Yin-Yang grid to a thermal convection of a Boussinesq fluid with infinite Prandtl number in a three-dimensional spherical shell. *Geophys. Res. Lett.* 2004, 31.

YOSHIDA, M. and KAGEYAMA, A. Low-degree mantle convection with strongly temperature- and depth-dependent viscosity in a three-dimensional spherical shell. *J. Geophys. Res.* 2006, 111, B3.

YOSHINO, T. and YAMAZAKI, D. Grain growth kinetics of $CaIrO_3$ perovskite and post-perovskite, with implications for rheology of D'' layer. *Earth. Planet. Sc. Lett.* 2007, 255, 3–4, pp. 485–493.

YOUNG, D. M. *Iterative methods for solving partial difference equations of elliptic type.* PhD thesis, Harvard University, Cambridge, Mass, 1950.

ZHANG, S. and CHRISTENSEN, U. Some effects of lateral viscosity variations on geoid and surface velocities induced by density anomalies in the mantle. *Geophys. J. Int.* 1993, 114, 3, pp. 531–547.

ZHONG, S. et al. Role of temperature-dependent viscosity and surface plates in spherical shell models of mantle convection. *J. Geophys. Res.* 2000, 105, B5, pp. 11063–11082.

ZHONG, S. et al. A benchmark study on mantle convection in a 3-D spherical shell using CitcomS. *Geochem. Geophys. Geosyst.* 2008, 9.

ZUBER, M. T. et al. Topography of the Northern Hemisphere of Mercury from MESSENGER Laser Altimetry. *Science.* 2012, 336, 6078, pp. 217–220.

List of Tables

List of Abbreviations

RHS	right-hand side
LHS	left-hand side
CMB	core-mantle boundary
GTR	geoid-to-topography ratio
LHDAC	laser-heated diamond anvil cell
EM	electromagnetic
PV	perovskite
PPV	post-perovskite

A. Definition of the Spherical Harmonic Functions and Some Selected Operations with Them

In this appendix, we summarize the basics of spherical harmonic function formalism: definitions, basic characteristics and common operations with harmonic functions. After that, we present spherical harmonic expansion of the equations that govern mantle convection. More detailed explanation of spherical harmonic functions can be found in literature (e.g. Varšalovič et al., 1975).

A.1 Definitions

Scalar, vector or tensor functions can be expressed in terms of series of spherical harmonic functions (respectively):

$$f(r,\vartheta,\varphi) = \sum_{j=0}^{\infty} \sum_{m=-j}^{j} f_{jm}(r) Y_{jm}(\vartheta,\varphi), \tag{A.1a}$$

$$\boldsymbol{v}(r,\vartheta,\varphi) = \sum_{j=0}^{\infty} \sum_{m=-j}^{j} \sum_{l=|j-1|}^{j+1} v^{l}_{jm}(r) \mathbf{Y}^{l}_{jm}(\vartheta,\varphi), \tag{A.1b}$$

$$\tau(r,\vartheta,\varphi) = \sum_{j=0}^{\infty} \sum_{m=-j}^{j} \sum_{k=0}^{2} \sum_{l=|j-k|}^{j+k} \tau^{lk}_{jm}(r) \boldsymbol{Y}^{lk}_{jm}(\vartheta,\varphi), \tag{A.1c}$$

where $Y_{jm}(\vartheta,\varphi), \boldsymbol{Y}^{l}_{jm}(\vartheta,\varphi)$ and $\boldsymbol{Y}^{lk}_{jm}(\vartheta,\varphi)$ are scalar, vector and tensor spherical harmonic functions which are defined as follows:

$$Y_{jm}(\vartheta,\varphi) = \begin{cases} P_{jm}(\cos\vartheta) e^{im\varphi} & \text{for } m \geq 0, \\ (-1)^m Y^{*}_{j|m|}(\vartheta,\varphi) & \text{for } m < 0, \end{cases} \tag{A.2a}$$

$$\mathbf{Y}^{l}_{jm}(\vartheta,\varphi) = \sum_{\mu=-1}^{1} \sum_{\nu=-l}^{l} C^{jm}_{l\nu 1\mu} Y_{l\nu}(\vartheta,\varphi) \boldsymbol{e}_{\mu}, \tag{A.2b}$$

$$\mathbf{Y}^{lk}_{jm}(\vartheta,\varphi) = \sum_{\mu=-l}^{l} \sum_{\nu=-k}^{k} C^{jm}_{l\mu k\nu} Y_{l\mu}(\vartheta,\varphi) \boldsymbol{e}_{k\nu}, \tag{A.2c}$$

where $P_{jm}(\cos\vartheta)$ are associated Legendre polynomials, * denotes complex conjugation and $C^{jm}_{j_1 m_1 j_2 m_2}$ are Clebsch-Gordan coefficients and $\boldsymbol{e}_{\mu}$ in equation (A.2b) are cyclic covariant base vectors

$$
\begin{aligned}
\boldsymbol{e}_1 &= -\frac{1}{\sqrt{2}}(\boldsymbol{e}_x + i\boldsymbol{e}_y) = -\frac{1}{\sqrt{2}}(\boldsymbol{e}_r \sin\vartheta + \boldsymbol{e}_\vartheta \cos\vartheta + i\boldsymbol{e}_\varphi)e^{i\varphi}, \\
\boldsymbol{e}_0 &= \boldsymbol{e}_z = \boldsymbol{e}_r \cos\vartheta - \boldsymbol{e}_\vartheta \sin\vartheta, \\
\boldsymbol{e}_{-1} &= \frac{1}{\sqrt{2}}(\boldsymbol{e}_x - i\boldsymbol{e}_y) = \frac{1}{\sqrt{2}}(\boldsymbol{e}_r \sin\vartheta + \boldsymbol{e}_\vartheta \cos\vartheta - i\boldsymbol{e}_\varphi)e^{-i\varphi},
\end{aligned}
\tag{A.3}
$$

where $\boldsymbol{e}_x, \boldsymbol{e}_y$ and $\boldsymbol{e}_z$ are Cartesian unit vectors and $\boldsymbol{e}_r, \boldsymbol{e}_\vartheta$ and $\boldsymbol{e}_\varphi$ are unit vectors in the spherical coordinate system.
Tensor base $\boldsymbol{e}_{k\nu}$ is defined as

$$
\boldsymbol{e}_{k\nu} = \sum_{\xi=-1}^{1} \sum_{\lambda=-1}^{1} C^{k\nu}_{1\xi1\lambda} \boldsymbol{e}_\xi \boldsymbol{e}_\lambda. \tag{A.4}
$$

Spherical harmonic functions (A.2a)–(A.2c) are orthonormal over the unit sphere. Orthonormality implies following relations for spherical harmonic coefficients:

$$
f_{jm}(r) = \int_0^\pi \int_0^{2\pi} f(r,\vartheta,\varphi) Y^*_{jm}(\vartheta,\varphi) \sin\vartheta \, \mathrm{d}\varphi \, \mathrm{d}\vartheta, \tag{A.5a}
$$

$$
v^l_{jm}(r) = \int_0^\pi \int_0^{2\pi} \boldsymbol{v}(r,\vartheta,\varphi) \boldsymbol{Y}^{l*}_{jm}(\vartheta,\varphi) \sin\vartheta \, \mathrm{d}\varphi \, \mathrm{d}\vartheta, \tag{A.5b}
$$

$$
\tau^{lk}_{jm}(r) = \int_0^\pi \int_0^{2\pi} \tau(r,\vartheta,\varphi) \boldsymbol{Y}^{lk\,+}_{jm}(\vartheta,\varphi) \sin\vartheta \, \mathrm{d}\varphi \, \mathrm{d}\vartheta, \tag{A.5c}
$$

where + denotes complex conjugation and transposition.

Theoretically, equations (A.1a)-(A.1c) give exact representations of the functions $f(r,\vartheta,\varphi)$, $\boldsymbol{v}(r,\vartheta,\varphi)$, and $\tau(r,\vartheta,\varphi)$. In real numerical applications, it is unavoidable to set up a cut-off degree j_{max} instead of the infinite series. Index j is called the degree of spherical harmonic function and index m is the order. Order m ranges from $-j$ to j and such coefficients can approximate a complex function, while a real function can be described by a set of coefficients for $m = 0, \ldots, j$. Generally, harmonic coefficients are complex numbers. For an axisymmetric function, only the coefficients with $m = 0$ are non-zero. These harmonic coefficients are real numbers. Vector harmonic coefficients with indices $l = j \pm 1$ describe poloidal part of the field, index $l = j$ indicates toroidal part. For tensor harmonic coefficients, those with $l = j, j \pm 2$ describe poloidal part and $l = j \pm 1$ is for toroidal part. Moreover, meaning of the index k is that it is 0 for the tensor trace,

$k = 1$ for the antisymmetric part and $k = 2$ denotes the deviatoric part of the tensor. A symmetric stress tensor can be expressed only by harmonic coefficients with $k = 0$ (pressure) and $k = 2$ (deviatoric part).

The power spectrum S is often used as a characteristic of function f and is defined as a function of harmonic degree j:

$$S(j, r) = \sum_{m=-j}^{j} f_{jm} f_{jm}^{*}(r). \tag{A.6}$$

A.2 Operations with spherical harmonic functions

From now on, we will not explicitly specify spatial coordinates.

A.2.1 Differential operators acting on spherical tensors

$$\nabla f_{jm} Y_{jm} = \frac{1}{\sqrt{2j+1}} \left[\sqrt{j} \left(\frac{d}{dr} + \frac{j+1}{r} \right) f_{jm} \mathbf{Y}_{jm}^{j-1} - \sqrt{j+1} \left(\frac{d}{dr} - \frac{j}{r} \right) f_{jm} \boldsymbol{Y}_{jm}^{j+1} \right] \tag{A.7}$$

$$\nabla f_{jm}^{l} \boldsymbol{Y}_{jm}^{l} = (-1)^{j+l+1} \sum_{k} \sqrt{2k+1} \sqrt{l} \begin{Bmatrix} 1 & 1 & k \\ j & l-1 & l \end{Bmatrix} \left(\frac{d}{dr} + \frac{l+1}{r} \right) f_{jm}^{l} \boldsymbol{Y}_{jm}^{l-1,k} + \tag{A.8}$$

$$+ (-1)^{j+l} \sum_{k} \sqrt{2k+1} \sqrt{l+1} \begin{Bmatrix} 1 & 1 & k \\ j & l+1 & l \end{Bmatrix} \left(\frac{d}{dr} - \frac{l}{r} \right) f_{jm}^{l} \boldsymbol{Y}_{jm}^{l+1,k}$$

$$\nabla \cdot f_{jm}^{l} \mathbf{Y}_{jm}^{l} = \frac{1}{\sqrt{2j+1}} \left[\sqrt{j} \left(\frac{d}{dr} - \frac{j-1}{r} \right) f_{jm}^{j-1} - \left(\frac{d}{dr} + \frac{j+2}{r} \right) f_{jm}^{j+1} \right] Y_{jm} \tag{A.9}$$

$$\nabla \cdot f_{jm}^{lk} \mathbf{Y}_{jm}^{lk} = (-1)^{j+l} \sqrt{2k+1} \left[\sqrt{l+1} \begin{Bmatrix} 1 & l & l+1 \\ j & 1 & k \end{Bmatrix} \left(\frac{d}{dr} - \frac{l}{r} \right) f_{jm}^{lk} \mathbf{Y}_{jm}^{l+1} - \right. \tag{A.10}$$

$$\left. - \sqrt{l} \begin{Bmatrix} 1 & l & l-1 \\ j & 1 & k \end{Bmatrix} \left(\frac{d}{dr} + \frac{l+1}{r} \right) f_{jm}^{lk} \mathbf{Y}_{jm}^{l-1} \right]$$

A.2.2 Products of spherical harmonic functions

$$Y_{j_1m_1}Y_{j_2m_2} = \frac{\Pi_{j_1j_2}}{\sqrt{4\pi}}\sum_{jm}\frac{1}{\Pi_j}C^{j0}_{j_10j_20}C^{jm}_{j_1m_1j_2m_2}Y_{jm} \tag{A.11}$$

$$Y_{j_1m_1}\boldsymbol{Y}^{l_2k_2}_{j_2m_2} = \frac{\Pi_{j_1j_2l_2}}{\sqrt{4\pi}}\sum_{jml}(-1)^{k_2+l+j}C^{l0}_{j_10l_20}C^{jm}_{j_1m_1j_2m_2}\left\{\begin{matrix} l_2 & k_2 & j_2 \\ j & j_1 & l \end{matrix}\right\}\boldsymbol{Y}^{lk_2}_{jm} \tag{A.12}$$

$$\boldsymbol{Y}^{l_1}_{j_1m_1}\cdot\boldsymbol{Y}^{l_2}_{j_2m_2} = (-1)^{j_2+l_2}\frac{\Pi_{j_1j_2l_1l_2}}{\sqrt{4\pi}}\sum_{jm}\frac{1}{\Pi_j}C^{j0}_{l_10l_20}C^{jm}_{j_1m_1j_2m_2}\left\{\begin{matrix} j_1 & j_2 & j \\ l_2 & l_1 & 1 \end{matrix}\right\}Y_{jm} \tag{A.13}$$

$$\boldsymbol{Y}^{l_1}_{j_1m_1}\cdot\boldsymbol{Y}^{l_2k_2}_{j_2m_2} = (-1)^{k_2+1}\frac{\prod_{j_1j_2l_1l_2k_2}}{\sqrt{4\pi}}\sum_{jml}C^{l0}_{l_10l_20}C^{jm}_{j_1m_1j_2m_2}\left\{\begin{matrix} j & j_1 & j_2 \\ l & l_1 & l_2 \\ 1 & 1 & k_2 \end{matrix}\right\}\boldsymbol{Y}^{l}_{jm} \tag{A.14}$$

$$\boldsymbol{Y}^{l_1k_1}_{j_1m_1}:\boldsymbol{Y}^{l_2k_2}_{j_2m_2} = \delta_{k_1k_2}(-1)^{j_2+l_2}\frac{\Pi_{j_1j_2l_1l_2}}{\sqrt{4\pi}}\sum_{jm}\frac{1}{\Pi_j}C^{j0}_{l_10l_20}C^{jm}_{j_1m_1j_2m_2}\left\{\begin{matrix} k_1 & l_1 & j_1 \\ j & j_2 & l_2 \end{matrix}\right\}Y_{jm} \tag{A.15}$$

where $\prod_{j_1j_2\ldots} = \sqrt{2j_1+1}\sqrt{2j_2+1}\ldots$, $\left\{\begin{matrix} a & b & c \\ d & e & f \end{matrix}\right\}$ is Wigner 6-j symbol and $\left\{\begin{matrix} a & b & c \\ d & e & f \\ g & h & i \end{matrix}\right\}$ is Wigner's 9-j symbol.

A.2.3 Clebsch-Gordan coefficients, 6-j and 9-j Wigner symbols

While manipulating with structural harmonic expansions of governing equations we need to use basic characteristics of Clebsch-Gordan coefficients and 6-j and 9-j Wigner symbols. Here, we give only brief overview. More (particularly the exact values for special choices of indices) can be found in literature (Varšalovič et al., 1975).

Symmetry of Clebsch-Gordan coefficients

$$C^{jm}_{j_1m_1j_2m_2} = (-1)^{j+j_1+j_2}\,C^{j-m}_{j_1m_1j_2-m_2},$$
$$C^{jm}_{j_1m_1j_2m_2} = (-1)^{j+j_1+j_2}\,C^{jm}_{j_2m_2j_1m_1}.$$

Indices of Clebsch-Gordan coefficients are bound together by two relations:

$$|j_1 - j_2| \leq j \leq j_1 + j_2 \quad \text{along with} \quad m_1 + m_2 = m.$$

Values for special choices of indices

$$\begin{aligned} C^{j0}_{j_1 0 j_2 0} &= 0 \quad \text{ if } j_1 + j_2 + j_3 \text{ is odd,} \\ C^{jm}_{jm00} &= 1. \end{aligned}$$

Symmetry of Wigner 6-j symbols: it is possible to switch any two columns:

$$\begin{Bmatrix} a & b & c \\ d & e & f \end{Bmatrix} = \begin{Bmatrix} a & c & b \\ d & f & e \end{Bmatrix} \quad \text{etc.}$$

switch rows in two columns, while third remain fixed:

$$\begin{Bmatrix} a & b & c \\ d & e & f \end{Bmatrix} = \begin{Bmatrix} a & e & f \\ d & b & c \end{Bmatrix} \quad \text{etc.}$$

Special value for $f = 0$

$$\begin{Bmatrix} a & b & c \\ d & e & 0 \end{Bmatrix} = \frac{(-1)^{a+b+c}}{\Pi_{ab}} \delta_{ae} \delta_{bd}$$

Symmetry of Wigner 9-j symbols, permute columns:

$$\begin{Bmatrix} a & b & c \\ d & e & f \\ g & h & i \end{Bmatrix} = \begin{Bmatrix} b & c & a \\ e & f & d \\ h & i & g \end{Bmatrix} \quad \text{etc.}$$

switch two columns and two rows:

$$\begin{Bmatrix} a & b & c \\ d & e & f \\ g & h & i \end{Bmatrix} = \begin{Bmatrix} d & f & e \\ a & c & b \\ g & i & h \end{Bmatrix} \quad \text{etc.}$$

Value of 9-j symbol for a special choice of indices:

$$\begin{Bmatrix} 0 & a & a \\ b & c & d \\ b & e & f \end{Bmatrix} = \frac{(-1)^{a+b+d+e}}{\Pi_{ab}} \begin{Bmatrix} f & d & a \\ c & e & b \end{Bmatrix}.$$

A.3 Stokes' problem for radially symmetric viscosity in spherical harmonic formalism

Using definitions (A.1a)–(A.1c) and some operations from the preceding paragraph, the Stokes' problem (eqs. (1.1), (1.2) and (1.5)) with boundary conditions (1.7) and (1.8) can be written in the following form (Klika, 1995):
Equation of continuity:

$$\sqrt{j}\left(\frac{d}{dr}-\frac{j-1}{r}\right)v_{jm}^{j-1}-\sqrt{j+1}\left(\frac{d}{dr}+\frac{j+2}{r}\right)v_{jm}^{j+1}=0, \tag{A.16}$$

momentum equation (here f represents the buoyancy force $\Delta\varrho g$):

$$\begin{aligned}-f_{jm}^{j-1}=&-\sqrt{\frac{j}{3(2j+1)}}\left(\frac{d}{dr}+\frac{j+1}{r}\right)\tau_{jm}^{j0}+\sqrt{\frac{j-1}{2j-1}}\left(\frac{d}{dr}-\frac{j-2}{r}\right)\tau_{jm}^{j-2,2}-\\&-\sqrt{\frac{(j+1)(2j+3)}{6(2j-1)(2j+1)}}\left(\frac{d}{dr}+\frac{j+1}{r}\right)\tau_{jm}^{j2},\end{aligned} \tag{A.17}$$

$$\begin{aligned}-f_{jm}^{j+1}=&-\sqrt{\frac{j+1}{3(2j+1)}}\left(\frac{d}{dr}-\frac{j}{r}\right)\tau_{jm}^{j0}-\sqrt{\frac{j+2}{2j+3}}\left(\frac{d}{dr}+\frac{j+3}{r}\right)\tau_{jm}^{j+2,2}+\\&+\sqrt{\frac{j(2j-1)}{6(2j+3)(2j+1)}}\left(\frac{d}{dr}-\frac{j}{r}\right)\tau_{jm}^{j2}\end{aligned} \tag{A.18}$$

and rheology equation:

$$\tau_{jm}^{j+2,2}+2\eta\sqrt{\frac{j+2}{2j+3}}\left(\frac{d}{dr}-\frac{j+1}{r}\right)v_{jm}^{j+1} = 0, \tag{A.19}$$

$$\tau_{jm}^{j-2,2}-2\eta\sqrt{\frac{j-1}{2j-1}}\left(\frac{d}{dr}+\frac{j}{r}\right)v_{jm}^{j-1} = 0, \tag{A.20}$$

$$\begin{aligned}\tau_{jm}^{j2}&+2\eta\sqrt{\frac{(j+1)(2j+3)}{6(2j-1)(2j+1)}}\left(\frac{d}{dr}-\frac{j-1}{r}\right)v_{jm}^{j-1}-\\&-2\eta\sqrt{\frac{j(2j-1)}{6(2j+3)(2j+1)}}\left(\frac{d}{dr}+\frac{j+2}{r}\right)v_{jm}^{j+1}=0.\end{aligned} \tag{A.21}$$

Boundary conditions yield:

$$\sqrt{j}\ v_{jm}^{j-1} - \sqrt{j+1}\ v_{jm}^{j+1} = 0, \tag{A.22}$$

$$\sqrt{\frac{(j+1)(j-1)}{(2j+1)(2j-1)}}\tau_{jm}^{j-2,2} - \sqrt{\frac{j(j+2)}{(2j+3)(2j+1)}}\tau_{jm}^{j+2,2} - \\ - \sqrt{\frac{3}{2(2j-1)(2j+3)}}\tau_{jm}^{j2} = 0. \tag{A.23}$$

The equations above involve only coefficients τ_{jm}^{j0}, τ_{jm}^{j2}, $\tau_{jm}^{j\pm2,2}$ and $v_{jm}^{j\pm1}$ and thus describe only poloidal part of the flow. It can be shown that the toroidal part of the flow induced by buoyancy forces in the case of material with spherically symmetric rheology is zero (Ricard and Vigny, 1989). Moreover, it can be shown that in the case of axisymmetric flow, the toroidal part of the solution is zero even for laterally-dependent viscosity (Klika, 1995; Tosi, 2007). Thus, the coefficients $\tau_{jm}^{j\pm1}$ and v_{jm}^{j} are zero in all cases assumed in this work.

A.4 Evaluation of non-linear terms on the grid

While solving governing equations (1.1)-(1.6) we need to treat several non-linear terms. One arises from the rheology equation in the case of laterally dependent viscosity ($\eta\nabla\boldsymbol{v}$), others are present in the energy equation, namely in advection ($\boldsymbol{v}\cdot\nabla T$), adiabatic heating ($v_r T$), viscous dissipation ($\sigma : \nabla\boldsymbol{v}$) and latent heat ($T\ \boldsymbol{v}\cdot\nabla\Gamma$) term. We need to evaluate different products of scalars, vectors and tensors, where the result of such a product is either tensor (term $\eta\nabla\boldsymbol{v}$) or scalar (other terms). As discussed in section 1.2, the evaluation of those non-linear terms in the spectral domain is inefficient, we thus evaluate these terms on the spatial grid here. This process consists of three steps: 1. evaluation of functions in the predefined grid points (evaluation of spherical components of vectors and tensors), 2. evaluation of products on the grid, 3. harmonic analysis to obtain spherical harmonic coefficients of the resulting products. Following sections contain formulas needed to perform steps 1 and 3 and brief description of their derivation (step 2 is trivial).

A.4.1 Step 1 — evaluation of spherical components of vectors and tensors

As a first step in a process of evaluation of spherical components of vectors and tensors, we derive formulas for spherical unit vectors $\boldsymbol{e}_r$, $\boldsymbol{e}_\vartheta$ and $\boldsymbol{e}_\varphi$. Then we use these formulas to derive the spherical components of a vector and finally we give formulas for the spherical components of a tensor.

A.4.1.1 Derivation of unit vectors $\boldsymbol{e}_r$, $\boldsymbol{e}_\vartheta$ and $\boldsymbol{e}_\varphi$

To derive vectors $\boldsymbol{e}_r$, $\boldsymbol{e}_\vartheta$ and $\boldsymbol{e}_\varphi$, we start from an alternative definition of spherical harmonic functions based on spherical base vectors. The following relationship applies:

$$\boldsymbol{Y}^{(\lambda)}_{jm} = \left[\boldsymbol{Y}^{(\lambda)}_{jm}\right]_r \boldsymbol{e}_r + \left[\boldsymbol{Y}^{(\lambda)}_{jm}\right]_\vartheta \boldsymbol{e}_\vartheta + \left[\boldsymbol{Y}^{(\lambda)}_{jm}\right]_\varphi \boldsymbol{e}_\varphi. \tag{A.24}$$

Functions $\boldsymbol{Y}^{(\lambda)}_{jm}$ are linear combinations of vector harmonic functions $\boldsymbol{Y}^{l}_{jm}$:

$$\boldsymbol{Y}^{(1)}_{jm} = \sqrt{\frac{j+1}{2j+1}}\boldsymbol{Y}^{j-1}_{jm} + \sqrt{\frac{j}{2j+1}}\boldsymbol{Y}^{j+1}_{jm}, \tag{A.25a}$$

$$\boldsymbol{Y}^{(0)}_{jm} = \boldsymbol{Y}^{j}_{jm}, \tag{A.25b}$$

$$\boldsymbol{Y}^{(-1)}_{jm} = \sqrt{\frac{j}{2j+1}}\boldsymbol{Y}^{j-1}_{jm} - \sqrt{\frac{j+1}{2j+1}}\boldsymbol{Y}^{j+1}_{jm}. \tag{A.25c}$$

Components $\left[\boldsymbol{Y}^{(\lambda)}_{jm}\right]_r$, $\left[\boldsymbol{Y}^{(\lambda)}_{jm}\right]_\vartheta$ and $\left[\boldsymbol{Y}^{(\lambda)}_{jm}\right]_\varphi$ are as follows:

	$\left[\boldsymbol{Y}^{(\lambda)}_{jm}\right]_r$	$\left[\boldsymbol{Y}^{(\lambda)}_{jm}\right]_\vartheta$	$\left[\boldsymbol{Y}^{(\lambda)}_{jm}\right]_\varphi$
$\lambda = 1$	0	$Ae^{-i\varphi}Y_{jm+1} - Be^{i\varphi}Y_{jm-1}$	$iC\frac{1}{\sin\vartheta}Y_{jm}$
$\lambda = 0$	0	$-C\frac{1}{\sin\vartheta}Y_{jm}$	$-iAe^{-i\varphi}Y_{jm+1} + iBe^{i\varphi}Y_{jm-1}$
$\lambda = -1$	Y_{jm}	0	0

where $A = \frac{1}{2}\sqrt{\frac{(j-m)(j+m+1)}{j(j+1)}}$, $B = \frac{1}{2}\sqrt{\frac{(j+m)(j-m+1)}{j(j+1)}}$ and $C = \frac{m}{\sqrt{j(j+1)}}$.

The vector $\boldsymbol{e}_r$ can be obtained from eq. (A.24) for $\lambda = -1$, $j = 0$ and $m = 0$. Using identity $Y_{00} = \frac{1}{\sqrt{4\pi}}$ we will get:

$$\boldsymbol{e}_r = -\sqrt{4\pi}\boldsymbol{Y}^{1}_{00}. \tag{A.26}$$

Similarly vector $\boldsymbol{e}_\vartheta$ was obtained from eq. (A.24) for $\lambda = 1$, $j = 1$ and $m = 0$, moreover replace $Y_{11} = -\frac{1}{2}\sqrt{\frac{3}{2\pi}}\sin\vartheta e^{i\varphi}$ and then

$$\boldsymbol{e}_{\boldsymbol{\vartheta}} = -\frac{2\sqrt{2\pi}}{3\sin\vartheta}(\sqrt{2}\boldsymbol{Y}^0_{10} + \boldsymbol{Y}^2_{10}). \tag{A.27}$$

Finally, $\boldsymbol{e}_\varphi$ is obtained for $\lambda = 0$, $j = 1$ and $m = 0$, using the above identities we get:

$$\boldsymbol{e}_{\boldsymbol{\varphi}} = -\frac{2i\sqrt{2\pi}}{\sqrt{3}\sin\vartheta}\boldsymbol{Y}^1_{10}. \tag{A.28}$$

A.4.1.2 Spherical components of vector

Here, we derive spherical components of a vector by multiplying a vector by unit vector:

$$\begin{aligned}
\boldsymbol{e}_r \cdot \boldsymbol{v} &= -\sqrt{4\pi}\sum_{jml} v^l_{jm}\boldsymbol{Y}^1_{00} \cdot \boldsymbol{Y}^l_{jm}, \\
\boldsymbol{e}_\vartheta \cdot \boldsymbol{v} &= -\frac{2\sqrt{2\pi}}{3\sin\vartheta}\sum_{jml} v^l_{jm}(\sqrt{2}\boldsymbol{Y}^0_{10} + \boldsymbol{Y}^2_{10}) \cdot \boldsymbol{Y}^l_{jm}, \\
\boldsymbol{e}_\varphi \cdot \boldsymbol{v} &= -\frac{2i\sqrt{2\pi}}{\sqrt{3}\sin\vartheta}\sum_{jml} v^l_{jm}\boldsymbol{Y}^1_{10} \cdot \boldsymbol{Y}^l_{jm},
\end{aligned}$$

Using the relation (A.13) for scalar product of two vector harmonics, we can evaluate the spherical components of vector as:

$$\begin{aligned}
v_r &= \sum_{jml}\sqrt{\frac{2l+1}{2j+1}} C^{j0}_{l010} v^l_{jm} Y_{jm}, \\
v_\vartheta &= \frac{\sqrt{2(2j+1)}}{3\sin\vartheta}\sum_{jml} v^l_{jm}\left[\sqrt{\frac{2}{2l+1}} C^{lm}_{jm10} Y_{lm} + \right. \\
&\quad \left. + \sqrt{15(2l+1)}\sum_{J=j-1}^{j+1} C^{J0}_{l020} C^{Jm}_{jm10}\begin{Bmatrix} j & 1 & J \\ 2 & l & 1 \end{Bmatrix} Y_{Jm}\right] \\
v_\varphi &= -\sum_{jml} v^l_{jm}\frac{\sqrt{6}i}{\sin\vartheta}\prod_{jl}\sum_{J=l\pm1}\frac{1}{\sqrt{2J+1}} C^{J0}_{l010} C^{Jm}_{jm10}\begin{Bmatrix} j & 1 & J \\ 1 & l & 1 \end{Bmatrix} Y_{Jm}
\end{aligned}$$

A.4.1.3 Spherical components of a tensor

As the stress tensor is symmetric, it has only 6 independent components: τ_{rr}, $\tau_{r\vartheta}$, $\tau_{r\varphi}$, $\tau_{\vartheta\vartheta}$, $\tau_{\vartheta\varphi}$ and $\tau_{\varphi\varphi}$. We need to evaluate the spherical components of stress deviator ($\tau = \sum_{jml}\tau^{l2}_{jm}\boldsymbol{Y}^{l2}_{jm}$) which has zero trace. This further reduces the number of independent components ($-\tau_{\varphi\varphi} = \tau_{rr} + \tau_{\vartheta\vartheta}$). Moreover, in the axisymmetric case, the components $\tau_{r\varphi}$ and $\tau_{\vartheta\varphi}$ are zero which leaves us with three independent components τ_{rr}, $\tau_{\vartheta\vartheta}$, $\tau_{r\vartheta}$.

To obtain a component of a tensor, it is necessary to multiply the tensor by two unit vectors (e.g. $\tau_{r\vartheta} = \boldsymbol{e}_r \cdot \tau \cdot \boldsymbol{e}_\vartheta$). First, let us evaluate products $\boldsymbol{e}_r \cdot \tau$ and $\boldsymbol{e}_\vartheta \cdot \tau$. Combining the relation for dot product of a vector and a tensor (A.14) with equations (A.26, A.27) and then using the properties of Clebsch-Gordan coefficients, 6-j and 9-j symbols leads to expressions:

$$\boldsymbol{e}_r \cdot \tau = \sum_{jml} \tau^{l2}_{jm} (-1)^{j+l} \sqrt{5(2l+1)} \sum_{L=l\pm1} C^{L0}_{l010} \begin{Bmatrix} 1 & L & j \\ l & 2 & 1 \end{Bmatrix} \boldsymbol{Y}^{L}_{jm},$$

$$\begin{aligned} \boldsymbol{e}_\vartheta \cdot \tau = & -\frac{\sqrt{10}}{3\sin\vartheta} \sum_{jlm} \sqrt{2j+1}\, \tau^{l2}_{jm} \sum_{J=|j-1|}^{j+1} \left[\sqrt{2} C^{Jm}_{jm10} \begin{Bmatrix} J & 1 & l \\ 2 & j & 1 \end{Bmatrix} \boldsymbol{Y}^{l}_{Jm} + \right. \\ & \left. + \sqrt{15(2l+1)} \sum_{L=|l-2|,l,l+2} C^{L0}_{l020} C^{Jm}_{jm10} \begin{Bmatrix} J & 1 & j \\ L & 2 & l \\ 1 & 1 & 2 \end{Bmatrix} \boldsymbol{Y}^{L}_{Jm} \right]. \end{aligned}$$

Then, by another multiplication of unit vectors and using the same procedure as for the derivation of vector components, the following relations can be obtained:

$$\tau_{rr} = \sum_{jml} \tau^{l2}_{jm} \sqrt{\frac{5(2l+1)}{(2j+1)}} \sum_{L=l\pm1} C^{L0}_{l010} \begin{Bmatrix} 1 & L & j \\ l & 2 & 1 \end{Bmatrix} \sqrt{2L+1} C^{j0}_{L010} Y_{jm}$$

$$\begin{aligned} \tau_{r\vartheta} = & \sum_{jml} \tau^{l2}_{jm} \frac{\sqrt{10 \prod_{lj}}}{3\sin\vartheta} \sum_{L=l\pm1} C^{L0}_{l010} \begin{Bmatrix} L & 1 & j \\ 2 & l & 1 \end{Bmatrix} \left[\sqrt{\frac{2}{2L+1}} C^{Lm}_{jm10} Y_{Lm} + \right. \\ & \left. + \sqrt{15(2L+1)} \sum_{J=|j-1|}^{j+1} \frac{1}{\sqrt{2J+1}} C^{J0}_{L020} C^{Jm}_{jm10} \begin{Bmatrix} j & 1 & J \\ 2 & L & 1 \end{Bmatrix} Y_{Jm} \right] \end{aligned}$$

$$\tau_{\vartheta\vartheta} =$$

$$\frac{\sqrt{20}}{9\sin^2\vartheta}\sum_{jl}\tau^{l2}_{jm}\sqrt{2j+1}\Bigg[\sum_{J=|j-1|}^{j+1} C^{Jm}_{jm10}\left\{\begin{array}{ccc} J & 1 & l \\ 2 & j & 1 \end{array}\right\}\sqrt{2J+1}\Bigg(\sqrt{\frac{2}{2l+1}}C^{lm}_{Jm10}Y_{lm}+$$

$$+\ \sqrt{15(2l+1)}\sum_{\gamma=|J-1|}^{J+1}\frac{1}{\sqrt{2\gamma+1}}C^{\gamma 0}_{l020}C^{\gamma m}_{Jm10}\left\{\begin{array}{ccc} J & 1 & \gamma \\ 2 & l & 1 \end{array}\right\}Y_{\gamma m}\Bigg)+$$

$$+\sqrt{15}\prod_{lJ}\sum_{J=|j-1|}^{j+1}\sum_{L=|l-2|}^{l+2}C^{L0}_{l020}C^{Jm}_{jm10}\left\{\begin{array}{ccc} J & 1 & j \\ L & 2 & l \\ 1 & 1 & 2 \end{array}\right\}\Bigg(\sqrt{\frac{2}{2L+1}}C^{Lm}_{Jm10}(-1)^{L+J+1}Y_{Lm}+$$

$$+\ \sqrt{15(2L+1)}\sum_{\gamma=|J-1|}^{J+1}\frac{1}{\sqrt{2\gamma+1}}C^{\gamma 0}_{L020}C^{\gamma m}_{Jm10}\left\{\begin{array}{ccc} J & 1 & \gamma \\ 2 & L & 1 \end{array}\right\}Y_{\gamma m}\Bigg)\Bigg]$$

A.4.2 Step 3 — Harmonic analysis

After evaluating the products on the grid we have to perform spherical harmonic analysis of these products. In the case of the products arising from energy equation ($\boldsymbol{v}\cdot\nabla T$, $v_r T$, $\sigma : \nabla\boldsymbol{v}$ and $T\ \boldsymbol{v}\cdot\nabla\Gamma$), the result is scalar and its analysis is a simple operation (A.5a). In the case of the rheology equation, the situation is more complex. We evaluate a product $\eta\nabla\boldsymbol{v}$ which is a tensor. We start from (A.5c), where tensor harmonic functions are given by (A.2c). For our axisymmetric problem order $m = 0$ and $k = 2$ (deviatoric stress) the relation (A.2c) is as follows:

$$\boldsymbol{Y}^{l2+}_{j0} = \sum_{\mu=-l}^{l}\sum_{\nu=-2}^{2} C^{j0}_{l\mu 2\nu}\left(Y_{l\mu}\boldsymbol{e}^T_{2\nu}\right)^* . \tag{A.31}$$

Base vector $\boldsymbol{e}^T_{2\nu}$ is then expanded to a set of products of Clebsch-Gordan coefficients and cyclic covariant base vectors following equation (A.4). Using equations (A.3) those products can be evaluated. Products are then substituted into (A.31). Finally, coefficients of stress yield:

$$
\begin{aligned}
\tau_{j0}^{l2} = 2\pi \int\limits_0^\pi \big\{ & P_{l2} C_{l22-2}^{j0} (\tau_{rr} \sin^2\vartheta + \tau_{r\vartheta} \sin 2\vartheta + \tau_{\vartheta\vartheta} \cos^2\vartheta - \tau_{\varphi\varphi}) + \\
& + 2 P_{l1} C_{l12-1}^{j0} (\tau_{rr} \sin\vartheta \cos\vartheta + \tau_{r\vartheta} \cos 2\vartheta - \tau_{\vartheta\vartheta} \sin\vartheta \cos\vartheta) + \\
& + \frac{1}{\sqrt{6}} P_{l0} C_{l020}^{j0} \big[2(\tau_{rr} \cos^2\vartheta - \tau_{r\vartheta} \sin 2\vartheta + \tau_{\vartheta\vartheta} \sin^2\vartheta) - \\
& - \ (\tau_{rr} \sin^2\vartheta + \tau_{r\vartheta} \sin 2\vartheta + \tau_{\vartheta\vartheta} \cos^2\vartheta + \tau_{\varphi\varphi}) \big] \ \big\} \sin\vartheta \, \mathrm{d}\vartheta,
\end{aligned}
$$

where $l = j - 2, j, j + 2$.